INVESTIGATION OF NOVEL GEOPHYSICAL TECHNIQUES FOR MONITORING CO_2 MOVEMENT DURING SEQUESTRATION

FINAL REPORT

Principal Investigator: G. Michael Hoversten[1]

Erika Gasperikova [2]

Lawrence Berkeley National Laboratory

One Cyclotron Rd

Mail Stop 90-1116

Berkeley CA, 94720

October 2003

gmhoversten@lbl.gov [1]

EGasperikova@lbl.gov [2]

CONTENTS

LIST OF FIGURES

List of Tables

Executive Summary - Abstract

This report considers the application of a number of different geophysical techniques for monitoring geologic sequestration of CO_2. The relative merits of seismic, gravity, electromagnetic and streaming potentials (SP) are considered for monitoring. Numerical modeling has been done on flow simulations based on a proposed CO_2 sequestration project on the North Slope of Alaska as well as a project in South Texas (to be begun in spring 2004).

Although we are specifically interested in considering "novel" geophysical techniques for monitoring we have chosen to include more traditional seismic techniques as a bench mark so that any quantitative results derived for non-seismic techniques can be directly compared to the industry standard seismic results. This approach puts the findings for "novel" techniques in the context of the seismic method and allows a quantitative analysis of the cost/benefit ratios of the newly considered methods compared to the traditional, more expensive, seismic technique.

The Schrader Bluff model was chosen as a numerical test bed for quantitative comparison of the spatial resolution of various geophysical techniques being considered for CO_2 sequestration monitoring. We began with a three dimensional flow simulation model provided by BP Alaska of the reservoir and developed a detailed rock-properties model from log data that provides the link between the reservoir parameters (porosity, pressure, saturations, etc.) and the geophysical parameters (velocity, density, electrical resistivity). The rock properties model was used to produce geophysical models from the flow simulations.

The difference in the vertical component of gravity caused by CO_2 injection over a 20-year period is on the order of 2 μGal, which is in the noise level of the field survey (Hare, 1999). The reduction in the vertical component of gravity is caused by increased CO_2 saturations reducing the bulk density of the reservoir. The spatial pattern of the change in the vertical component of gravity (G_z) as well as the vertical gradient of gravity (dG_z/dz) is directly correlated with the net change in density of the reservoir. Just as with G_z, the magnitude of dG_z/dz measured at the surface is above the gradiometer accuracy, but the difference between initial conditions and 20 years into CO_2 injection is too small to resolve with current technology. These results are for a CO_2 enhance oil recovery scenario where water is injected alternately with CO_2, reducing the net density change. Brine formations at the same depths would produce measurable responses. This is the experience at the Sleipner CO_2 project (Eiken, personal communication) for a gravity survey conducted in 2002 and not yet published. These results suggest future analysis to determine the maximum sensitivity of G_z and dG_z/dz that could be obtained by permanent emplacement of sensors with continuous monitoring coupled with surface deformation measurements to reduce noise levels.

In addition to surface gravity measurements borehole gravity measurements have been modeled. Measurements done in boreholes just above (1,200 m depth) the reservoir interval would produce measurable changes in G_z that would directly map the areas of net density changes caused by injected CO_2 and water within the reservoir. The difference in

both the borehole G_z and the borehole dG_z/dz identifies the position of the reservoir vertically in the borehole and maps the lateral changes in reservoir density when measured from several boreholes.

There is a significant change in seismic amplitude associated with the reservoir caused by the changes is water and CO_2 saturation as sequestration proceeds. In addition, there is a large change in the AVO response from the reservoir interval. Both seismic amplitude and AVO can be exploited to make quantitative estimates of saturation changes. Forward calculations using the Zoeppritz equation for both five and twenty years into injection show significant changes in both the zero-offset amplitude and the gradient of the response with angle.

The electrical resistivity of reservoir rocks is highly sensitive to changes in water saturation. This high sensitivity to water saturation in a reservoir can be exploited by electromagnetic (EM) techniques where the response is a function of reservoir electrical resistivity. Of all the possible combination of EM sources and measured EM fields one system combines both relative ease of deployment with high sensitivity to reservoirs of petroleum scale and depth. This technique uses a grounded electric dipole that is energized with an alternating current at a given frequency to produce time varying electric and magnetic fields that can be measured on the earth's surface. To simulate such an EM system we have calculated the electric field on the surface of the Schrader Bluff model using 100 m electric dipoles operating at 1 Hz and measuring the resulting electric field at a separation of 2 km in-line with the transmitting dipole. The generated electric field for the Schrader Bluff model, using only a small portable generator is an order of magnitude above the background electric field (noise) at the operating frequency of 1 Hz. This means that synchronous detection of the signal combined with stacking can recover signal variations to better than 1 percent. There is a direct one-to-one correspondence with the change in S_w and the change in the electric field amplitude. While this signal level is low, it can be measured give the signal-to-noise ratio of the data. While this represents a potential low-cost monitoring technique it is best suited for CO_2 – brine systems where there is a one-to-one correlation between the change in water saturation and the change in CO_2 saturation (since $S_w + S_{CO2} = 1$). In petroleum reservoir such as Schrader Bluff the presence of hydrocarbon as additional fluids eliminates the one-to-one correlation between changes in S_w and changes in S_{CO2}. This type of EM technique has not yet been employed as a monitoring tool within the petroleum industry. However, EM technology is currently the subject of a significant upsurge in industry interest. Several commercial contractors are now offering this technique as a survey tool, most notably, in the offshore environment where it is currently being used as an exploration tools (Ellingsrud et al. 2002). The equipment and service providers exist to apply this technique for monitoring in the future.

Laboratory studies coupled with numerical simulations show that the streaming potential coupling coefficients for CO_2 flow are large enough to cause a measurable SP signal in the field. As the CO_2 displaces water in a formation the coupling coefficient decreases. On average, the coupling coefficients observed for CO_2 flow is about 10 times lower than for fresh water flow in the same sample. The most effective way to spatially monitor injected

CO_2 flow is to monitor the progressing CO_2/water front, where the coupling coefficient is largest.

The SP method has the potential to be a low-cost low-resolution method of large scale reservoir monitoring. Compared to other geophysical techniques relatively little quantitative work has been done on the SP technique. We have simulated the response of a CO_2 sequestration scenario in 2D, based both on the Liberty Field and Sleipner CO_2 injection tests. Modeling results show that injection of CO_2 to the Liberty Field formation would produce a response, which is easily measured with the SP method. The Sleipner results are less encouraging, however a number of key parameters are poorly defined and definitive statements about the potential of SP as a monitoring tool cannot yet be made.

Modeling of a wide variety of geophysical techniques was done over the Liberty Field near Houston, Texas. This small-scale pilot project is part of the GeoSeq project and we are using our involvement with it to leverage the CCP funding. As part of this work we have determined that we should consider the use of surface tilt as a low cost monitoring technique. This was not in our original plans but as a result of our work at Liberty Field we feel it is worth considering.

Models were used to calculate anticipated contrasts in seismic velocity, density and impedance in brine-saturated rock when CO_2 is introduced. Numerical simulations were performed to evaluate how small a volume of CO_2 could be detected in the subsurface by the surface seismic reflection method and by surface gravity measurements. Results for geology appropriate for south Texas (Liberty Field) showed that a wedge of CO_2 in 10 m thick sand could be seismically detected. The gravity response was much less sensitive. The smallest volume that could be detected at 1,000 m depth was equivalent to 20 days production (240 m radius 50 m apex inverted cone of 100% CO_2 saturated sand) from a 1,000 MW coal powered power plant.

Introduction

Cost effective monitoring of reservoir fluid movement during CO_2 sequestration is a necessary part of a practical geologic sequestration strategy. Current petroleum industry seismic techniques are well developed for monitoring production in petroleum reservoirs. The cost of time-lapse seismic monitoring can be born because the cost to benefit ratio is small in the production of profit making hydrocarbon. However, the cost of seismic monitoring techniques is more difficult to justify in an environment of sequestration where the process produces no direct profit. For this reasons other geophysical techniques, which might provide sufficient monitoring resolution at a significantly lower cost, need to be considered.

In order to evaluate alternative geophysical monitoring techniques we have undertaken a series of numerical simulations of CO_2 sequestration scenarios. These scenarios have included existing projects (Sleipner in the North Sea), future planned projects (GeoSeq Liberty test in South Texas and Schrader Bluff in Alaska) as well as hypothetical models based on generic geologic settings potentially attractive for CO_2 sequestration. In addition, we have done considerable work on geophysical monitoring of CO_2 injection into existing oil and gas fields, including a model study of the Weyburn CO_2 project in Canada and the Chevron Lost Hills CO_2 pilot in Southern California (Hoversten et al. 2003).

Although we are specifically interested in considering "novel" geophysical techniques for monitoring we have chosen to include more traditional seismic techniques as a bench mark so that any quantitative results derived for non-seismic techniques can be directly compared to the industry standard seismic results. This approach will put all of our finding for "novel" techniques in the context of the seismic method and allow a quantitative analysis of the cost/benefit ratios of the newly considered methods compared to the traditional, more expensive, seismic technique.

The Schrader Bluff model was chosen as a numerical test bed for quantitative comparison of the spatial resolution of various geophysical techniques being considered for CO_2 sequestration monitoring. We began with a three dimensional flow simulation model provided by BP Alaska of the reservoir and developed a detailed rock-properties model from log data that provides the link between the reservoir parameters (porosity, pressure, saturations, etc.) and the geophysical parameters (velocity, density, electrical resistivity). The rock properties model was used to produce geophysical models from the flow simulations.

Selection of monitoring techniques

Petroleum reservoirs and brine formations offer the two most obvious sequestration targets. Petroleum reservoirs have the natural advantages that they are already well characterized, have a demonstrated seal, have an existing infrastructure, and offer cost offsets in the form of enhanced petroleum production as CO_2 is injected. From a monitoring standpoint, petroleum reservoirs offer more challenges than brine formations because they typically have less vertical extent (~25m for oil vs. 100's of m for brine formations) and have multiple in-situ fluids. Not withstanding their inherent monitoring challenges, petroleum reservoir will undoubtedly provide many of the early sequestration examples.

This report provides an evaluation of several geophysical monitoring techniques. This analysis makes use of a realistic scenario for a combined enhanced oil recovery (EOR) and CO_2 storage project. It is based on the Schrader Bluff oil field on the North Slope of Alaska and the Liberty Field pilot test in Texas.

On-shore EOR project – Schrader Bluff, Alaska

A joint industry project comprising BP, ChevronTexaco, Norsk Hydro, Shell, Statoil, Suncor was formed with the goal of developing technologies to enable the cost effective CO_2 capture and sequestration. One site being considered is the Schrader Bluff reservoir on Alaska's North Slope (Figure 1). Preliminary evaluations show that a CO_2 based enhanced oil recovery could increase oil recovery by up to 50% over waterflooding (Hill et al, 2000). Furthermore, the studies concluded that up to 60% of the CO_2 injected as part of the EOR scheme would remain in the reservoir. A schematic geological cross-section through the Schrader Bluff Formation is shown in Figure 2.

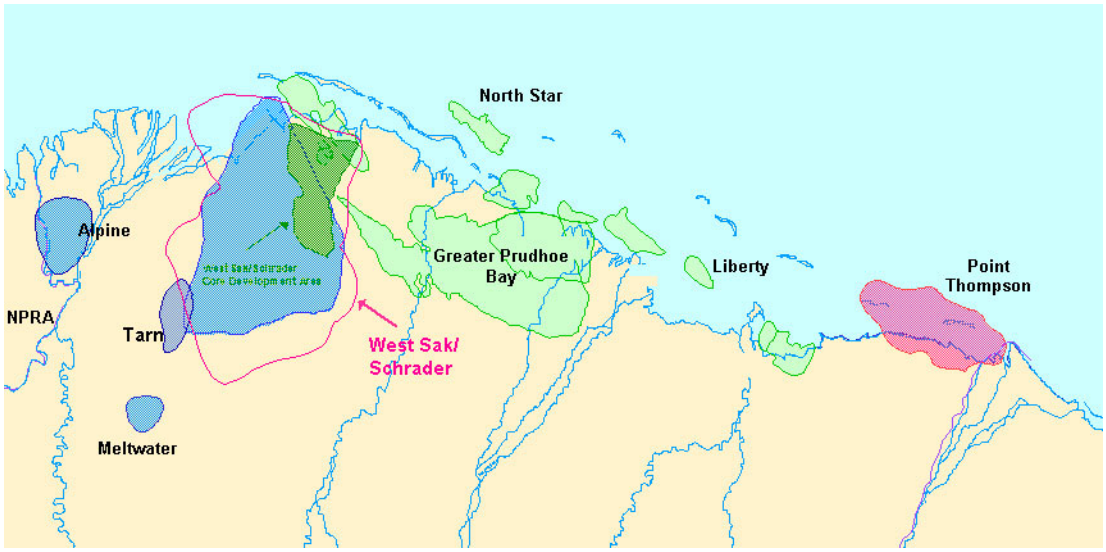

Figure 1: Location of Schrader Bluff reservoir on Alaska's North Slope.

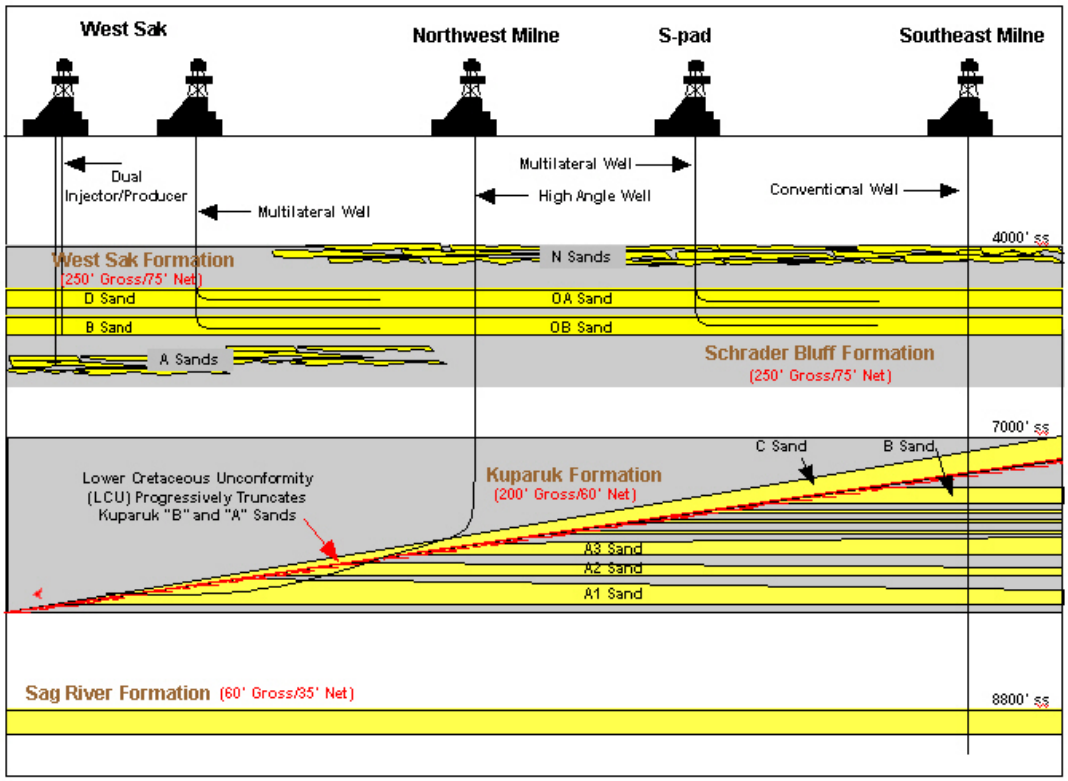

Figure 2: A schematic geological cross-section through the Schrader Bluff Formation.

In order to compare the spatial resolution and sensitivity of various geophysical techniques being considered for CO_2 sequestration monitoring a three-dimensional (3D) flow simulation model the reservoir provided by BP was used in conjunction with rock-

properties relations developed from log data to produce geophysical models from the flow simulations. The Schrader Bluff reservoir is a sandstone unit, between 25 and 30 m thick, at a depth of 1,100 – 1,400 m. Figure 3 shows a 3-D view of the portion of the reservoir under consideration for a CO_2 sequestration test. The reservoir unit gently dips to the east with major faulting running mainly north-south. Two faults with offsets in excess of 75 m cut the reservoir with several smaller sub-parallel faults present. Time-lapse snap shots of the reservoir at initial conditions and 5-year increments out to 2035 were used. A water after gas (WAG) injection strategy is considered which produces complicated spatial variations in both CO_2 and water saturation within the reservoir over time.

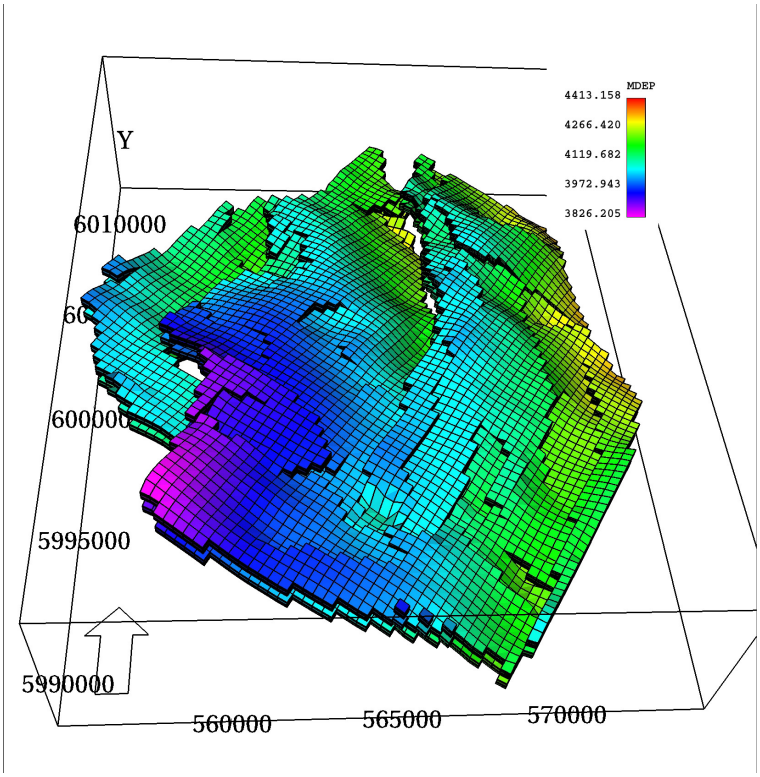

Figure 3. Three-dimensional view of the portion of the reservoir under consideration for CO2 sequestration test at Schrader Bluff. Depths range between 3,800 and 4,400 feet (1,158 and 1,341 m) true vertical depth.

Rock Properties Model

Rock properties models were developed from log data for the reservoir. These models relate reservoir parameters to geophysical parameters and are used to convert the flow simulation model parameters to geophysical parameters (V_P, V_S, density and electrical resistivity). A description of the rock-properties modeling process is given by Hoversten

et al. (2003). Electrical resistivity as a function of porosity and water saturation using an Archie's law formulation is used. Seismic properties are modeled as shown in Figure 4. The predicted V_p, V_s and density from the derived model based on log data from the MSP-15 well are shown.

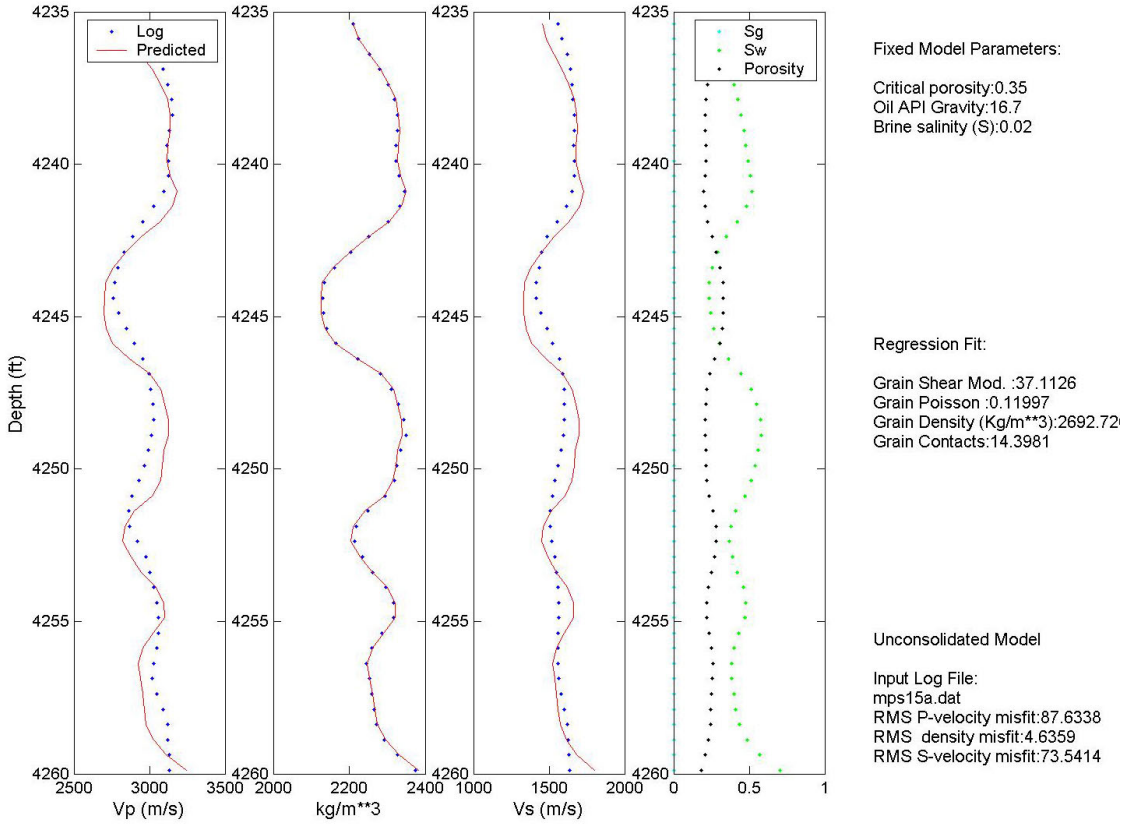

Figure 4. Rock properties model based on un-consolidated sandstone model (Dvorkin & Nur, 1996). Measured log values shown as blue dots. Parameters (right side) are derived from a simplex minimization of the misfit between observed and calculated V_p, V_s and density logs. Predicted V_p, V_s and density are shown as red lines.

A critical porosity appropriate for sandstone of 35% is assumed. Oil API gravity and brine salinity are taken from measured values. The regression determined values of the grain shear modulus and Poisson ratio are appropriate for quartz grains. The model parameters are determined for the reservoir interval in the logs. The full geophysical models are built by interpolating available well logs in 3D using the seismic reservoir surfaces as a spatial guide. This produces a background model in V_p, V_s, density and resistivity. The reservoir flow simulations, which only cover the reservoir interval, are then filled in at the time intervals where flow simulations were done. The model shown in Figure 4, along with Archie's law, is used to convert the porosity, water saturation, oil saturation, gas saturation, CO_2 saturation, pressure and temperature from the flow simulation to V_p, V_s, density and electrical resistivity.

Gravity modeling

A snapshot of the model at initial conditions, before CO_2 injection begins, is shown in Figure 5. Figure 5a is a cross-section of bulk density as a function of depth and horizontal distance between a pair of injection wells. In this figure, gravimeters are located in two wells roughly 8 km apart. The reservoir interval is outlined in white on Figure 5a. Figure 5b is a plan view of the density at initial conditions at a depth of 1,200 m with positions of 23 injecting wells taken from the reservoir simulation. The positions of the gravimeters are indicated by black squares. Spacing between the gravimeters in depth (z) is 10 m outside of the reservoir and 5 m inside of the reservoir. The white circle in the upper part of Figure 5b indicates a well for which borehole gravity responses are shown in Figure 11 and 12.

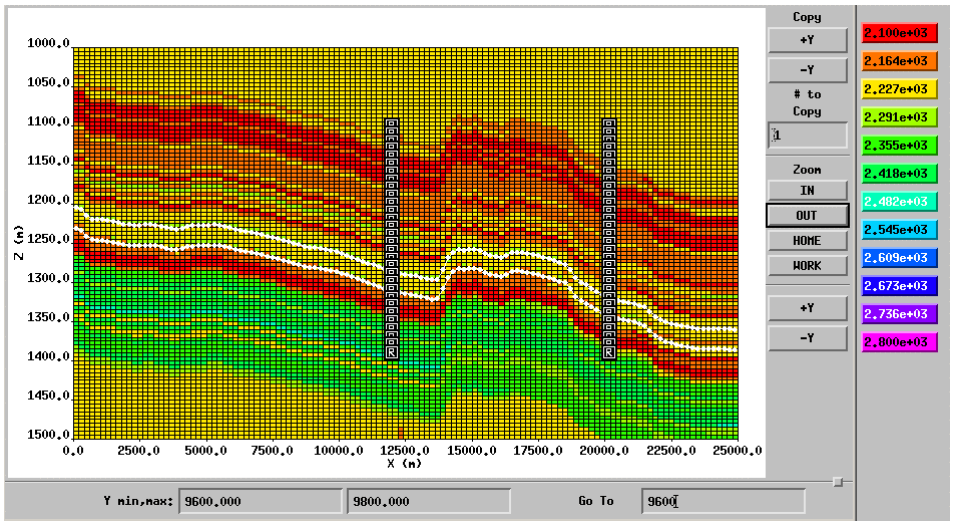

Figure 5a. Cross-section of a density field (kg/m^3) as a function of depth and horizontal position.

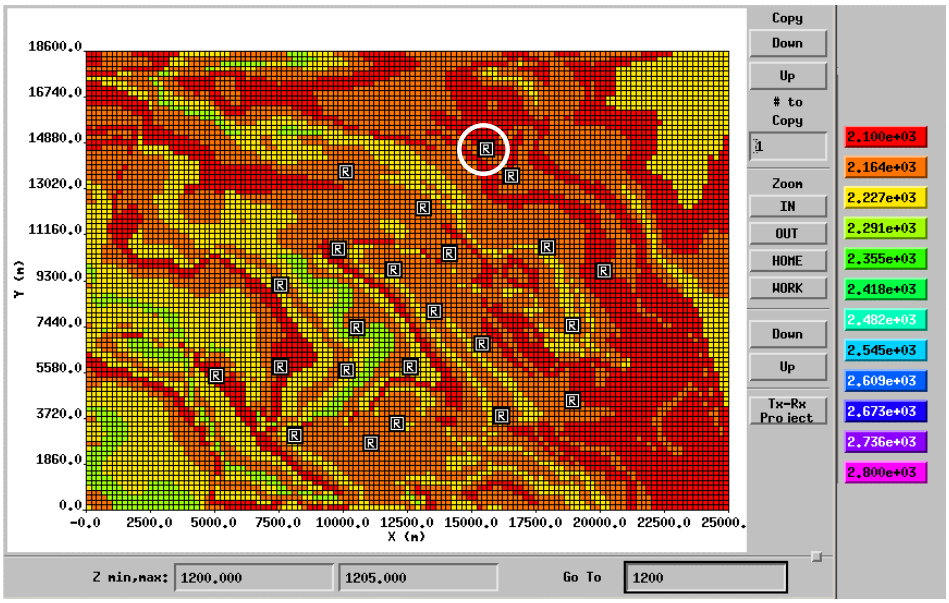

Figure 5b. Plan view of a density (kg/m^3) field at a depth z = 1,200 m. The white circle indicates the well location used for borehole gravity calculations shown in Figures 11 and 12.

The surface gravity response was calculated on a grid of stations with 1 km spacing from 2,000 m to 22,000 m in x and from 2,000 m to 16,000 m in the y direction. In general since CO_2 is less dense (at reservoir conditions) than either oil or water, addition of CO_2 to the reservoir will cause a reduction in the measured gravitational attraction either at the surface or in a borehole.

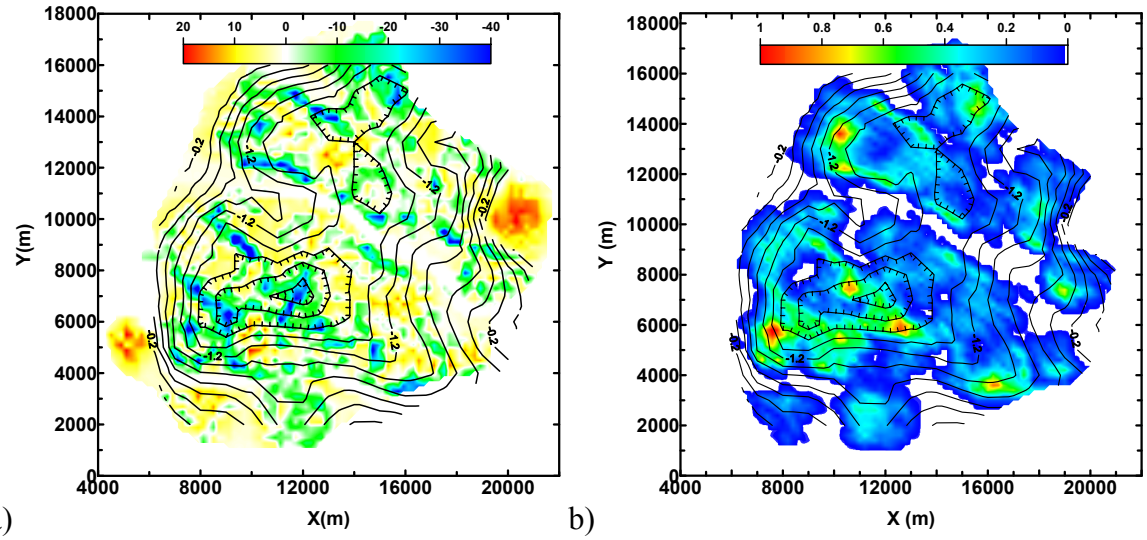

a) b)

Figure 6. (a) Plan view of the net change in density (kg/m^3) within the reservoir. (b) Plan view of the net changes in CO_2 saturation within the reservoir. The change in G_z

at the surface for the same time period is shown as black contours with hatch marks indicating decreasing G_z values.

The change in the vertical attraction of gravity (G_z) at the ground surface between 2020 and initial conditions is overlaid as black contours in Figure 5a on the net density changes within the reservoir. The peak-to-peak change in G_z is on the order of 2 μgal, which would be in the noise level of a field survey using current technology (Hare, 1999). The changes in the vertical gradient of gravity (dG_z/dz) between 20 years into CO_2 injection and initial conditions (not shown) are approximately 0.01 Eötvos units (EU), and also below the noise level of current instruments. The high spatial variations of the net density changes within the reservoir are expressed as a filtered response at the surface and only show the average changes on a larger scale. It should be noted that petroleum reservoirs in general, and this reservoir in particular, are thinner (30 m) than most brine formations considered for CO_2 sequestration (100–200 m). This difference means that while the calculated response for Schrader Bluff at the surface are below current technology repeatability, brine formations at the same depths would produce measurable responses. This is the experience at the Sleipner CO_2 project (Eiken, 2003) for a gravity survey conducted in 2002 and not yet published. These results suggest future analysis to determine the maximum sensitivity of G_z and dG_z/dz that could be obtained by permanent emplacement of sensors with continuous monitoring coupled with surface deformation measurements to reduce noise levels.

Figure 6b shows the change in surface gravity G_z as black contours overlaid on the net change in CO_2 saturation within the reservoir. Because the density changes within the reservoir are caused by a combination of CO_2, water and oil saturation changes as the WAG injection proceeds, there is not a one-to-one correlation in space between either the net change in density and the change in G_z or the net change in CO_2 saturation (S_{CO2}) and the change in G_z. There is correlation between the change in surface G_z and the net change in S_{CO2} on a large scale. For example, the largest changes in S_{CO2} occur in the south-west quadrant of the image (Figure 6b) where the largest change in G_z occurs. This scenario, injecting CO_2 into an oil reservoir with multiple fluid components, is a worst case for the use of gravity to directly map changes in S_{CO2}. In a CO_2 injection into a brine formation there would only be water and CO_2, in this case the net changes in density within the reservoir would directly correlate with the net changes in S_{CO2} as would the change in G_z at the surface.

Access to boreholes allows the gravity measurement to be made closer to the reservoir, thus strengthening the signal compared to observations made on the surface. Figure 7a shows the change in G_z (2020 – initial) at a depth of 1,200 m (just above the reservoir in this section of the field), while Figure 7b is a change in dG_z/dz at the same depth. In both figures, the data are calculated on the same grid of 1km by 1km site locations as on the surface. The color images in Figures 7a and 7b are the net density changes in the reservoir from Figure 7a. The changes in G_z and dG_z/dz respectively, correlate directly with the maximum density changes. The magnitude of the changes in both G_z and dG_z/dz is larger than for surface measurements, although only the change in G_z would be measurable in the boreholes with current commercial technology. It should

be noted however that work on more sensitive borehole G_z and dG_z/dz meters is ongoing and has the potential to significantly lower the sensitivity of such devices in the near future (Thomsen et al, 2003).

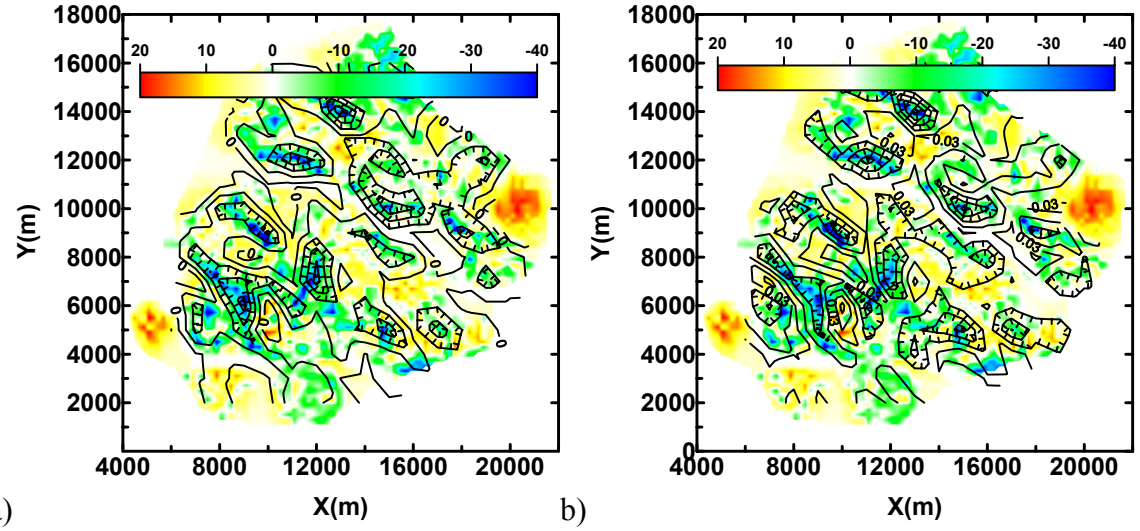

Figure 7. (a) Plan view of the color coded net change in density within the reservoir (2020-initial). The change in G_z (μGal) at a depth of 1,200 m is overlaid as black contours. The peak-to-peak change in G_z is approximately 10 μGal. (b) The change in dG_z/dz (EU) at a depth of 1,200 m overlaid on the net change in density. The peak-to-peak change in dG_z/dz is approximately 0.25 EU.

While Figure 7 illustrated the potential resolution by measuring close to the reservoir, access though the existing injection wells would substantially reduce the data coverage. Figure 8a shows a map of contoured changes in G_z measured only in the 23 boreholes at a depth of 1,200 m. Figure 8b is a net change of CO_2 saturation for comparison. Figure 8a was generated using a minimum curvature algorithm for data interpolation; however it is representative of the general features present in all of the other types of interpolation tested. In general, interpretation of the interpolated G_z changes from the boreholes would lead to an over estimate of the CO_2 saturation changes in the reservoir. This problem is particularly evident at the north end of the field where increased CO_2 saturation at two isolated wells produces an interpolated image that would be interpreted as increased CO_2 between the wells where none exists.

Borehole measurements would have to be used in conjunction with some form of surface measurement to guide the interpolation between wells. Alternatively, pressure testing between wells could provide estimates of spatial variations in permeability that could be used to condition, in a statistical sense, interpolation of the borehole gravity data. Many possibilities exist for combining the borehole data with other information in order to produce more accurate maps of change within the reservoir. This is an area where further work could be done.

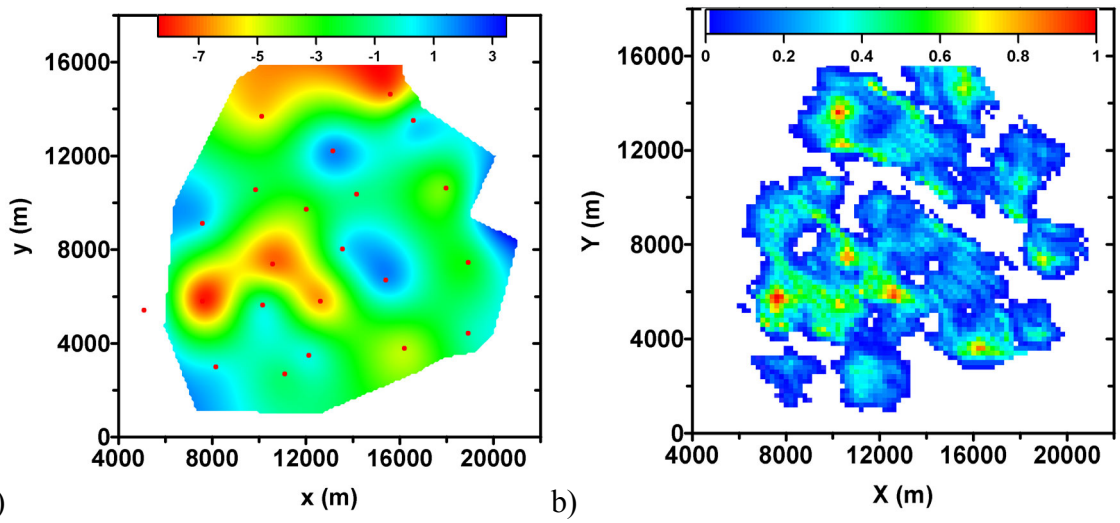

a) b)

Figure 8: (a) Plan view of the change in G_z (μGal) at a depth of 1,200 m between 20 years into CO_2 injection and initial conditions using 23 wells indicated by red dots. (b) Plan view of the net change in S_{CO2} within the reservoir between 20 years into CO_2 injection and initial condition.

In addition to considering spatial variations in G_z and dG_z/dz on both the surface and at a constant depth within boreholes the response of G_z and dG_z/dz in vertical profiles down boreholes has been considered. Figure 9 is the change in S_w between 2020 and initial conditions along a vertical slice through the reservoir at an injection well indicated by a white circle in Figure 5b. Figure 10 shows the change in S_{CO2} between 2020 and initial conditions. At the top of the reservoir near the injection well, S_w decreases while S_{CO2} increases. At the bottom of the reservoir, both S_{CO2} and S_w increase slightly. G_z measured in the borehole, shown in Figure 11a, reflects this change by a decrease in the response at the top of the reservoir, and an increase in the response at the bottom. The change in G_z is ± 8 μGal. The reservoir interval is between 1,325 and 1,350 m at this location. The change in G_z between 2020 and initial conditions (Figure 11b) clearly identifies the position of the reservoir. The sign of the change reflects the changes in the local densities caused by the combined changes in all fluids (oil, water and CO_2). The reservoir is outlined by the shaded blue area.

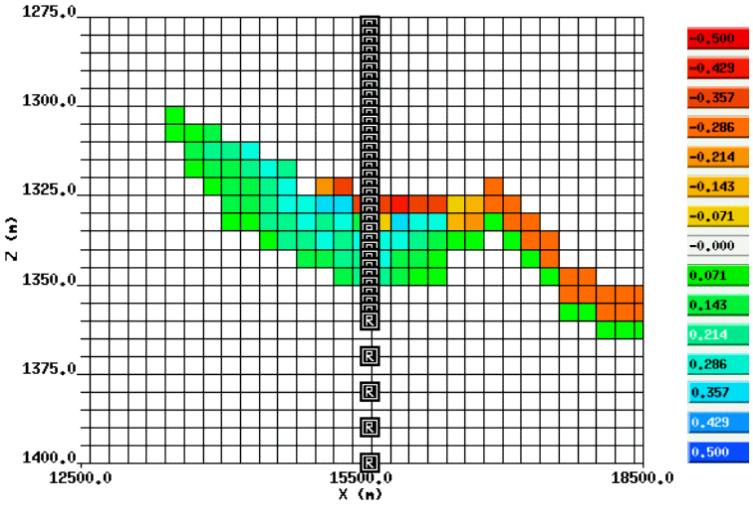

Figure 9. Change in S_w between 2020 and initial conditions. Greens and blues are an increase in S_w, yellows and reds are a decrease.

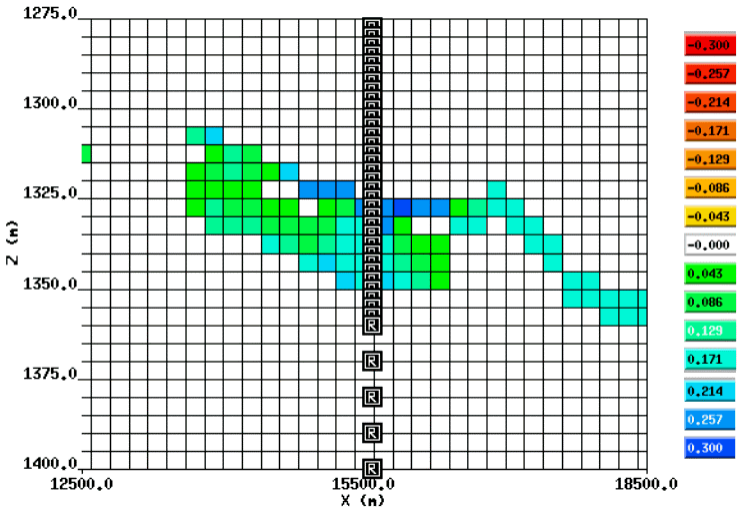

Figure 10. Change in S_{CO2} between 2020 and initial conditions. Greens and blues are an increase in S_{CO2}, yellows and reds are a decrease.

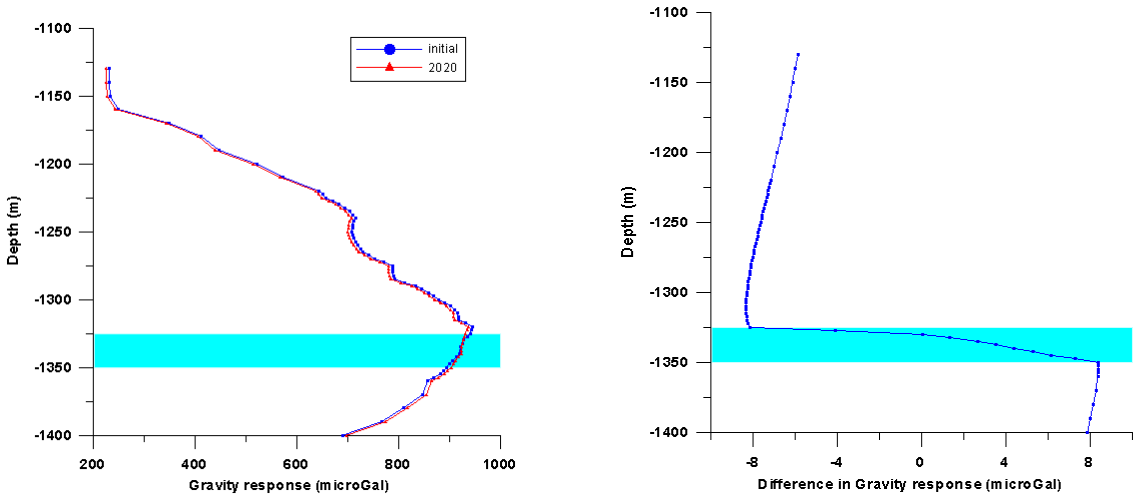

(a) (b)

Figure 11. (a) Borehole G_z for initial conditions (dark blue line) and 2020 (red line), (b) Change in G_z between 2020 and initial conditions. The reservoir interval is indicated by the light blue area.

The vertical gradient response (dG_z/dz) is shown in Figure 12a, and the change between 2020 and initial conditions is shown in Figure 12b. The change in the response is about 0.1 EU, which is not measurable with current technology.

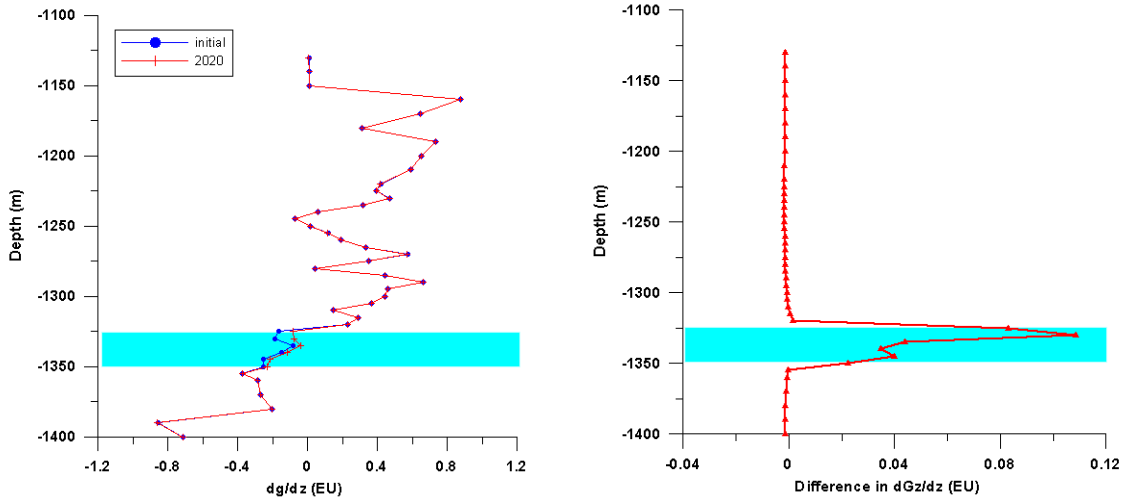

(a) (b)

Figure 12. (a) Borehole vertical gradient response (dG_z/dz) for initial conditions (dark blue line) and 2020 (red line), (b) Change in dG_z/dz between 2020 and initial conditions. The reservoir interval is indicated by the light blue area.

Popta et al. (1990) showed that a geological structure with a sufficient density contrast can be detected by borehole gravity measurements if the observation well is not

further away than one or two times the thickness of the zone of density contrast. Figure 13 shows a CO_2 wedge of 250 m radius and density of 2,260 kg/m^3 (representing 20% CO_2 saturation in 20% porosity) inside of 100 m thick sand layer with a density of 2,285 kg/m^3 at the depth of 1 km. The background density is 2,160 kg/m^3. The borehole gravity response as a function of distance from the right edge of the wedge is shown in Figure 14a. The maximum response at the edge of the CO_2 wedge is 10 μGal (due to 1% change in density). The responses decrease with distance away from the wedge. 50 m away from the wedge the response is 6 μGal, 100 m away response decreases to 4.4 μGal, and 200 m away it is down to 2.5 μGal. The borehole vertical gradient response for the same model is shown in Figure 14b. The response changes from 7 EU at the edge of the CO_2 wedge to 1 EU 50 m away from the edge.

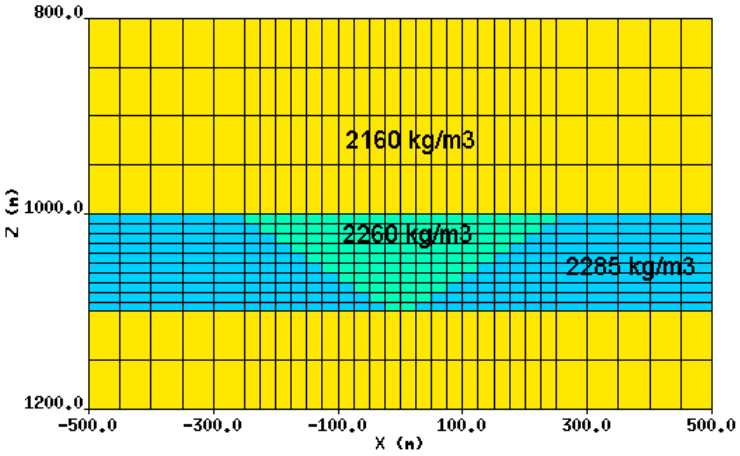

Figure 13: CO_2 wedge model.

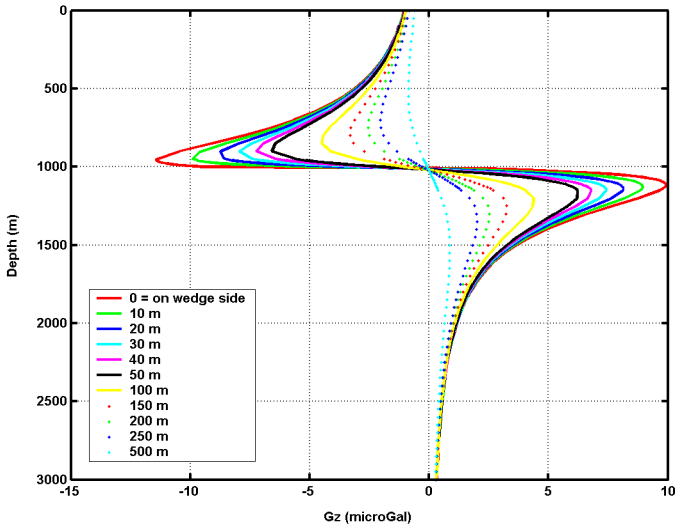

Figure 14a: Borehole gravity response of the model in Figure 13 as a function of distance from the wedge edge.

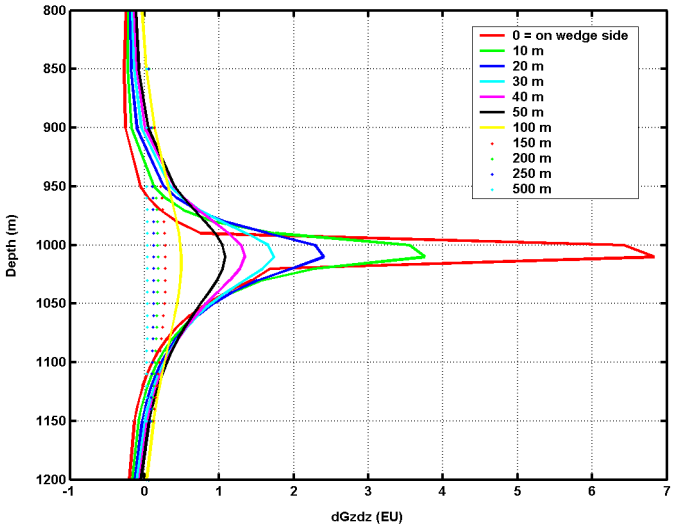

Figure 14b: Borehole vertical gradient gravity response of the model in Figure 13 as a function of distance from the wedge edge.

Current borehole gravimeter technology has a repeatability of around 5 μGal for G_z, this means that with current technology borehole measurements are sensitive to changes in a zone up at distances equal to the zone thickness away from the zone edge.

Seismic modeling

The flow simulation models for Schrader Bluff have been converted to acoustic velocity, shear velocity and density. A simulated seismic line has been calculated running approximately N45°E across the reservoir. The elastic response to a 50 Hz Ricker wavelet was calculated. The general increase in S_{CO2} in portions of the reservoir near injection wells produces an approximately 20% decrease in seismic velocity as shown in Figure 15 (change in P-wave velocity between 2020 and 2005). The S_{CO2} and S_w changes are shown in Figures 16 and 17 respectively. The seismic pressure responses, for a single shot located at 7,500 m (covering the area of the reservoir with maximum change in S_{CO2}) on the 2D profile, for 2005 and 2020 are shown in Figure 18 with the difference shown in Figure 19. There is a significant class 3 type AVO effect as S_{CO2} increases in the reservoir.

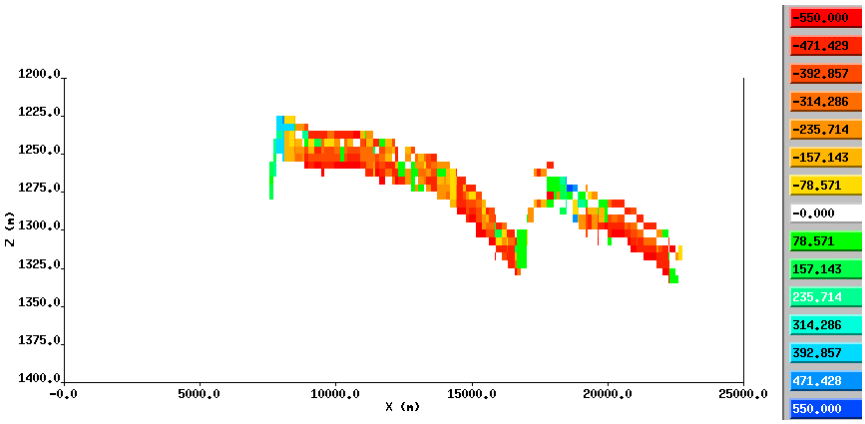

Figure 15. Change in the acoustic velocity (Vp) between 2020 and 2005 along a 2D profile extracted form the 3D model volume. The profile runs N45°E across the 3D model. Note the significant decrease in acoustic velocity associated with the increase in S_{CO2} (Figure 16).

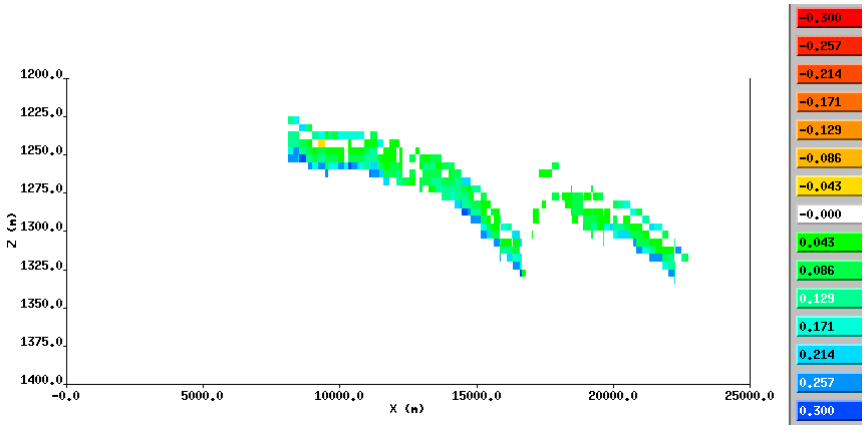

Figure 16. Change in the S_{CO2} between 2020 and 2005.

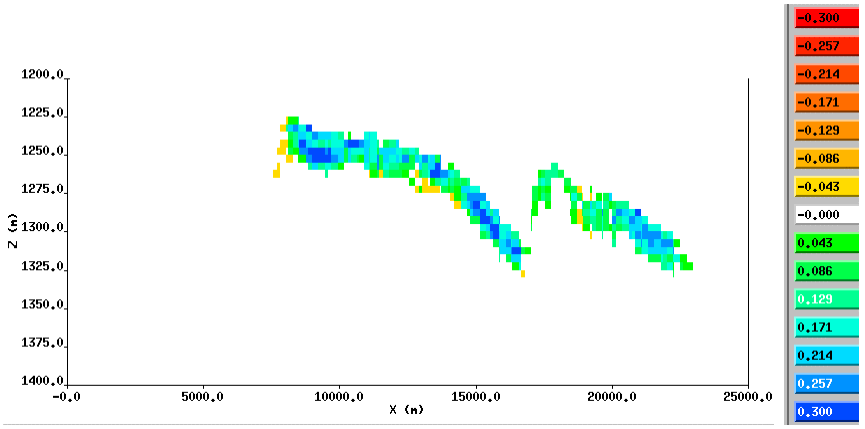

Figure 17. Change in S_w between 2020 and 2005.

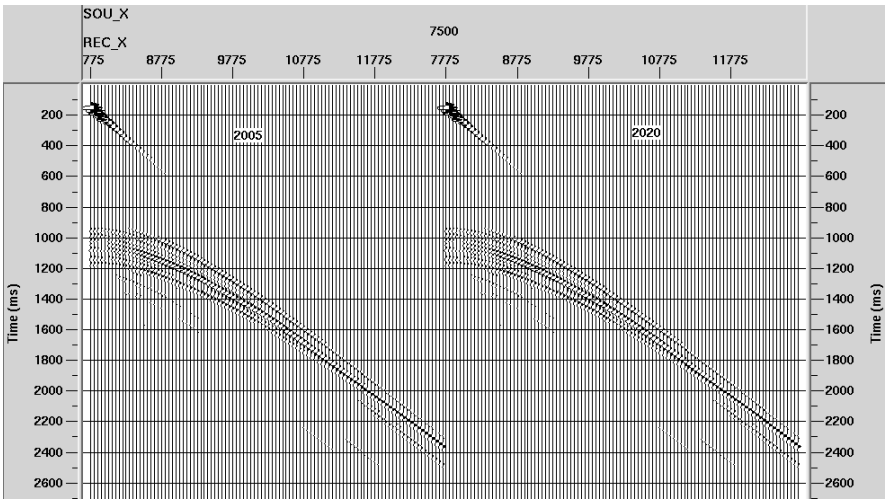

Figure 18. Seismic pressure response (shot gather) for 2005 and 2020.

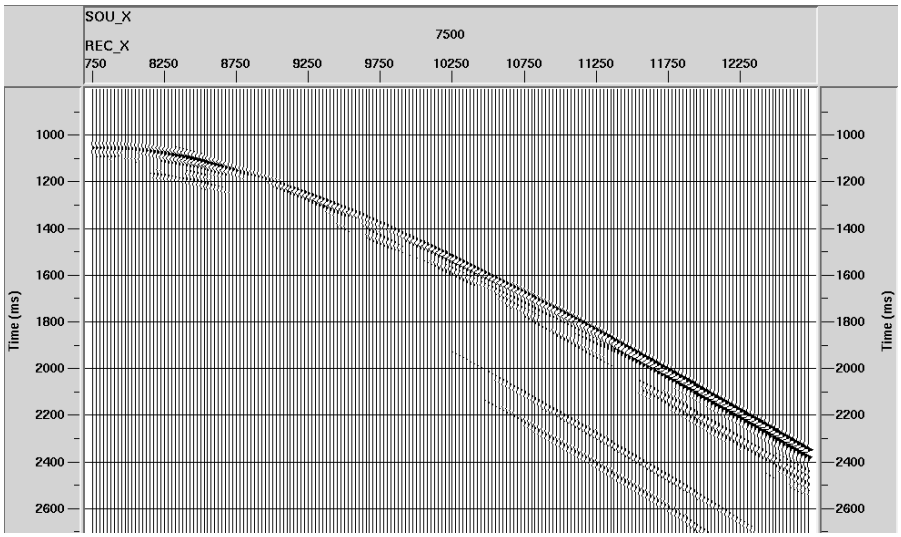

Figure 19. Change in pressure response (shot gather) between 2020 and 2005. Note amplitude change and AVO effects associated with S_w and S_{CO2} changes in the reservoir.

The pressure response was sorted to CDP gathers, NMO corrected and stacked to produce the sections for 2005 and 2020 shown in Figure 20. The red line is a constant time horizon within the reservoir for reference. The 30 m reservoir interval is not uniform and is comprised of 5 m thick substrata, each of which has reflection coefficients at their top and base that vary with S_{CO2}. These sub-strata are all below the seismic tuning thickness. This produces a seismic response without a clear top and base reflector. There is a significant increase in S_{CO2} to the right of CDP 8412.5 producing the large change in the stacked sections shown in Figure 20.

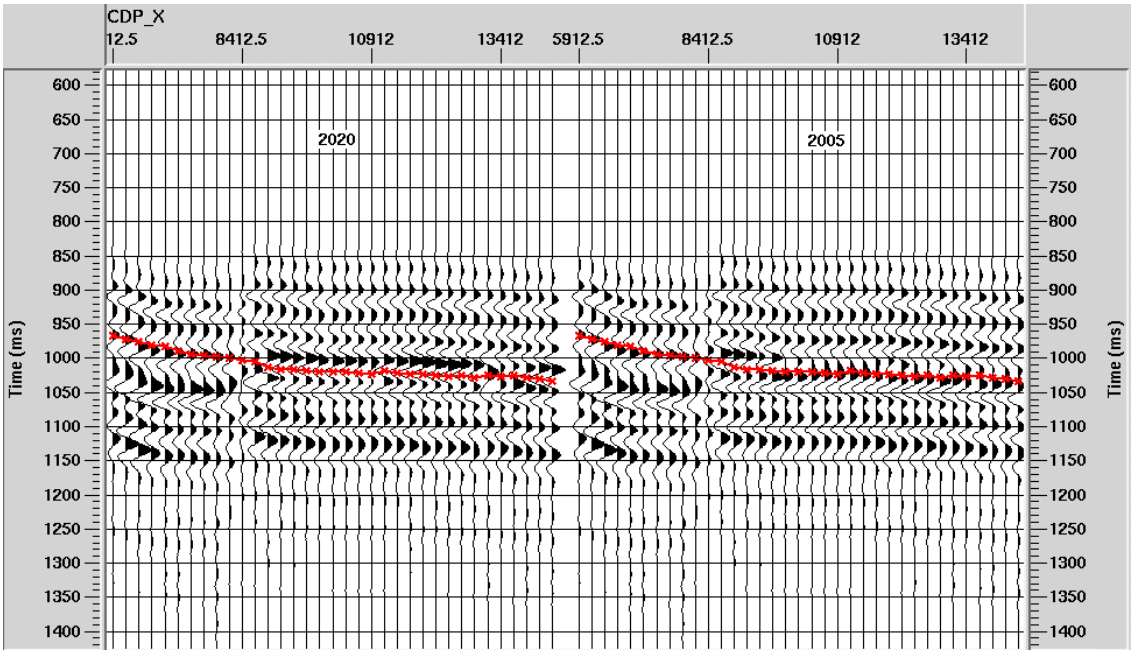

Figure 20. Stacked section for 2005 and 2020.

The change in the stacked sections between 2020 and 2005 is shown in Figure 21. Below the areas of major change in the reservoir (to the right of CDP 8412.5) the decrease in the velocity of the reservoir produces a time shift in the 2020 seismic responses below the reservoir, resulting in the events around 1,100 ms that do not reflect CO_2 saturation changes at this depth, only the time shift from CO_2 above.

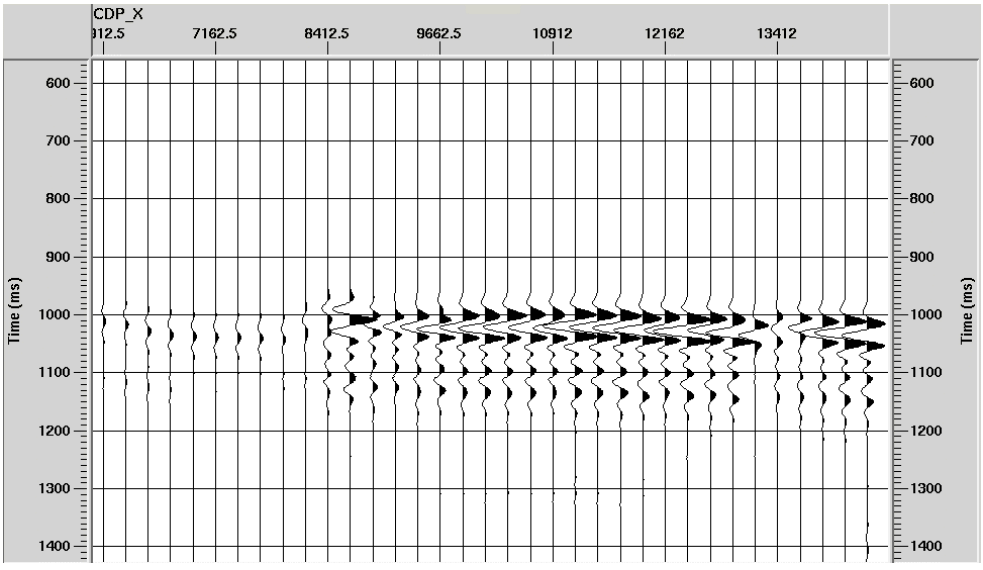

Figure 21. Change in the stacked sections between 2020 and 2005 (2020-2005).

There is a large, and easily measurable, change in the stacked trace amplitude associated with the reservoir caused by the changes in S_w and S_{CO2}. In addition, there is a change in the AVO effects as seen in Figure 19. Both amplitude and AVO can be exploited to make quantitative estimates of saturation changes under certain conditions. Forward calculations using the Zoeppritz equation for both the 2005 and 2020 models provide insight into the AVO dependence on model parameters. The forward modeling creates a synthetic seismic gather from a given set of elastic parameters V_P, V_S and density as a function of depth. The full Zoeppritz equation is used to compute the acoustic to acoustic (pp) reflection coefficient Rpp(θ) for each angle and at each layer boundary. Synthetic seismic CDP gathers are calculated by convolving the angle dependent reflection coefficients with a 50 Hz Ricker wavelet. The convolution model assumes plane-wave propagation across the boundaries of horizontally homogeneous layers, and takes no account of the effects of geometrical divergence, inelastic absorption, wavelet dispersion, transmission losses, mode conversions and multiple reflections.

The change in V_P, V_S, and density within the reservoir (between 1250 and 1275 m) is shown in Figure 22.

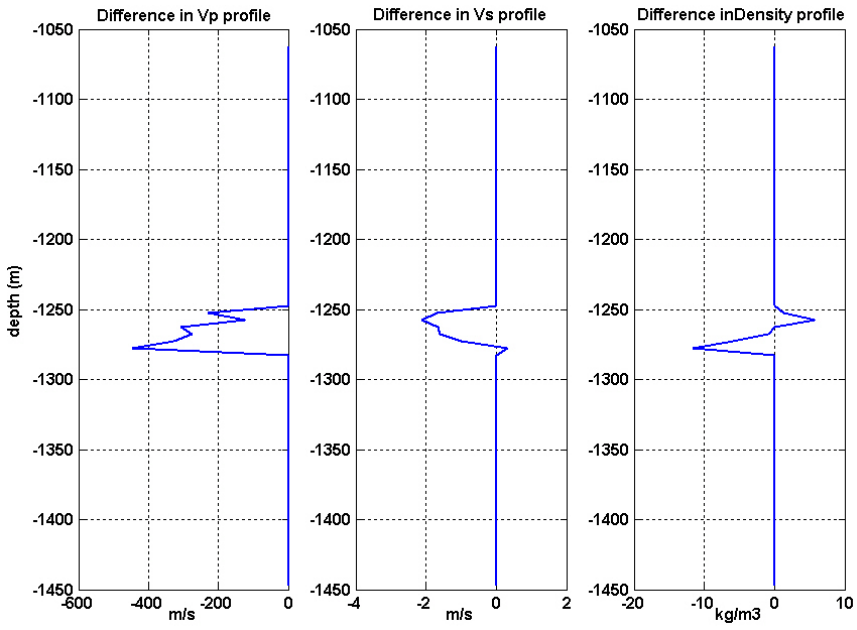

Figure 22. Difference in V_P, V_S, and density profiles between 2020 and 2005 for the Schrader Bluff model at the center of maximum CO_2 saturation increase.

The synthetic CDP gathers as a function of angle are shown in Figures 23a and 23b for 2005 and 2020 respectively. The change in reflection amplitude between 2020 and initial conditions is shown in Figure 24. The AVO response of the composite reflections from the reservoir interval shows increasing negative amplitude with offset, a typical Class 3 gas response. The negative trough (associated with the top of the reservoir) increases its magnitude with offset and is followed by an increasing peak amplitude with offset

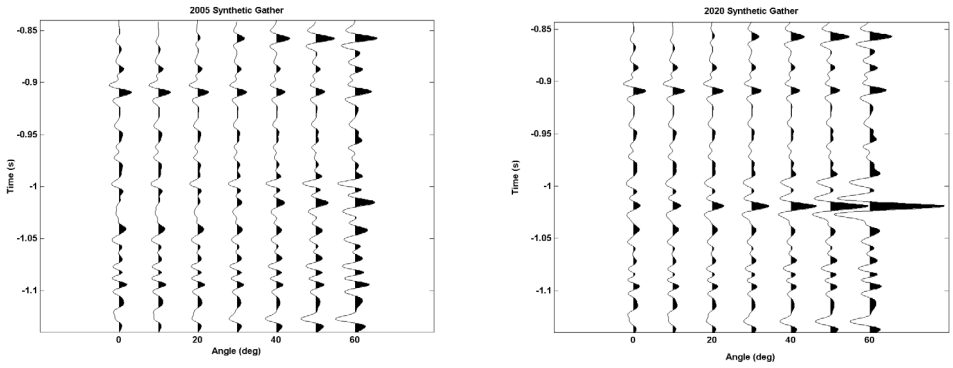

(a) (b)

Figure 23. Synthetic gather for (a) 2005 and (b) 2020.

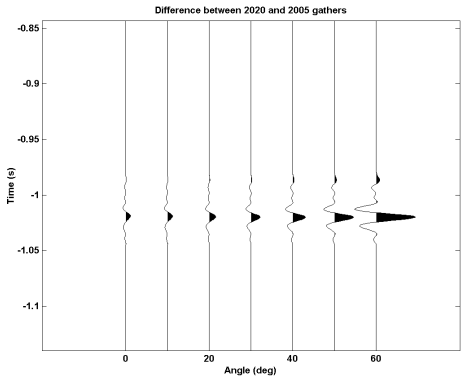

Figure 24. Difference between 2020 and 2005 gathers.

Use of AVO in fluid saturation prediction

The AVO attributes of reflections from the reservoir can be used to estimate fluid saturations under certain circumstances. AVO data can be used to estimate the acoustic and shear impedance of the reservoir (Castagna et al., 1998). When used in a time-lapse sense, these data can provide estimates of the change in water saturation and pressure within the reservoir (Landro, 2001). The ability to predict changes in water saturation and pressure within a reservoir is illustrated in Figure 25. In Figure 25 the rock properties model derived for the North Sea sands of the Troll reservoir (Dvorkin and Nur, 1996) is used to calculate the changes in shear and acoustic impedance of the reservoir as the water saturation and pore pressure for two cases of oil saturation as CO_2 is introduced. The first case (open circles) has initial oil and water saturation of 50%, as CO_2 is introduced it replaces water. The second case has an initial oil saturation of 60% and 40% water, with CO_2 replacing water. In both cases S_{CO2} ranges from 0 to 30%. Each point in the figure represents a unique value of S_W and S_{CO2} with the oil saturation held fixed at either 50% or 60%. S_{CO2} values increase in increments of 0.015% from right to left on the figure, and

pore pressure increases and decreases (indicated by arrows) from the reference pressure of 24.24 MPa by increments of 0.7 MPa.

Figure 25 illustrates three important points; 1) if the oil saturation is known the changes in shear and acoustic impedance of the reservoir can determine the change in pressure and CO_2 saturation, 2) the changes in the shear impedance required to make the estimates is quite small and would require extremely good shear data, 3) an uncertainty in the oil saturation level of 10% in this example has only a small effect on the estimated values of changes in S_{CO2} and almost no effect on the estimates of pressure change.

An uncertainty on the value of oil saturation has limited effects in these calculations because of the relative similarity of the bulk modulus and density of oil compared to water when either is compared to the properties of CO_2. The situation is significantly different if there is hydrocarbon gas (such as methane) in the reservoir. In this case (due to the extreme differences between the properties of methane and water) even a small uncertainty in the hydrocarbon gas saturation leads to very large uncertainties in the estimated values of pressure and CO_2 saturation changes, making this technique essentially unusable unless an independent estimate of water saturation or gas saturation can be obtained from other methods (Hoversten et al., 2003).

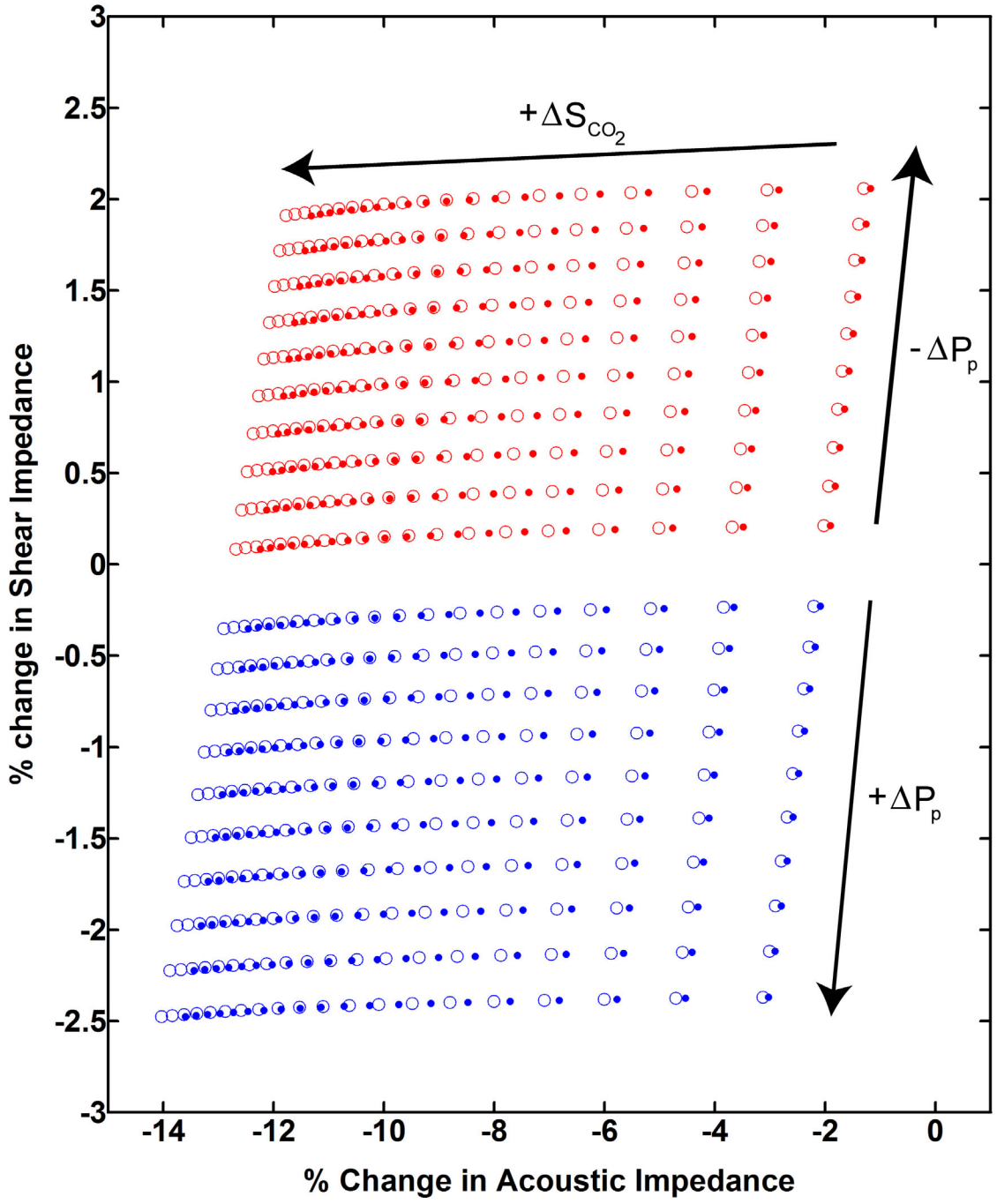

Figure 25. Each point represents a unique value of changes in pore pressure (ΔP_p) and CO_2 saturation (ΔS_{CO2}) as a function of changes in the shear and acoustic impedance of the reservoir. Open circles represent oil saturation of 50% with CO_2 replacing water. Filled dots represent oil saturation of 60% with CO_2 replacing water. Initial pore pressure is 25.24 MPa, initial S_{CO2} is 0%. S_{CO2} increments are 0.015 and pressure increments are 0.7 MPa.

While estimation of changes in fluid saturation using AVO is complicated by the multiple fluid components in oil or gas reservoir, the situation is simpler in a brine reservoir. For cases were CO_2 is injected into a brine reservoir there are only two fluid components (brine and CO_2) and the added constraint that their saturations levels sum to one. In this case AVO information can more easily be used to estimate the level of CO_2 in the reservoir. The following example illustrates this process. An unconsolidated North Sea sand of the Troll reservoir (Dvorkin and Nur, 1996) that is encased in shale is assumed to contain 50% brine and 50% CO_2 as the reference point for these calculations. Pressure and temperature are such that the CO_2 is in the liquid state. The values of CO_2 (and hence water) saturation and pore pressure are varied about this starting point and the acoustic and shear velocities as well as density are calculated.

The reflection coefficient at the top of the reservoir can be approximated (Shuey, 1985) by:

$$R(\theta) \approx A + B\sin^2(\theta) + C\sin^2(\theta)\tan^2(\theta) \tag{2}$$

where θ is the average of the reflection and transmission angle for a plane wave hitting the interface. The constants A and B are referred to as the intercept and slope respectively in the AVO literature. The constants A, B and C are functions of the velocity and density of the media on either side of the reflecting interface and are given by:

$$A = 1/2(\Delta V_p / \langle V_p \rangle + \Delta\rho / \langle \rho \rangle \tag{3}$$

$$B = 1/2(\Delta V_p / \langle V_p \rangle - 2(\langle V_s \rangle / \langle V_p \rangle)^2 (2\Delta V_s / \langle V_s \rangle + \Delta\rho / \langle \rho \rangle)) \tag{4}$$

$$C = 1/2(\Delta V_p / \langle V_p \rangle \tag{5}$$

where ΔV_p is the change in acoustic velocity across the interface and $\langle V_p \rangle$ is the average acoustic velocity across the interface, ΔV_s , $\langle V_s \rangle$, $\Delta\rho$, and $\langle \rho \rangle$ are changes and averages for shear velocity and density respectively. If time lapse seismic data is acquired, and A and B are estimated from the AVO data and used to calculate ΔA and ΔB, the associated ΔS_{CO2} and ΔP_p can be estimated from model based calculations such as are illustrated in Figure 26.

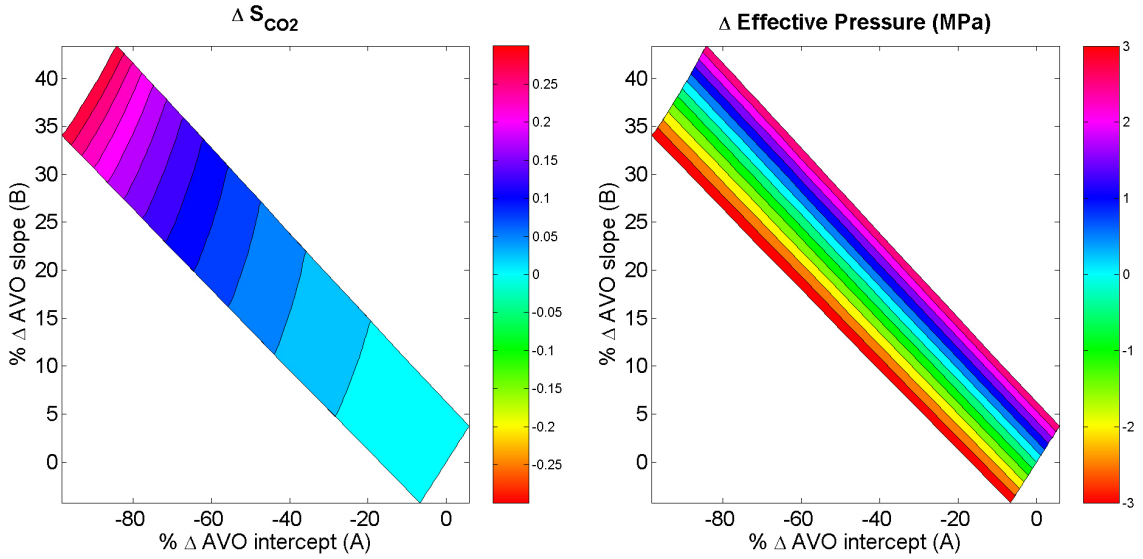

Figure 26. Contours of the change in CO_2 saturation (left panel) and effective pressure (lithostatic – pore pressure) (right panel) as function of the change in the AVO intercept (A) and slope (B) for an unconsolidated sand surrounded by shale.

This example illustrates a theoretical case without noise in the seismic data, in practice estimation of the "slope", B, is the most difficult. Extremely high signal to noise (S/N) seismic data would be required for accurate estimates of B and hence accurate estimates of pressure and saturation changes.

Electromagnetic modeling

The electrical resistivity of reservoir rocks is highly sensitive to changes in water saturation. This can be seen from Archie's Law (Archie 1942), which has been demonstrated to accurately describe the electrical resistivity of sedimentary rocks as a function of water saturation, porosity, and pore fluid resistivity. Figure 27 shows the rock bulk resistivity (Ωm) as a function of gas saturation (1–water saturation) for a reservoir with brine resistivity equivalent to sea water (ρ_{brine} = 0.33) with 25% porosity. All petroleum fluids (oil, condensate, and hydrocarbon gas) as well as CO_2 are electrically resistive, hence the relation shown in Figure 27 is appropriate for any

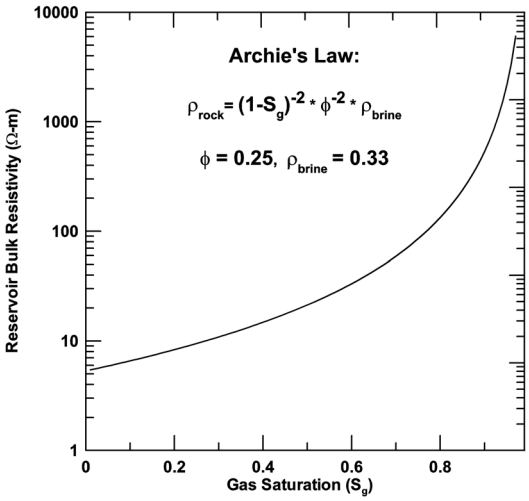

Figure 27. Reservoir bulk resistivity as a function of gas saturation (S_g). Porosity = 25%.

combination of oil, hydrocarbon gas, condensate or CO_2.

The bulk resistivity in Figure 27 is plotted on a log scale to span the large range of resistivity values as a function of the gas saturation (S_g). This high sensitivity to water saturation in a reservoir can be exploited by electromagnetic (EM) techniques where the response is a function of the earths electrical resistivity. Of all the possible combination of EM sources and measured EM fields one system combines both relative ease of deployment with high sensitivity to reservoirs of petroleum scale and depth. This technique uses a grounded electric dipole that is energized with an alternating current at a given frequency to produce time varying electric and magnetic fields that can be measured on the earth's surface. The electric dipole can consist of two steel electrodes (1 m^2 plates or sections of drill pipe) buried at a shallow depth (1-10 m) separated by 100 m and connected by cable to a low power generator (a portable 5,000 W generator is sufficient). The measured data would consist of the electric field at a given separation from the transmitter acquired on the surface or within the near surface.

To simulate such an EM system we have calculated the electric field on the surface of the Schrader Bluff model using 100 m electric dipoles operating at 1 Hz an measuring the resulting electric field at a separation of 2 km in-line with the transmitting dipole. Figure 28 shows the amplitude of the generated EM field at 2 km separation and 1 Hz together with the natural background electric field generated from worldwide thunderstorms and pulsations in the earths ionosphere (the source field for the magnetotelluric method). The significance of Figure 28 is that the generated electric field for the Schrader Bluff model, using only a small portable generator (producing a 10 A current in the source dipole) is an order of magnitude above the background electric field (noise) at the operating frequency of 1 Hz. This means that synchronous detection of the signal combined with stacking can recover signal variations to better than 1 percent.

Figure 29 shows the net change in water saturation within the reservoir (vertically integrated ΔS_w) between 2020 and initial conditions. The change in the electric field amplitude for the same interval is overlaid as black contour lines, with peak-to-peak amplitude of 1.2%. There is a direct one-to-one correspondence with the change in S_w and the change in the electric field amplitude. While this signal level is low, it can be measured give the signal-to-noise ratio of the data (Figure 28). While this represents a potential low-cost monitoring technique it is best suited for CO_2 – brine systems where there is a one-to-one correlation between the change in water saturation and the change in CO_2 saturation (since $S_w + S_{CO2} = 1$). In petroleum reservoir such as Schrader Bluff the presence of hydrocarbon as additional fluids eliminates the one-to-one correlation between changes in S_w and changes in S_{CO2}. This is illustrated in Figure 30 where the same changes in electric field amplitude are overlaid on the net change in the CO_2 saturation within the reservoir between 2020 and initial conditions. In this case we see that the correlation between changes in S_{CO2} and changes in the electric field amplitude are not as good as seen between changes in S_w and the electric field data.

This type of EM technique has not yet been employed as a monitoring tool within the petroleum industry. However, EM technology is currently the subject of a significant

upsurge in industry interest. Several commercial contractors are now offering this technique as a survey tool, most notably, in the offshore environment where it is currently being used as an exploration tools (Ellingsrud et al. 2002). The equipment and service providers exist to apply this technique for monitoring in the future.

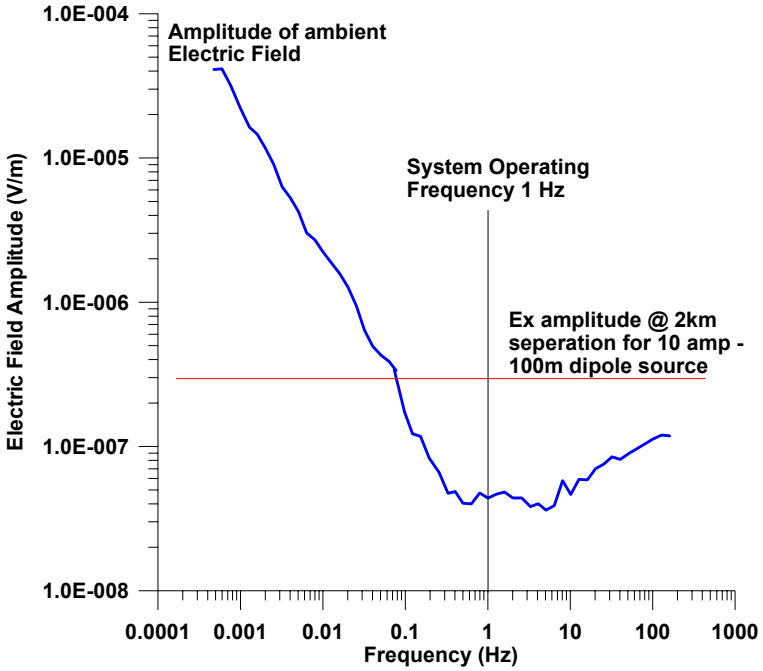

Figure 28. Amplitude of naturally occurring electric field as a function of frequency (Gasperikova et al. 2003), that would be considered noise to that electromagnetic system considered here for monitoring, shown as blue curve. The horizontal red line represents the signal amplitude at a source-receiver separation of 2 km at an operating frequency of 1 Hz for a 100 m electric dipole energized with 10 A of current.

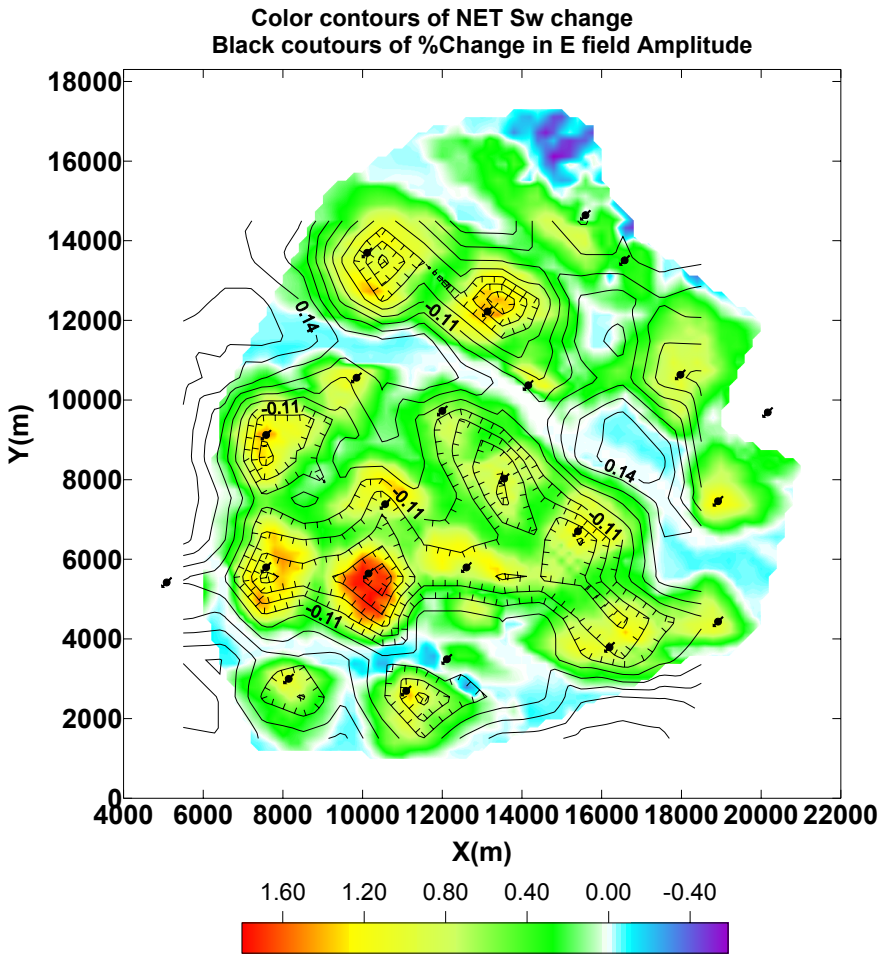

Figure 29. Color contours of the net change in water saturation over the vertical interval of the reservoir between 2020 and initial conditions. The change in the amplitude of the electric field from an electric dipole source at a separation of 2 km is overlaid as black contours. The peak-to-peak change is electric field amplitude is 1.2 %. Note the direct correlation between decreases in the electric field amplitude and increases in water saturation (decreased electric resistivity of the reservoir). Locations of injection wells are shown by black circles with arrows through them.

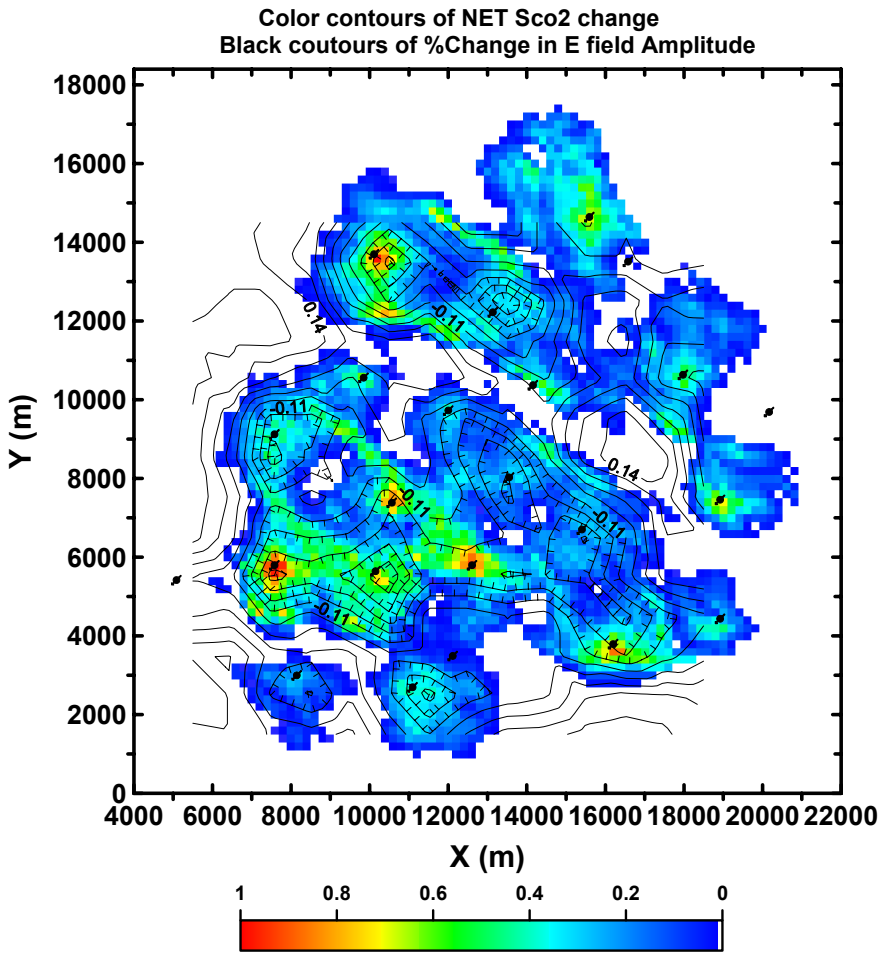

Figure 30. Color contours of the net change in CO_2 saturation (ΔS_{CO2}) over the vertical interval of the reservoir between 2020 and initial conditions. The change in the amplitude of the electric field from an electric dipole source at a separation of 2 km is overlaid as black contours. The peak-to-peak change is electric field amplitude is 1.2 %. Location of injection wells are shown by black circles with arrows through them.

On-shore saline aquifer – Frio Formation, Texas

Brine-bearing formations that are below and hydrologically separated from potable water reservoirs above have been widely recognized as having high potential for CO_2 sequestration. One of the most promising sites is the Frio Formation in Texas, which was chosen as a field demonstration site as part of the U.S. DOE and NETL sponsored GeoSeq project. The test demonstration project has four main goals; 1) demonstrate that CO_2 can be injected into a saline formation without adverse health, safety, or environmental effects, 2) determine the subsurface location and distribution of the injected CO_2 plume, 3) demonstrate an understanding of the conceptual models, and 4) develop experience necessary for the success of future large-scale CO_2 injection experiments (Hovorka and Knox, 2002).

The South Liberty pilot test site lies on the south side of a salt dome (Figure 31 and Figure 32). The injection target is the Frio Formation which is strongly compartmentalized by a pattern of high-angle faults radiating from the salt dome and associated cross faults. The structure and fault boundaries used for modeling are based on upward extrapolation of structure and fault patterns mapped from 3-D seismic on a producing interval about 1,000 m below the brine-bearing upper Frio Formation. This structural interpretation has a 440 m-wide compartment with fault boundaries on the northwest, northeast, and southeast. A fault boundary in the southwest side of the compartment was not imaged within the seismic volume, so the closure on this side is unknown and is considered as a variable in the modeling experiment. Within the compartment, strata are tilted off the salt dome. At the injection well, the top of the Frio Formation is at about 1,500 m depth, strikes N70°W, and dips 15° toward the southwest. Stratigraphy employed for the flow modeling focuses on the selected injection interval, a 12-m thick high-porosity, high-permeability sandstone referred to as the C sand, which is separated into upper and lower halves by a thin (0.3 m) shale layer. The section below the thin shale, an upward-coarsening sand, is the actual injection target. Locally extensive shale deposited within the Frio during cycle-bounding flooding events form sealed boundaries at the top and bottom of the C sand. The thick regionally extensive shale of the Anahuac Formation overlies the Frio Formation and provides an additional impermeable boundary isolating CO_2 from the land surface.

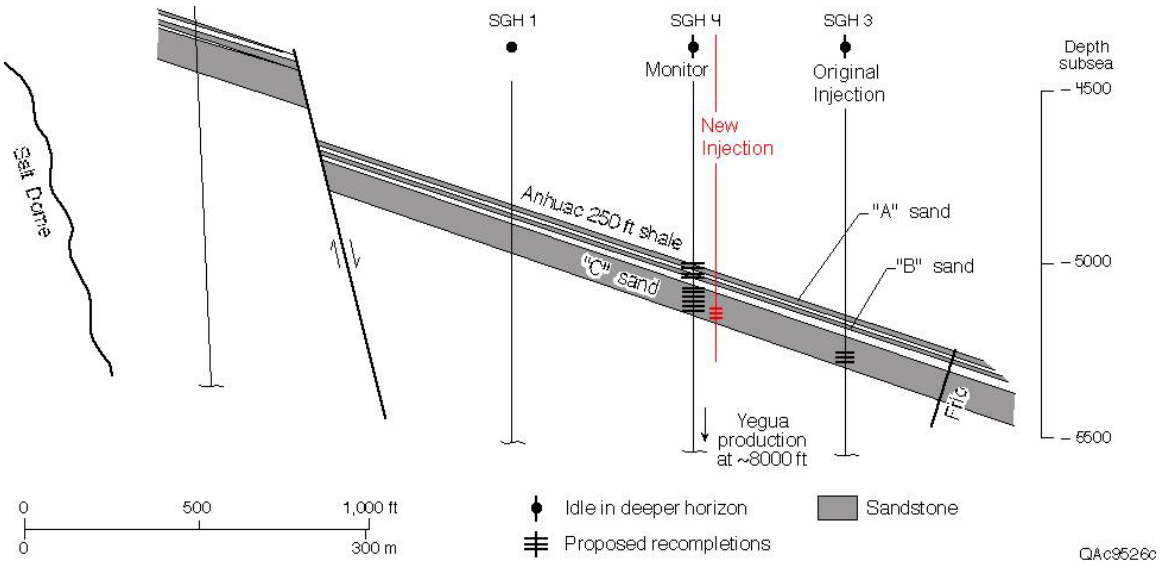

Figure 31. Schematic cross-section of the Frio Formation at the South Liberty pilot test site, Texas.

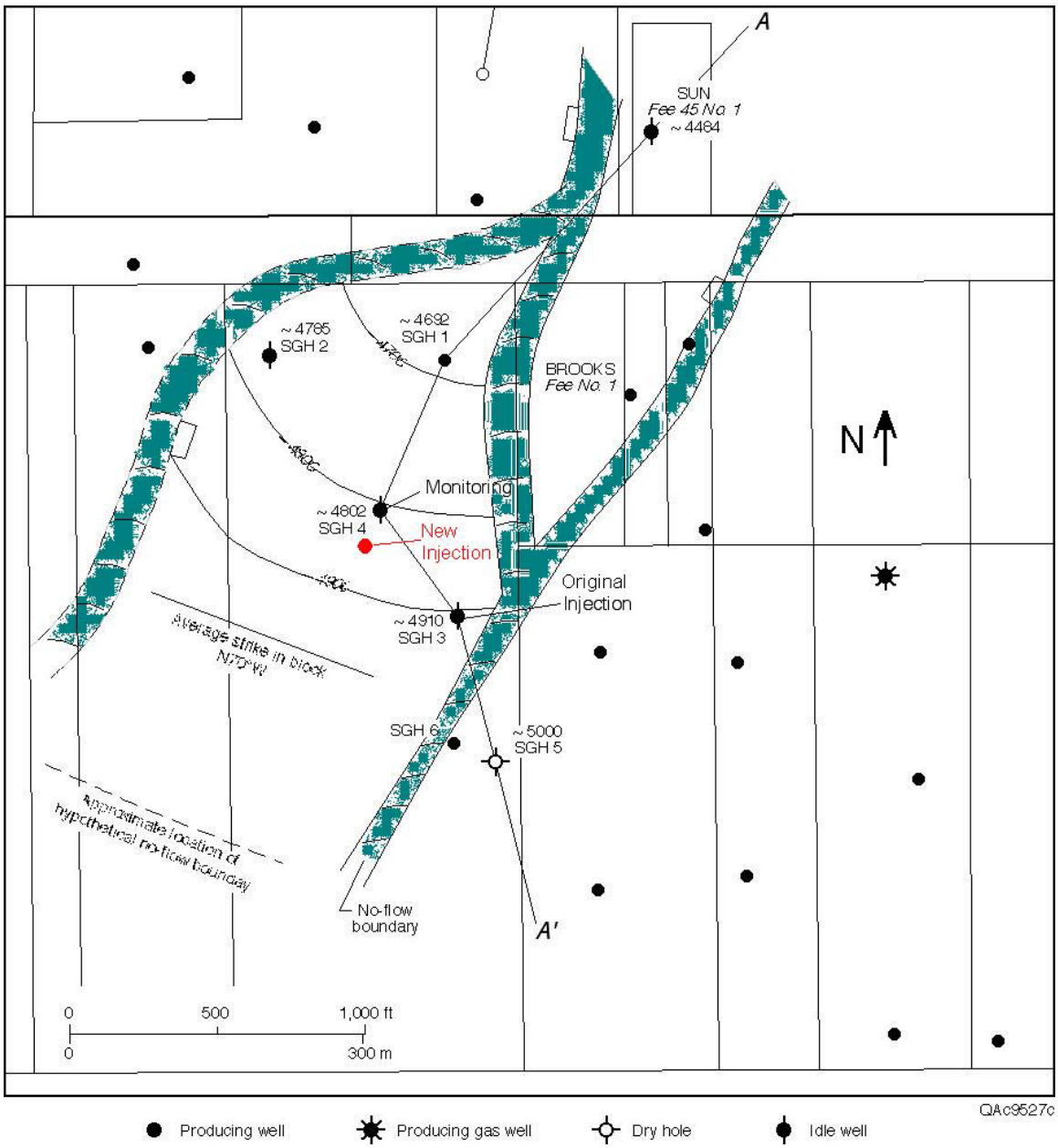

Figure 32. Schematic plan view of the South Liberty pilot test site. The shaded bands show sub-vertical faults that are assumed to act as impermeable barriers to fluid flow.

The regional geothermal gradient is taken to be 32.6°C/1,000 m (Loucks et al., 1984). For Frio water chemistry at these depths, reasonable values are TDS 100,000 ppm, Na 35,000 ppm and Cl 45,000 ppm (Kreitler et al., 1988; Macpherson, 1992). The injection interval is nonproductive of hydrocarbons.

CO_2 will be trucked to the site and injected into the high-permeability C sand within the upper Frio formation. There will be a series of field monitoring experiments before, during and after CO_2 injection. These experiments will test effectiveness of a spectrum of CO_2 monitoring techniques and compare the results to validate the methods. Injection will be

completed within 15-20 days, followed by up to a year of monitoring and assessment. There is one monitoring well, located about 30 m up-dip of the injection well (Figures 31 and 31).

Based on the geological setting of fluvial/deltaic Frio Formation, a 3-D stochastic model of the C sand was created for fluid flow and transport modeling using a two-phase (liquid, gas), three-component (water, salt, and CO_2) system in the pressure/temperature regime above the critical point of CO_2 (P = 73.8 bars, T = 31°C) (Doughty and Pruess, 2003). When CO_2 is injected in a supercritical state it has a much lower density and viscosity than the liquid brine it replaces, making buoyancy flow a potentially important effect. The model is bounded above and below by closed boundaries, which represent continuous shale. Three of the four lateral boundaries are closed to represent the edges of the fault block. CO_2 is injected at a rate of 250 metric tons per day (2.9 kg/s) for a period of 20 days, and then the system is monitored for an additional year. Initial formation conditions are P = 150 bars, T = 64°C and TDS = 100,000 ppm. Under these conditions, supercritical CO_2 has a density of 565 kg/m^3 and a viscosity of 4.3 x 10^{-5} Pa·s. In the reservoir, about 15% of the CO_2 dissolves in the brine, with the remainder forming an immiscible gas-like phase.

During the 20-day injection period, the distribution of CO_2 is nearly radially symmetric around the injection well (Figure 33). The plume arrives at the monitoring well in 2-3 days. After injection ends, the plume begins to spread and it doesn't take long for gas saturation to decrease to the residual value, making the plume essentially immobile.

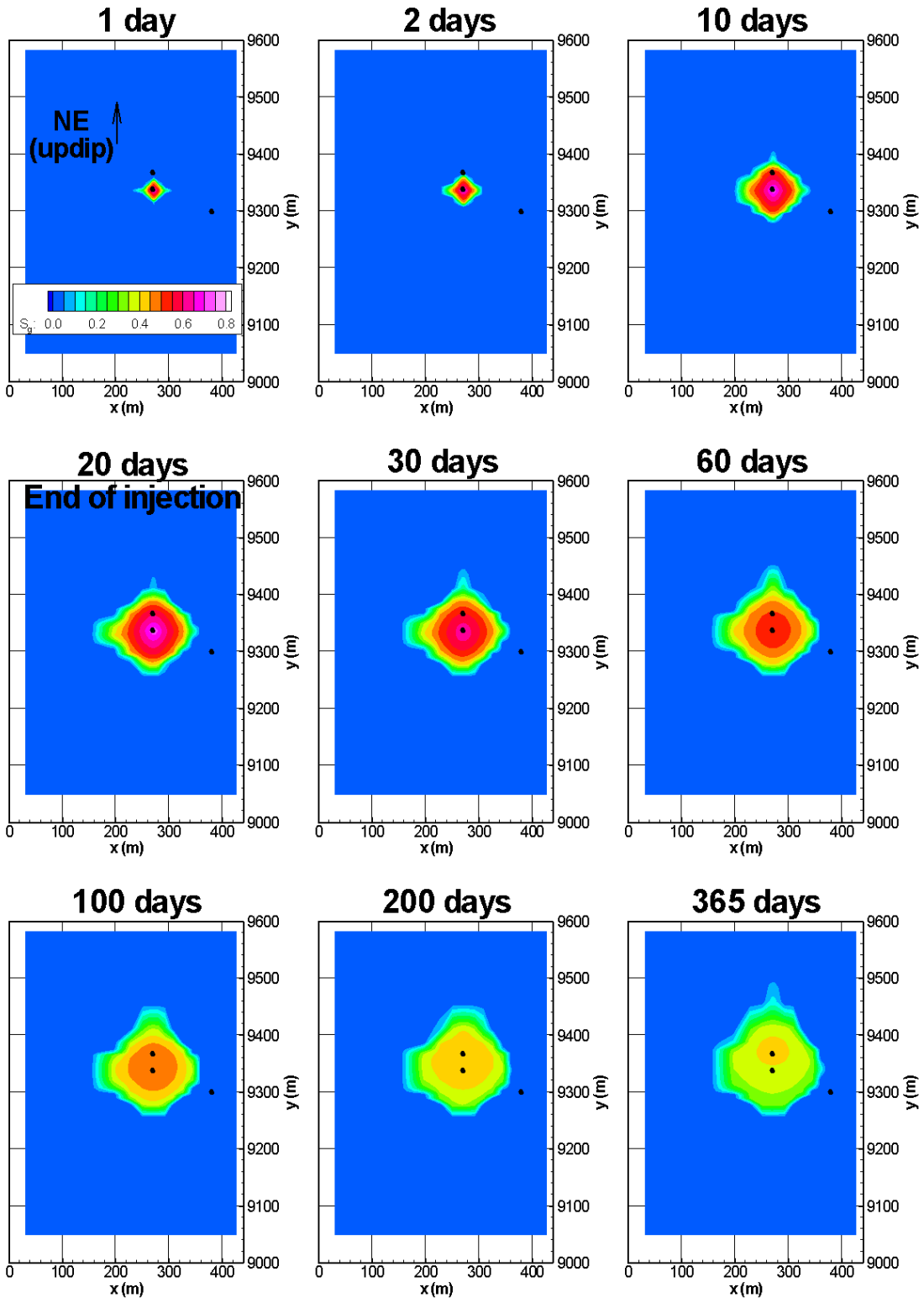

Figure 33. Plan view of gas saturation (S_{CO2}) distribution at the top of the injection interval within the C sand, for a series of times during and after CO_2 injection. The three black dots show the locations of well SGH-3, well SGH-4, and the new injection well (see Figures 31 and 32).

During the South Liberty Field test less than 5,000 tons of CO_2 will be injected into a 6 m thick sand unit at a depth of 1,500 m. As such it is a good limiting case for detection and resolving capabilities of geophysical monitoring techniques. A flow simulation model of the fault block that will be used for the injection was created using geo-statistical realizations of the sand shale distributions based on log data. Log data were used to construct rock properties models that relate the reservoir parameters to geophysical parameters. These relations were used to convert the flow simulation model to geophysical models.

Streaming Potential (SP) measurements

Fluid flow within a porous media can produce an electrical potential due to the separation of ions across flow boundaries. This phenomena is the basis of the Self-Potential (SP) method. SP has been used in geothermal exploration (i.e. Corwin and Hoower, 1979), in earthquake studies (i.e. Fitterman, 1978; Corwin and Morrison, 1977), and in engineering applications (i.e. Ogilvy et al, 1969; Bogoslovsky and Ogilvy, 1973, Fitterman, 1983). Early model studies were based on polarized spheres or line dipole current sources. These techniques provided very little information about the nature of the primary sources. Marshall and Madden (1959) discussed source mechanisms in detail and provided a technique for the solution of coupled flows that incorporated the primary driving potential. Sill (1983) presented an alternative method for the solution of coupled flow problems that explicitly models both the primary flow and the induced secondary electric potential.

The measurement of the SP generated electric fields is a relatively simple and low cost measurement. The ease of the measurement coupled with the fact that the data is generated directly by the flow phenomena suggests a potential technique for low-cost, low-resolution monitoring. To investigate the potential of SP as a CO_2 sequestration monitoring technique the GeoSeq and CCP projects at LBNL undertook numerical model studies to access the magnitude of the SP responses for a variety of scenarios.

The gradient of the electric potential (electric field) produced at a flow boundary by the streaming potential is given by:

$$\nabla \phi = L \frac{\Gamma \mu}{k \sigma}$$

where L is the so called 'coupling coefficient'
Γ is the primary fluid flux, related to the pressure gradient by Darcy's Law
k is solution dielectric constant
σ is the bulk conductivity of the rock
μ is the fluid viscosity

A review of the literature showed that there was very little data on the coupling coefficient, L, for flow of CO_2 within sedimentary rocks. This lead to a program of laboratory studies to measure this parameter. In the following sections we describe the laboratory and the numerical modeling studies. The transcript of a paper submitted to JGR, covering the laboratory experiments conducted as part of this project is given in Appendix 1. A detailed review of the SP method is provided in Appendix 2.

SP laboratory studies

Laboratory studies were done for the streaming potential due to CO_2 injection in Berea sandstone (Lang Stone, Columbus, Ohio). These are the first such measurements for CO_2 to our knowledge. The testing device held a 127 mm long core of 25 mm diameter (Figure 34). Tests were run on two different rock samples. Each sample was saturated prior to testing under vacuum for a period no less than 1 day. The pore fluid for initial saturation was normal tap water, tested to have a resistivity of 125 Ohm-m. The coupling coefficient for the rock/water case was determined both before and after each CO_2 flood of two samples using a low-pressure static head method. Next, liquid CO_2 was allowed to flow over each sample. Test 1 allowed liquid CO_2 to flow through the sample for 1½ hour, while test 2 lasted 1 hour.

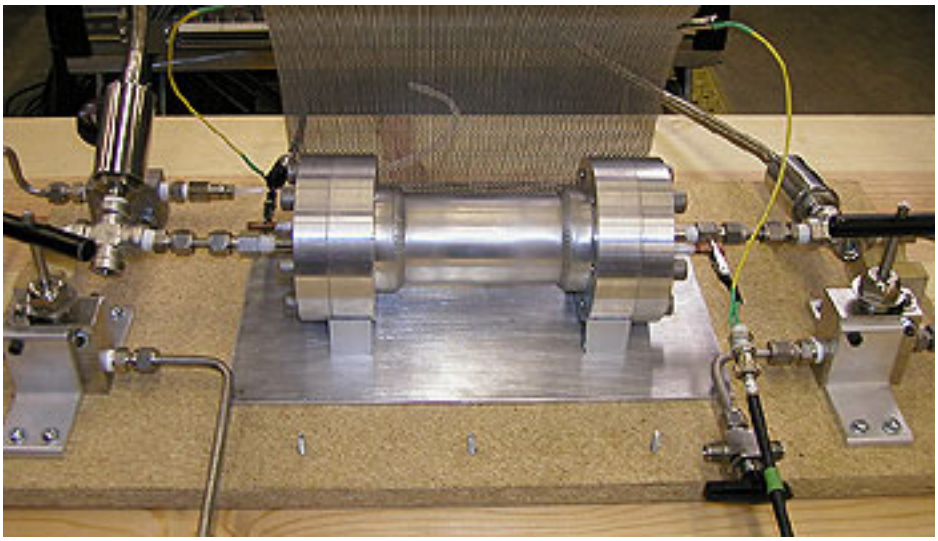

Figure 34. Testing device containing Berea sandstone core. Sample is 127 mm long and 25 mm diameter.

Figure 35 illustrates that the observed potentials and applied pressure changes correlated well throughout the testing.

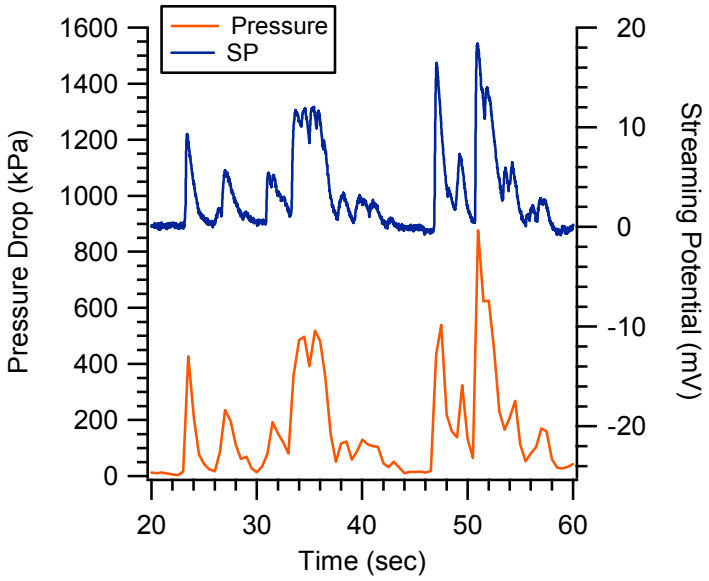

Figure 35. Streaming potential and pressure changes as a function of time as CO_2 is injected into the core sample.

Prior to each CO_2 injection, coupling coefficient information was determined for the Berea sandstone sample saturated with 125 Ohm-m tap water. For these low-pressure tests, results indicate linear correlation of applied pressure and observed potential, as illustrated in Figure 36.

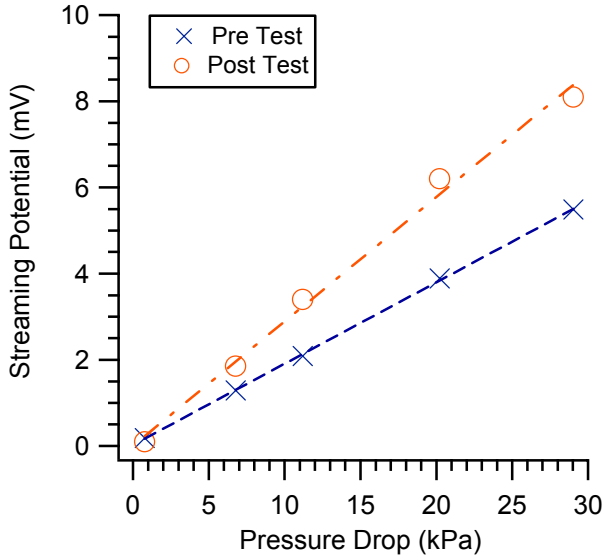

Figure 36. Results for static head testing to determine water-only coupling coefficient both prior to and following CO_2 injection test 2. Resistivity of pore fluid was 125 Ohm-m. Slope of line indicates coupling coefficients of 20 mV/0.1MPa (Pre) and 30 mV/0.1MPa (Post).

When liquid CO_2 was applied to the sample, the water in the sample pore space was displaced, while reacting with the CO_2 to form carbonic acid. The coupling coefficient evolved over time in response to the mixing and displacing of the pore water. Figure 37 shows the coupling coefficient evolution of both tests for the 20 minutes following CO_2 injection.

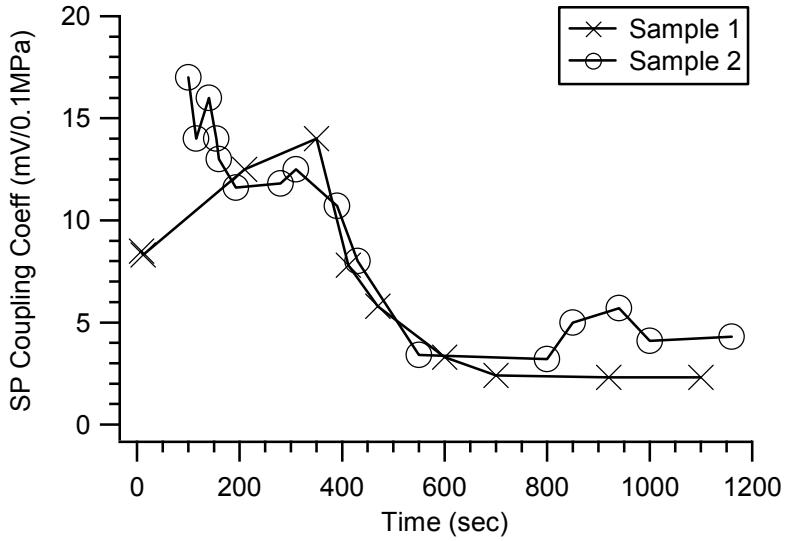

Figure 37. Coupling coefficients as a function of time for the first 20 minutes of CO_2 injection for samples 1 and 2. Coupling coefficient values were steady for times greater than 700 seconds, and remained steady throughout the remaining testing time.

The results of the test are summarized in Table 1. As the CO_2 displaced the water the coupling coefficient decreased. On average, the coupling coefficients observed for steady CO_2 flow is about 10 times lower than for water flow in the same sample. Since the liquid CO_2 coupling coefficient is smaller than that of water, the most effective way to spatially monitor injected CO_2 flow is to monitor the progressing CO_2/water front, where the coupling coefficient is largest.

Table 1. Summary of coupling coefficient results. All units are in mV/0.1MPa.

	Pre-Test (water)	**During (CO2)**	**Post-Test (water)**
Sample 1	45	2.5	15
Sample 2	20	3.5	30

SP modeling

In order to determine the magnitude of the SP response a 2D numerical model based on the geology and configuration of the Liberty Field CO_2 injection test was used. The model consists of a 10 m thick sand unit at a depth of 1,500 m embedded in shale. The resistivity of the sand unit is 2 Ohm-m, while the resistivity of surrounding shale is 1 Ohm-m. The flow rate of CO_2 is 350 kg per second; the viscosity of CO_2 is 0.073 x 10^{-3} Pa-s and the density of CO_2 is 788 kg/m^3 at a temperature of 70° C and a pressure of 30 MPa. The model is shown in Figure 38a. The 2D algorithm developed by Sill (1983) was used. This algorithm assumes the fluid sources to be a line perpendicular to the geologic variation at steady state conditions (constant flow of a single phase fluid).

Figure 39a shows the pressure distribution for the model in Figure 38a with the associated electric potential shown in Figure 39b. In general SP noise sources are on the order of a few to 10s of mV although this number is highly site-specific. SP Signals over 10 mV are considered large.

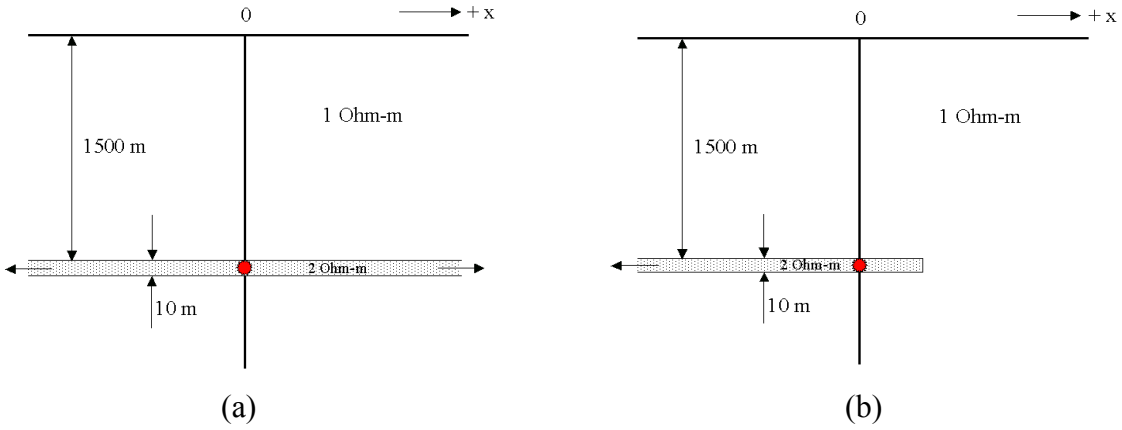

Figure 38. (a) Continuous layer model simulating the Liberty Field geology - 10 m thick sand layer at a depth of 1,500 m. (b) Layer truncated at +300m in x.

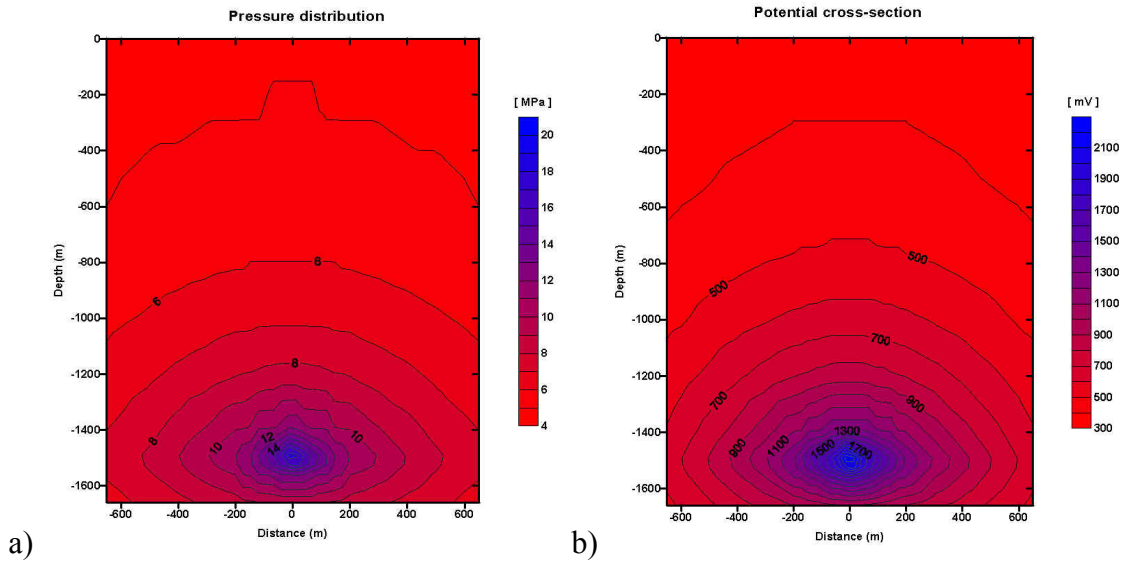

a) b)

Figure 39. (a) Pressure distribution for the model from Figure 38a. (b) Electric Potential cross-section for model in Figure 38a with coupling coefficient, L = -15 mV/atm.

The model shown in Figure 38b has the same parameters as the model in Figure 38a, except that the sand layer is terminated at +300 m. Comparison of results from these two models give an indication the ability of the SP surface measurements to resolve lateral variations in the subsurface flow of CO_2. The largest effect of the layer truncation is to increase the pressure gradient by reducing the flow volume within the layer thus increasing the magnitude of the SP observed at the surface. The truncation of the layer also introduces an asymmetry in the surface SP response (red curve in Figure 40). The response is 10 mV higher on the truncated side than on the continuous side. The ability to differentiate this spatial variation in the signal will depend on the background noise level in the electric fields on the surface.

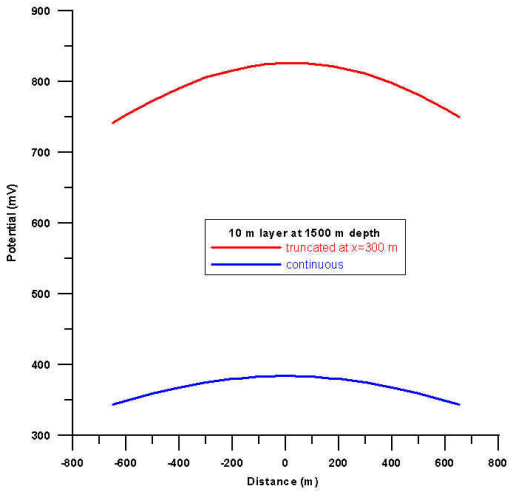

Figure 40. Surface SP response for models shown in Figure 38. Blue curve is for continuous layer; red curve is for the truncated layer.

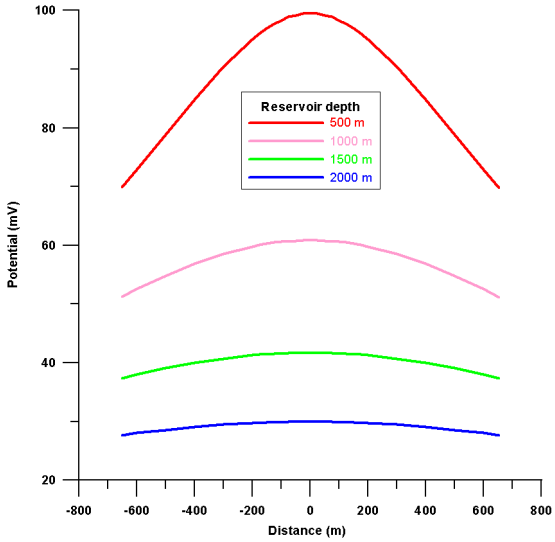

Figure 41. SP response for 100 m thick sand layer at the depth of 500 m, 1,000 m, 1,500 m, and 2,000 m.

The effects of layer depth on the SP response is shown in Figure 41. A 100 m thick sand layer (properties taken from the Liberty test site) is placed at depths of 500 m, 1,000 m, 1,500 m, and 2,000 m respectively. The deeper the sand layer is, the smaller is the signal amplitude on the surface.

Another aspect of interest was how is the SP response influenced by the CO_2 flow rate. Figure 42 illustrates that higher the flow rate the bigger is the SP response. Model used in this figure is 100 m thick layer at the depth of 1,000 m; all other parameters were the same as previous models. The flow rates used in these models were 440 l/s, 293 l/s, and 40 l/s respectively.

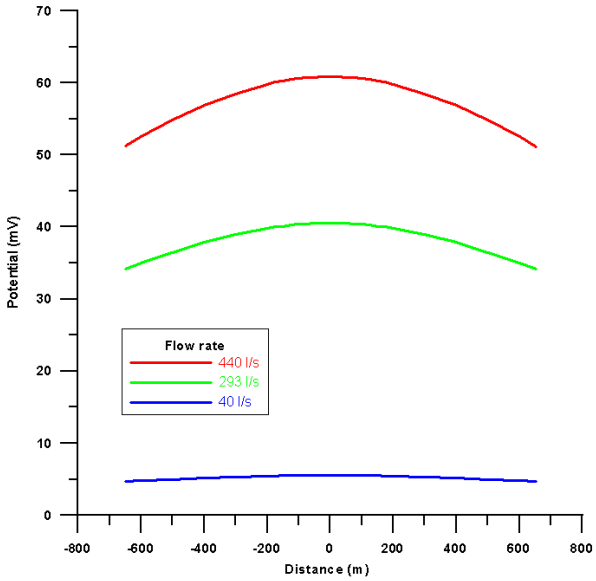

Figure 42. SP response for 100 m thick sand layer at the depth of 1,000 m for the flow rate of 440 l/s, 293 l/s, and 40 l/s.

We also studied the relationship between the thickness of the layer and the SP response. To illustrate this concept we run model with 10 m, 30 m, 100 m, and 200 m thick sand layer at the depth of 1,000 m; all other parameters were unchanged. Figure 43 shows that the amplitude of the SP response is inversely proportional to the thickness of the layer. The largest response was for the 10 m thick layer. This result derives from the fact that the SP response is linearly proportional to the fluid flux, so that for a given injection rate, the thinner layers have a higher fluid flux.

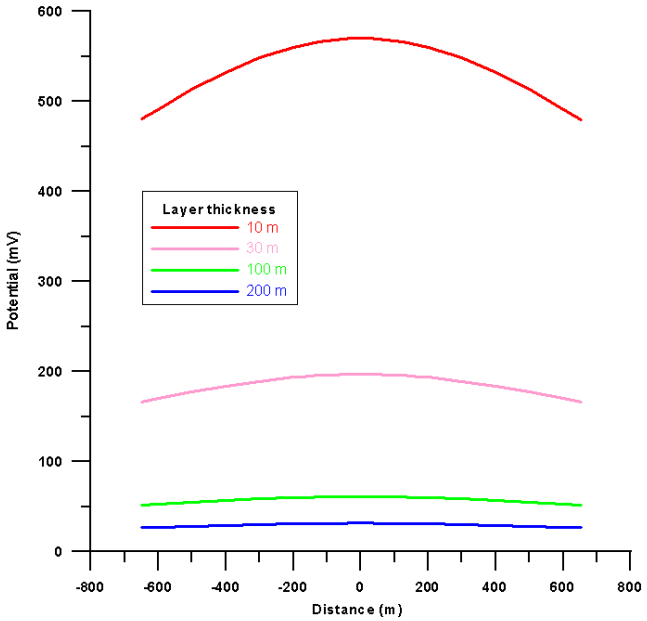

Figure 43. SP response of the 10 m, 30 m, 100 m, and 200 m thick sand layer at the depth of 1,000 m.

We have also investigated how the SP response depends on the coupling coefficient, L, which is shown in Figure 44. The Liberty Field is 10 m thick layer at 1,500 m depth with a lateral extend of 500 – 600 m. Its permeability is 150 milliDarcies, the flow rate is 4 l/s, and the viscosity of CO_2 is 73 μPa-s. The model was run for three different values: 15 mV/atm, 57mV/atm, and 100 mV/atm representing a linear progression from potable water (L=15) to resistive benzene (L=100). Figure 44 shows linear dependence between the cross-coupling coefficient and the SP response.

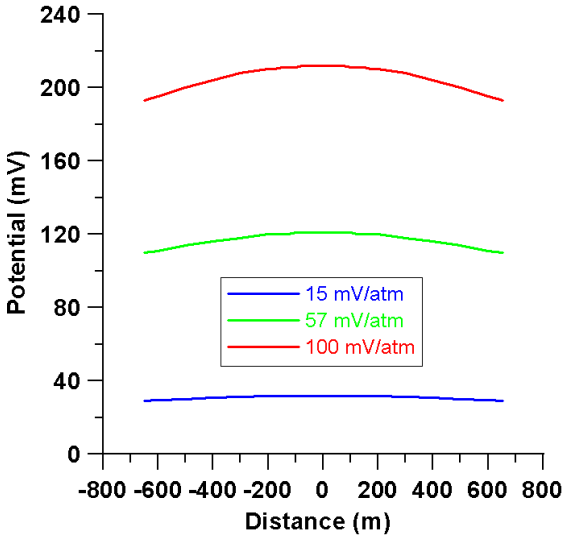

Figure 44. SP response of the Liberty Field reservoir for the coupling coefficient of 15 mV/atm, 57mV/atm, and 100 mV/atm.

Seismic modeling

The size of the region containing CO_2 must be sufficient to generate an interpretable signal at the surface. To put bounds on the minimum size of a CO_2 saturated region that will be detectable by seismic, seismic simulations were performed using a model in which a wedge of CO_2 is placed in a brine saturated unconsolidated sand layer. The CO_2 saturation in the wedge was assumed to be 50%. The wedge is a rough approximation of the shape of the plume formed by CO_2 injected into (or leaking into) the base of the sand layer. The thickness of the sand was varied from 5 m to 100 m. The width of the wedge was based on the size of the first Fresnel zone. Velocity and density models are shown in Figure 45 and Figure 46 respectively. The shale P-velocity was 2,700 m/s and density of 2,160 kg/m^3, while the sand P-velocity was 3,050 m/s and density of 2,285 kg/m^3. The CO_2 wedge P-velocity was 2,530 m/s and a density of 2,260 kg/m^3. The seismic wave center frequency was 30 Hz. For these conditions, the first Fresnel zone diameter is approximately 320 m. Calculations were carried out for wedge widths of 160 m, 320 m, and 480 m, or 0.5, 1.0 and 2.0 Fresnel zones respectively.

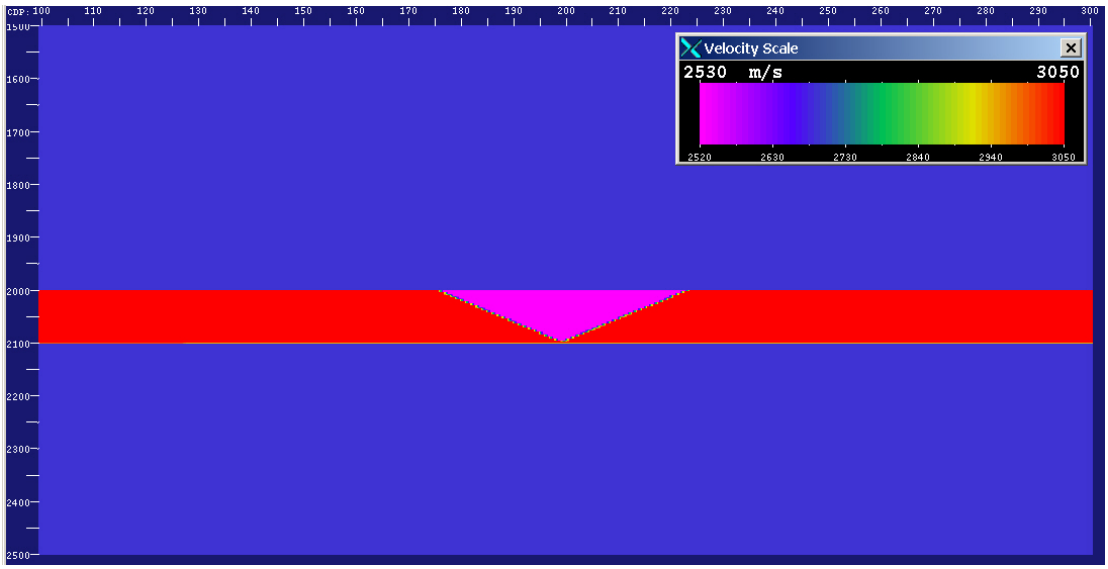

Figure 45. Velocity model of the CO_2 wedge placed in a sand layer at the depth of 2,000 m.

Figure 46. Density model of the CO_2 wedge placed in a sand layer at the depth of 2,000 m.

An acoustic finite difference simulation was carried to produces a zero-offset stacked section followed by Kirchhoff time to produce the plots shown in the following figures.

The model with a 5 m thick sand layer generated no discernable reflection. This is understandable since the layer thickness was on the order of 5% of the seismic wavelength. The result for the 10 m thick layer is shown in Figure 47. The sand layer generates a reflection, but none is observed in the center at the location of the CO_2 wedge. At 2,000 m depth, for the conditions assumed in this model, the impedance difference between the shale and the sand containing CO_2 is almost zero.

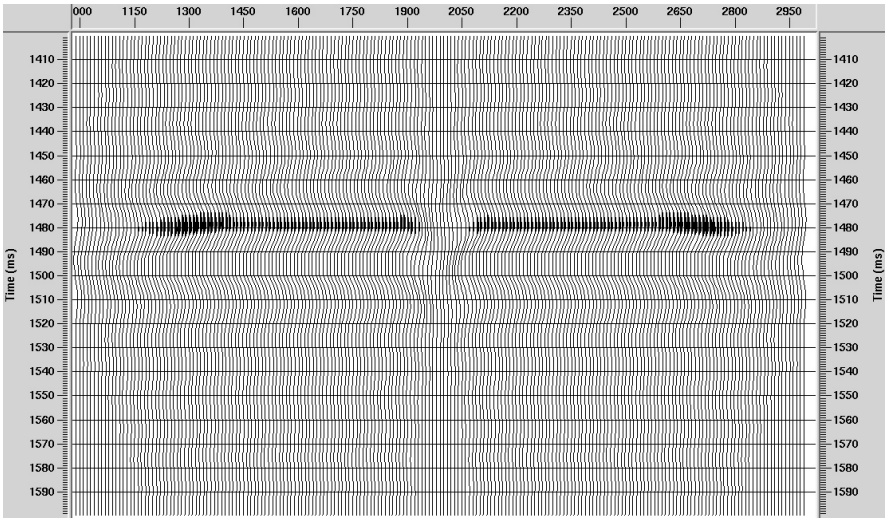

Figure 47. Kirchhoff time migration plot for the CO_2 wedge of 160 m width inside of the 10 m thick layer at the depth of 2,000 m.

Figure 48 shows results for the 30 m thick layer. In this case, the CO_2 wedge is imaged, where the reflections are generated at the interface between the brine saturated sand and the sand containing CO_2. There is a sufficient thickness of brine-saturated sand beneath the CO_2 wedge to generate a reflection.

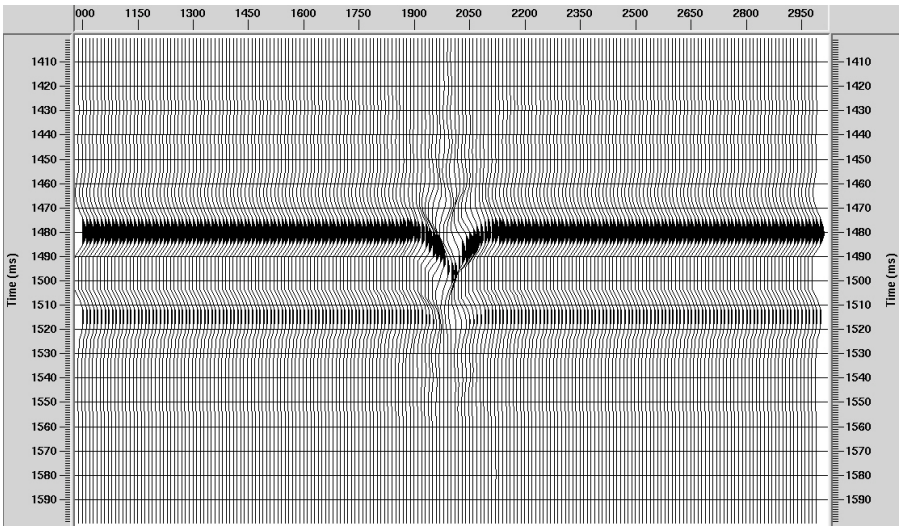

Figure 48. Kirchhoff time migration plot for the CO_2 wedge of 160 m width inside of the 30 m thick layer at the depth of 2,000 m.

For these models the width of the wedge is less than a Fresnel zone and the layer thickness is on the order or less than the layer tuning thickness. Even though the CO_2 wedge is detected, interpretation of the reflection for fluid properties would be difficult because of geometric effects.

A wedge large enough to prevent contamination of reflections by geometrical effects had a width of about 480 m in a 100 m thick sand. The results for this model are shown in Figure 49.

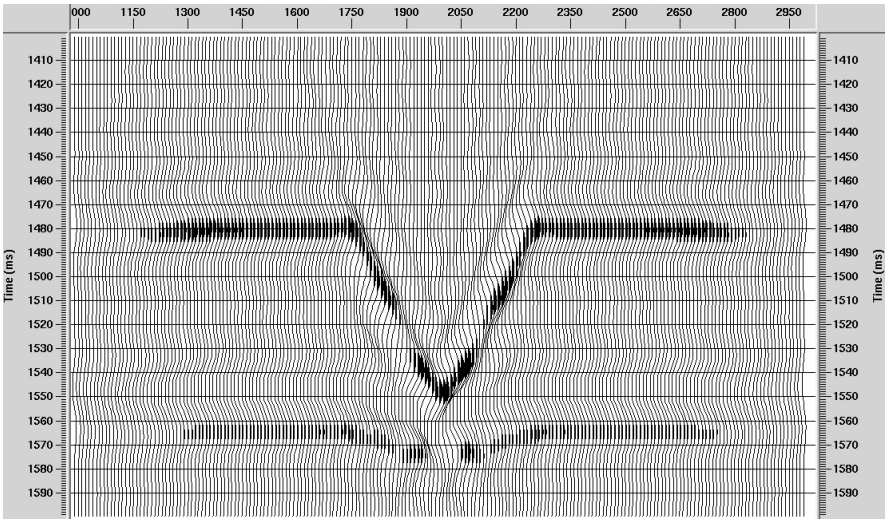

Figure 49. Kirchhoff time migration plot for the CO_2 wedge of 480 m width inside of 100 m thick layer at the depth of 2,000 m.

Gravity modeling

In order to set some limits on the size and depths of CO_2 plumes that can be detected and resolved by surface gravity measurements, the wedge model used in the seismic modeling was also considered for gravity measurements. The rock parameters were taken as general onshore Texas values of density. The surrounding shale was modeled having a density of 2,240 kg/m^3 with the sand layer having 20% porosity and being brine saturated with a density of 2,280 kg/m^3. The 3D wedge of CO_2 saturated sand was considered to be 100% saturated with CO_2, which resulted in a density of 2,200 kg/m^3 for the wedge.

Figure 50 shows three surface response curves of the vertical component of the gravity field for the top of the wedge at 2,000 m depth. The radius of the wedge is 240 m. The simulation was run for 100, 50 and 30 m thick wedges. A reasonable number for land gravity measurement sensitivity levels is 2 micro-gals (μGal). For this depth, even the response of the 100 m thick wedge is below this level. Since the response of the 100 m thick wedge is just below the 2 μGal level, this indicates that amounts larger that 41 days production could be detected but not resolved.

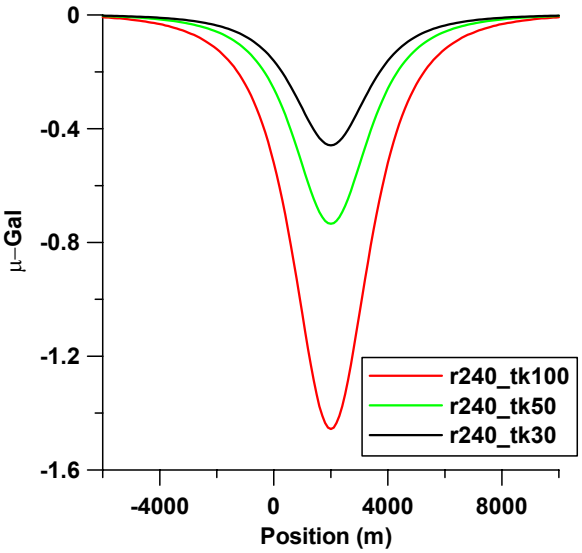

Figure 50. Surface vertical component of gravity measured over a 3D wedge at a depth of 2,000 m. The wedge radius is 240 m with thickness of 100, 50 and 30 m. The wedge with thickness of 100 m contains the equivalent amount of CO_2 produced by a 1000 MW US coal fired power plant in 41 days.

A second set of models with the wedge at 1,000 m depth were run, their responses are shown in Figure 51. With the CO_2 plume at 1,000 m both the 50 m and 100 m thick volumes are detectable. The observed gravity response for the 100 m wedge is large enough to be resolved to some degree.

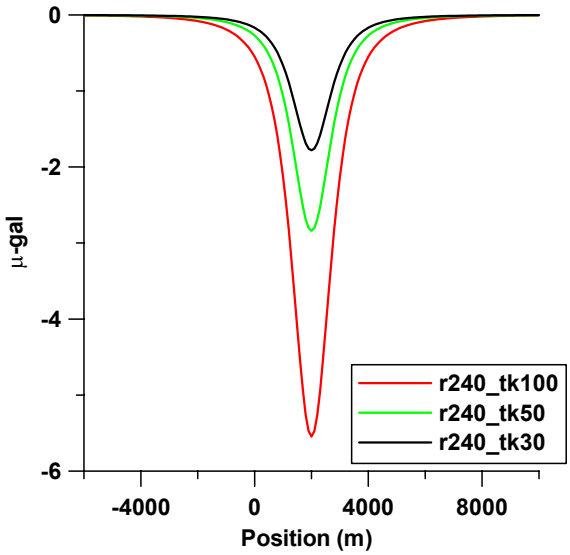

Figure 51. Surface vertical component of gravity measured over a 3D wedge at a depth of 1,000 m. The wedge radius is 240 m with thickness of 100, 50 and 30 m.

Our conclusions to date are that gravity will most likely only be a useful monitoring technique for accumulations of CO_2 with depths on the order of 1km. The volumes

affected for deeper targets will have to be much larger. These results are model specific to the Texas gulf coast.

Tilt calculations

Recent advances in satellite imaging provide new opportunities for using land surface deformation and spectral images to indirectly map migration of CO_2. Ground surface deformation can be measured by satellite and airborne interferometric synthetic aperture radar (InSAR) systems (Zebker, 2000, Fialko and Simons, 2000). Tiltmeters placed on the ground surface can measure changes in tilt of a few nano-radians (Wright et. al., 1998). Taken separately or together these measurements can be inverted to provide a low-resolution image of subsurface pressure changes. While these technologies are new and have not yet been applied for monitoring CO_2 storage projects, they have been used in a variety of other applications, including reservoir monitoring (Vasco et al., 2001) and groundwater investigations (Hoffman et al., 2001, Vasco et al., 2001).

Numerical modeling work done in preparation for the DOE GeoSeq CO_2 field test in the Liberty Field, Texas (scheduled for spring of 2004) provides an illustration of the application of surface deformation as a monitoring tool. The planned test is quite small, injecting a total of 5,000 tons of CO_2 over a 15-20 day period. The injection target is a 12 m sand at a depth of 1,500 m. The target sand lies in a fault block which has sealing faults on three sides and is open to flow on the forth. The presence of the sealing faults acts to confine pressure build up to the fault block, thus increasing the magnitude of the surface deformation.

As CO_2 injection proceeds there is an associated pressure build up in the sequestration unit. This pressure increase translates into stress changes that propagate to the surface and manifest themselves as surface deformation. Figure 52 shows the change in pressure (left panel) within a 15 m thick sand unit at a depth of 1,500 m from the flow simulation model of the Liberty field project as well as the inversion (right panel) of the resulting surface tilt data (Vasco et al., 1998, 2001). The surface tilt is shown in Figure 53. The response is dominated by the fact that the injection occurs in a bounded fault block, thus amplifying the surface tilt above the injection point. The inverted pressure distribution has captured the large-scale pressure increase trending from southwest to northeast across the center of the section.

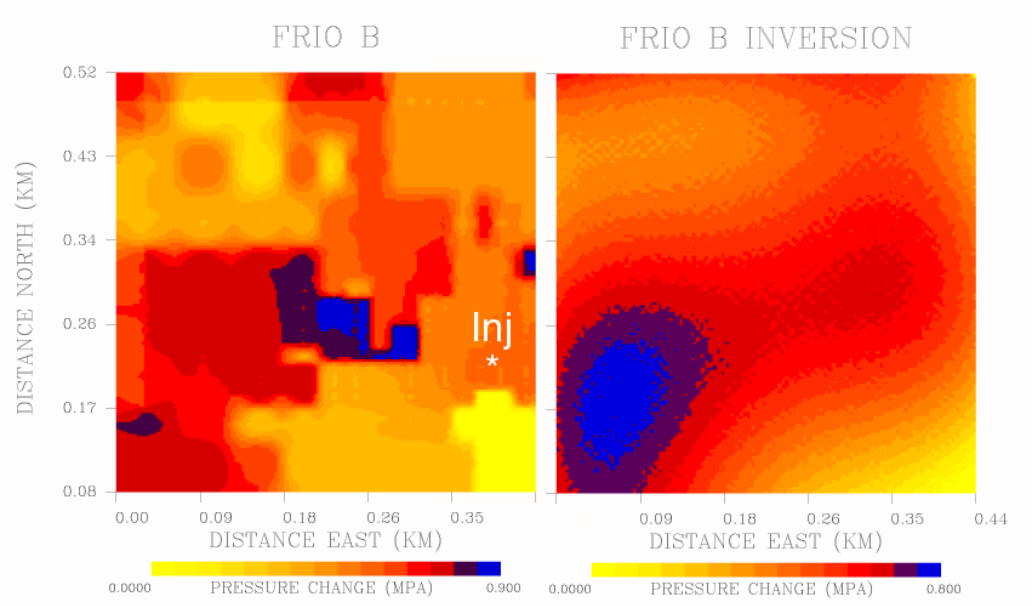

Figure 52. Left panel: Pressure buildup in Frio B sand after 30 days of CO_2 injection. Right Panel: Inversion for pressure change from surface tilt measurements. The section shown is bounded by faults on left, right and top and is open to the bottom. CO_2 concentration is centered on the injector well but permeability variations within the unit cause the maximum pressure increase to be offset from the injection well.

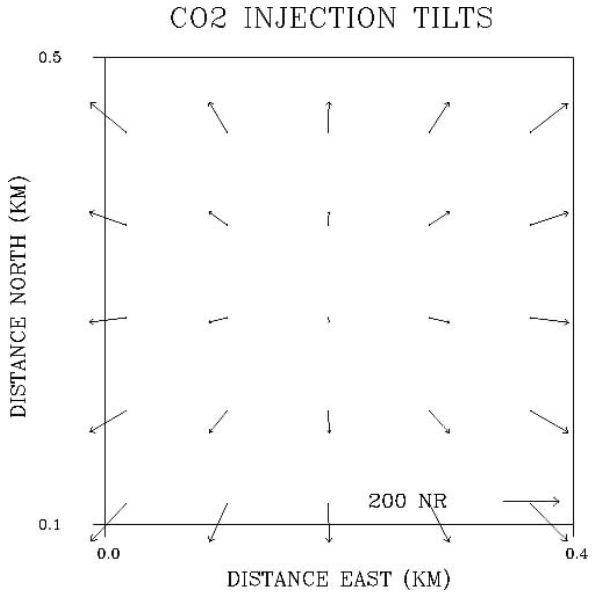

Figure 53. Surface tilt calculated for the pressure change shown in Figure 52 and rock properties representative of the Liberty Field geology. Vectors show the orientation and magnitude of the tilt. The center of the bulge over the maximum pressure is flat and has little tilt. The bounding faults truncate the pressure field and are seen as locations of maximum tilt.

The calculated tilt values are easily observable in the field, since it is possible to achieve an accuracy of 1 nano-radian in field tilt measurements. While the limited spatial extent of this model with the presence of bounding faults (increasing the pressure buildup) dominate the response, it is clear that these measurements can be made in the field over very small quantities of injected CO_2.

The tilt measurements sensitivity to pressure changes provides an ability to map vertically integrated permeability within the injection unit. In this model the injection well is in the lower right corner of the figures. The permeability model was generated as a geostatistical realization. The model has a zone of increased permeability in the lower portions of the model below the main injection sand unit. When this unit is pressured up the pressure front moves ahead of the injected CO_2 and pressurizes the zones with higher permeability. This causes the vertically integrated pressure change to have a maximum toward the center of the model away from the injection well. The tilt responses to this pressure increase therefore maps the high net permeability regions of the injection interval, ahead of the arrival of the CO_2 itself, providing a means of mapping future migration pathways.

Cost Estimates

The costs of geophysical surveys can vary widely depending on surface terrain and the complexity of the survey. In our analysis we consider three methods: seismic, electromagnetic (EM), and gravity. Seismic data is the most costly surface geophysical technique, and, in general, is considered to be an expensive monitoring option. In order to put survey costs in perspective to other costs of sequestration, an estimate was made of the cost of geophysical monitoring of a hypothetical project for sequestering the CO_2 from a 1,000 MW power plant with a 30-year lifetime. Such a plant, with current technology, would produce about 8.6 M metric tones of CO_2 per year. Storage of this in a 100 m thick layer with 20% porosity is assumed. We also assume a final CO_2 saturation of 10% of the pore space (the capacity factor). The depth and temperature of the sequestration formation is assumed to be such that CO_2 density is 800 kg/m^3.

We have considered three scenarios: (1) oil reservoir, (2) brine aquifer – sticky plume, and (3) brine aquifer – slippery plume. The terms sticky and slippery plume refer the the assumed residual CO_2 saturation. A high residual CO_2 saturation results in a plume that does not move much (sticky). An oil reservoir similar to the Schrader Bluff is about 360 km^2 in size. Seismic acquisition costs were assumed to be \$10,000/ km^2, seismic processing costs were assumed to be \$1,000 / km^2. This was the cost for the 3D seismic surveys shot over the Sleipner CO_2 sequestration project (Arts, personal communication). Contractor supplied estimates of land acquisition ofor 3D seismic data in Texas was also comparable. Gravity and EM acquisition costs were assumed to be \$1000/site. The costs for seismic and gravity surveys were calculated at 1, 2, 5, 10, 15, 20, 25, 30, 40, and 50 years. Surveys at 40 and 50 years are done after CO_2 injection is stopped to assure that CO_2 stays in place. Table 2 shows the calculated costs for the Schrader Bluff example.

Table 2. Calculated costs of geophysical data acquisition and processing for an oil reservoir.

Schrader Bluff

				Gravity		Seismic	
Year	Area (km^2)		# sites	Acquisition (\$US)		Acquisition (\$US)	Processing (\$US)
1	360		360	\$360,000.00		\$3,600,000.00	\$360,000.00
2	360		360	\$360,000.00		\$3,600,000.00	\$360,000.00
5	360		360	\$360,000.00		\$3,600,000.00	\$360,000.00
10	360		360	\$360,000.00		\$3,600,000.00	\$360,000.00
15	360		360	\$360,000.00		\$3,600,000.00	\$360,000.00
20	360		360	\$360,000.00		\$3,600,000.00	\$360,000.00
25	360		360	\$360,000.00		\$3,600,000.00	\$360,000.00
30	360		360	\$360,000.00		\$3,600,000.00	\$360,000.00
40	360		360	\$360,000.00		\$3,600,000.00	\$360,000.00
50	360		360	\$360,000.00		\$3,600,000.00	\$360,000.00
Total Cost:				**\$3,600,000.00**		**\$36,000,000.00**	**\$3,600,000.00**
Metric tons of CO2				2.58E+08		2.58E+08	
\$US / ton				**1.40E-02**		**1.53E-01**	

The same estimates were done for a case when CO_2 is stored in a brine aquifer. In this case monitoring would continue 50 more years after the 30 year plant life. Depending on the properties of formation two scenarios are possible: (a) CO_2 stays in place ("sticky plume") or (b) CO_2 still moves ("slippery plume') after injection stops. In the case of a sticky plume the monitoring area stays the same during the post-injection monitoring, while for a slippery plume the monitoring area is increasing. Calculated costs for both of these scenarios are shown in Table 3 and Table 4, respectively.

Table 3. Calculated costs of geophysical data acquisition and processing for a brine aquifer – sticky plume.

Brine Aquifer (sticky plume)								
				Gravity			Seismic	
Year	Area (km^2)		# sites	Alaska ($US)	Texas ($US)		Aquisition ($US)	Processing ($US)
1	18.65		25	$25,000.00	$5,000.00		$190,000.00	$19,000.00
2	27.86		36	$36,000.00	$7,200.00		$280,000.00	$28,000.00
5	51.61		64	$64,000.00	$12,800.00		$520,000.00	$52,000.00
10	87.08		100	$100,000.00	$20,000.00		$880,000.00	$88,000.00
15	120.54		121	$121,000.00	$24,200.00		$1,210,000.00	$121,000.00
20	152.97		169	$169,000.00	$33,800.00		$1,530,000.00	$153,000.00
25	184.74		196	$196,000.00	$39,200.00		$1,850,000.00	$185,000.00
30	216.04		225	$225,000.00	$45,000.00		$2,170,000.00	$217,000.00
40	216.04		225	$225,000.00	$45,000.00		$2,170,000.00	$217,000.00
50	216.04		225	$225,000.00	$45,000.00		$2,170,000.00	$217,000.00
60	216.04		225	$225,000.00	$45,000.00		$2,170,000.00	$217,000.00
70	216.04		225	$225,000.00	$45,000.00		$2,170,000.00	$217,000.00
80	216.04		225	$225,000.00	$40,500.00		$2,170,000.00	$217,000.00
Total Cost:				**$2,061,000.00**	**$407,700.00**		**$19,480,000.00**	**$1,948,000.00**
Metric tons of CO2				2.58E+08	2.58E+08		2.58E+08	
$US / ton				**7.99E-03**	**1.58E-03**		**8.31E-02**	

Table 4. Calculated costs of geophysical data acquisition and processing for a brine aquifer – slippery plume.

Brine Aquifer (slippery plume)								
				Gravity			Seismic	
Year	Area (km^2)		# sites	Alaska ($US)	Texas ($US)		Aquisition ($US)	Processing ($US)
1	18.65		25	$25,000.00	$5,000.00		$190,000.00	$19,000.00
2	27.86		36	$36,000.00	$7,200.00		$280,000.00	$28,000.00
5	51.61		64	$64,000.00	$12,800.00		$520,000.00	$52,000.00
10	87.08		100	$100,000.00	$20,000.00		$880,000.00	$88,000.00
15	120.54		121	$121,000.00	$24,200.00		$1,210,000.00	$121,000.00
20	152.97		169	$169,000.00	$33,800.00		$1,530,000.00	$153,000.00
25	184.74		196	$196,000.00	$39,200.00		$1,850,000.00	$185,000.00
30	216.04		225	$225,000.00	$45,000.00		$2,170,000.00	$217,000.00
40	237.65		256	$256,000.00	$51,200.00		$2,380,000.00	$238,000.00
50	261.41		289	$289,000.00	$57,800.00		$2,620,000.00	$262,000.00
60	287.55		289	$289,000.00	$57,800.00		$2,880,000.00	$288,000.00
70	316.31		324	$324,000.00	$64,800.00		$3,170,000.00	$317,000.00
80	347.94		361	$361,000.00	$64,980.00		$3,480,000.00	$348,000.00
Total Cost:				**$2,455,000.00**	**$483,780.00**		**$23,160,000.00**	**$2,316,000.00**
Metric tons of CO2				2.58E+08	2.58E+08		2.58E+08	
$US / ton				**9.52E-03**	**1.88E-03**		**9.87E-02**	

A summary of total costs for all three scenarios is given in Table 5.

Table 5. Total costs of geophysical data acquisition and processing for assumed plume from a 1,000 MW coal fired power plant operating for 30 years.

	Brine Aquifer ("slippery")	Brine Aquifer ("sticky")	Oil Reservoir
Pre-operational Costs:			
Seismic Survey	$3,828,000	$2,387,000	$4,000,000
Characterization and Performance Prediction	$600,000	$600,000	$150,000
Reservoir Simulation	$15,000	$15,000	$15,000
Gravity Survey	$361,000	$225,000	$370,000
EM Survey	$361,000	$225,000	$370,000
Total:	$5,165,000	$3,452,000	$4,905,000
Operational Costs:			
Seismic Survey	$9,493,000	$9,493,000	$32,000,000
Gravity Survey	$936,000	$936,000	$2,880,000
EM survey	$936,000	$936,000	$2,880,000
Total:	$11,365,000	$11,365,000	$37,760,000
Closure Costs:			
Seismic Survey	$15,983,000	$11,935,000	$8,000,000
Gravity Survey	$1,519,000	$1,125,000	$720,000
EM Survey	$1,519,000	$1,125,000	$720,000
Total:	$19,021,000	$14,185,000	$9,440,000
Total:	$35,551,000	$29,002,000	$52,105,000
Metric tons of CO_2	2.58E+08	2.58E+08	2.58E+08
Total cost / CO_2 Ton:	$0.138	$0.112	$0.202

These costs represent a reasonable, though idealized, estimate for a generic monitoring program. Given the variation in terrain, climate, and sequestration formation complexity it is not unreasonable to assume that actual costs may vary by as much as a factor of 2.

Cost analysis indicates that other types of geophysics (gravity, electromagnetic) would be potentially an order of magnitude less expensive than seismic monitoring. However, when the costs of monitoring are put in the perspective of the total cost of a sequestration project where the cost of CO_2 capture alone (not including injection) is on the order of 50 to 100 $US/ tonne the cost savings from using, for example, gravity versus seismic is not (in our opinion) justified given the decreased resolution and insensitivity to small changes in CO_2 saturation. This latter point, insensitivity to small changes in CO_2 saturation is quite significant in that only the seismic technique has the ability to detect a few percent change in CO_2 saturation in a very thin (1-5 m) zone above a reservoir that would be the early warning signs of leakage.

The other geophysical methods considered here definitely have a role to play in fine-scale detailed quantitative analysis of a reservoirs performance, particularly in a petroleum reservoir with multiple fluid components were seismic alone does not contain enough information to uniquely determine all the fluid saturations (Hoversten et al. 2003). The other techniques may also be used more frequently, as a fill-in between seismic surveys to provide assurance that CO_2 movement in the reservoir is proceeding in the planned direction. However, seismic will always be an integral part of a monitoring strategy with the time-interval between seismic surveys dictated by model based risk analysis of the CO_2 propagation times in the formations above a storage reservoir, so that the seismic surveys can catch a leak sufficiently early to mitigate it.

Results and Discussion

The difference in the vertical component of gravity on the surface caused by CO_2 injection over a 20-year period for the Schrader Bluff model is on the order of 2 μGal, which is in the noise level of the field survey (Hare, 1999). The negative change in the response is caused by increased CO_2 saturations reducing the bulk density of the reservoir. The spatial variations in the changes in the vertical component of gravity as well as the vertical gradient of the vertical component of gravity directly correlate with the spatial variations in the net density changes within the reservoir. Again, the magnitude of the signal measured in the field (2–10 EU) is above the gradiometer accuracy (0.5–1 EU), but the difference between initial conditions and 20 years into CO_2 injection is very small (~0.1 EU). If the noise levels of measurements of the changes in dG_z/dz could be reduced by permanent sensor emplacement and continuous monitoring gravity and gradient measurements may offer a tool for monitoring.

Borehole measurements of gravity just above the reservoir do produce measurable change in the vertical component of gravity that could be used to map lateral distributions of injected CO_2. The changes in dG_z/dz measured in the borehole are below the ability of current technology to distinguish. However, current work on borehole gravity tools may change this situation within the next few years. The difference in both the borehole gravity response and the vertical gravity gradient (dG_z/dz) measured in vertical profiles within boreholes clearly identifies the position of the reservoir. The sign of the change reflects the changes in the local densities caused by either water or CO_2.

There is a clear change in seismic amplitude associated with the reservoir caused by the changes is water and CO_2 saturation. In addition, there is a change in the seismic AVO effects. Both seismic amplitude and AVO can be exploited to make quantitative estimates of saturation changes. Forward calculations using Zoeppritz equation for both 2005 and 2020 models support this argument.

The electrical resistivity of reservoir rocks is highly sensitive to changes in water saturation. This high sensitivity to water saturation in a reservoir can be exploited by electromagnetic (EM) techniques where the response is a function of the electrical resistivity of the formation. Of all the possible combination of EM sources and measured EM fields one system combines both relative ease of deployment with high sensitivity to reservoirs of petroleum scale and depth. This technique uses a grounded electric dipole that is energized with an alternating current at a given frequency to produce time varying electric and magnetic fields that can be measured on the earth's surface. To simulate such an EM system we have calculated the electric field on the surface of the Schrader Bluff model using 100 m electric dipoles operating at 1 Hz an measuring the resulting electric field at a separation of 2 km in-line with the transmitting dipole. The generated electric field for the Schrader Bluff model, using only a small portable generator is an order of magnitude above the background electric field (noise) at the operating frequency of 1 Hz. This means that synchronous detection of the signal combined with stacking can

recover signal variations to better than 1 percent. There is a direct one-to-one correspondence with the change in S_w and the change in the electric field amplitude. While this signal level is low, it can be measured give the signal-to-noise ratio of the data. While this represents a potential low-cost monitoring technique it is best suited for CO_2 – brine systems where there is a one-to-one correlation between the change in water saturation and the change in CO_2 saturation (since $S_w + S_{CO2} = 1$). In petroleum reservoir such as Schrader Bluff the presence of hydrocarbon as additional fluids eliminates the one-to-one correlation between changes in S_w and changes in S_{CO2}. This type of EM technique has not yet been employed as a monitoring tool within the petroleum industry. However, EM technology is currently the subject of a significant upsurge in industry interest. Several commercial contractors are now offering this technique as a survey tool, most notably, in the offshore environment where it is currently being used as an exploration tools (Ellingsrud et al. 2002). The equipment and service providers exist to apply this technique for monitoring in the future.

The SP method has the potential to be a low-cost low-resolution method of large scale reservoir monitoring. Compared to other geophysical techniques relatively little quantitative work has been done on the SP technique. To quantify the magnitude of the SP response caused by CO_2 injection considerable effort has been done on laboratory measurements of the SP caused by CO_2 injection into sandstone. These studies have shown that the coupling coefficients for CO_2 are large enough to cause an SP signal that could be measured at the surface above injection sites, depending on the injection rate, depth of the reservoir and the geologic setting. As the CO_2 displaces the water the coupling coefficient decreases. On average, the coupling coefficients observed for CO_2 flow is about 10 times lower than that for water flow in the same sample. However, the maximum SP signal comes from the flood front where CO_2-water mixing is occurring, and the SP coupling coefficient is increased by a factor of 3. This provides a benefit in that the signal source region is spatially confined to the advancing front, allowing higher spatial resolution.

We have simulated the SP response of a CO_2 sequestration scenario in 2D, based both on the Liberty Field and Sleipner CO_2 injection tests. Modeling results show that injection of CO_2 to the Liberty Field formation would produce a response, which is easily measured with the SP method. The Sleipner results are less encouraging, however, a number of key parameters are poorly defined and definitive statements about the potential of SP as a monitoring tool cannot yet be made.

REFERENCES

Archie, G. E., 1942, The electrical resistivity log as an aid in determining some reservoir characteristics: Trans., AIME 146, pp. 54-62.

Arts, R. 2003, Personal communication.

Bogoslovsky, V.A., and Ogilvy, A.A., 1973, Deformations of natural electric fields near drainage structures: Geophysical Prospecting, **21**, p. 716-723.

Castagna, J.P, Swan, H. W., Forster, J.F., 1998, Framework for AVO gradient and intercept interpretation, Geophysics, **63**, pp. 948-956.

Corwin, R.F., and Hoower, D.B., 1979, The self-potential method in geothermal exploration: Geophysics, **44**, p. 226-245.

Corwin, R.F., and Morrison, H.F., 1977, Self-potential variations preceding earthquakes in central California: Geophys. Rev. Lett., **4**, p. 171-174.

Doughty, C., and Pruess, K., 2003, Modeling supercritical CO_2 injection in heterogeneous porous media: Proceedings, TOUGH Symposium, May 12-14, 2003.

Dvorkin, J. and Nur, A., 1996, Elasticity of high-porosity sandstones: Theory of two North Sea data sets: Geophysics, **61,** pp. 1363-1370.

Eiken, O. 2003 Personal communication

Ellingsrud, S., Eidesmo, T., Johansen, S., Sinha, M.C., MacGregor, L. M., Constable, S., 2002, Remote sensing of hydrocarbon layers by seabed logging (SBL): Results from a cruise offshore Angola: The Leading Edge, **21**, pp. 972-982.

Fialko, Y., and Simons, M., 2000, Deformation and Seismicity in the Coso Geothermal Area, Inyo County, California: Observations and Modeling Using Satellite Radar Interferometry, Journal of Geophysical Research, **105**, 21,781-21,793.

Fitterman, D.V., 1978, Electrokinetic and magnetic anomalies associated with dilatant regions in a layered earth: J. Geophys. Res., **83**, B12, p. 5923-5928.

Fitterman, D.V., 1983, Self-potential surveys near several Denver Water Department dams: U.S. Geol. Surv. Open file rept. 82-470.

Gasperikova, E., Hoversten, G.M., Ryan, M.P., Kauahikaua, J.P., Newman, G.A., and Cuevas, N., 2003, Magnetotelluric investigations of Kilauea volcano, Hawai'i. Part I: Experiment design and data processing. Journal of Geophysical Research, in review.

Hare, J.L., Ferguson, J.F., and Aiken, C.L.V., 1999, The 4-D microgravity method for waterflood surveillance: Amodel study from the Prudhoe Bay reservoir, Alaska: Geophysics, **64**, 78-87.

Hoffmann, J., Zebker, H. A., Galloway, D. L., and Amelung, F., 2001, Seasonal subsidence and rebound in Las Vegas Valley, Nevada observed by synthetic aperture radar interferometry, Water Resources Research, **37**, 1551.

Hoversten, G., M., Gritto, R., Washbourne, J., Daley, T., M., 2003, Pressure and Fluid Saturation Prediction in a Multicomponent Reservoir, using Combined Seismic and Electromagnetic Imaging. Geophysics, (in press Sept-Oct 2003).

Hovorka, S.D. and P.R. Knox, 2002, Frio Brine Sequestration Pilot in the Texas Gulf Coast, Sixth International Conference on Greenhouse Gas Control Technologies (GHGT-6), Kyoto, Japan, 1-4 October, 2002.

Jouniaux, L., Bernard, M.L., Pozzi, J.P., and Zamora, M., 2000, Electrokinetic in Rocks: Laboratory Measurements in Sandstone and Volcanic Samples: Phys. Chem. Earth (A), **25**, 329-332

Kreitler, C. W., Akhter, M. S., Donnelly, A. C. A, and Wood, W. T., 1988, Hydrology of formations for deep-well injection, Texas Gulf Coast: The University of Texas at Austin, Bureau of Economic Geology, unpublished contract report, 204 p.

Landro, M., 2001, Discrimination between pressure and fluid saturation changes from time-lapse seismic data: Geophysics, **66**, pp. 836-844.

Loucks, R. G., Dodge, M. M., and Galloway, W. E., 1984, Regional controls on diagenesis and reservoir quality in lower Tertiary sandstones along the lower Texas Gulf Coast, *in* McDonald, D. A., and Surdam, R. C., eds., Clastic diagenesis: American Association of Petroleum Geologists Memoir **37**, p. 15–46.

Macpherson, G. L., 1992, Regional variation in formation water chemistry; major and minor elements, Frio Formation fluids, Texas: American Association of Petroleum Geologists Bulletin, **76**, no. 5, pp. 740–757.

Marshall, D.J., and Madden, T.R., 1959, Induced polarization, A study of its causes: Geophysics, **24**, p. 790-816.

Ogilvy,A.A., Ayed, M.A., and Bogoslovsky, V.A., 1969, Geophysical studies of water leakages from reservoir: Geophys. Prosp., **17**, p. 36-62.

Popta, J.V., Heywood, J.M.T., Adams, S.J., and Bostock, D.R., 1990, Use of borehole gravimetry for reservoir characterization and fluid saturation monitoring: SPE 20896, p. 151- 160.

Shuey, 1985, A simplification of the Zoeppritz equations: Geophysics, **50**, pp. 609-614.

Sill, W.B., 1983, Self-potential modeling form primary flows: Geophysics, **48**, p. 76-86.

Thomsen L.A., Brady J.L., Biegert E., Strack K.M., 2003, A Novel Approach to 4D Full Field Density Monitoring, SEG workshop.

Vasco D W, Karasaki K.; Myer L. R, 1998, Monitoring of fluid injection and soil consolidation using surface tilt measurements. Journal of Geotechnical and Geoenvironmental Engineering,**124**, pp.29-37.

Vasco, D.W. Karasaki, K. and Kiyoshi, K., 2001, Coupled Inversion of Pressure and Surface Deformation Data. Water Resources Research, pp. 3071-3089.

Wright, C., Davis, E., Minner, W., Ward, J., Weijers, L., Schell, E., and Hunter, S., 1998, Surface Tiltmeter Fracture Mapping Reaches New Depths-10,000 Feet and Beyond?, Society of Petroleum Engineering #39919.

Zebker, H., 2000, Studying the Earth with Interferometric Radar, Computing in Science and Engineering, **2**, 52-60.

APPENDIX 1

THE STREAMING POTENTIAL COUPLING COEFFICIENT OF LIQUID CARBON DIOXIDE INJECTED INTO WATER SATURATED BEREA SANDSTONE

Jeffrey R. Moore, Steven D. Glaser, H. Frank Morrison, and G. Michael Hoversten

University of California, Berkeley
440 Davis Hall
Berkeley, CA 94720
e-mail: moore@ce.berkeley.edu

ABSTRACT

The streaming potential coupling coefficient was determined for a liquid carbon dioxide flood of a water-saturated sample of Berea sandstone. The coupling coefficient for the rock/water case was determined both before and after each CO_2 flood of three samples using a low-pressure static head method. Next, liquid CO_2 was allowed to flow through each sample. As the CO_2 displaced the water the coupling coefficient decreased. At longer times, when all mobile pore water was displaced, the coupling coefficient maintained a steady state, and was lower than that for water by an order of magnitude. The results of this testing reveal a coupling coefficient of 30 mV/0.1MPa, for 125 Ω-m water flow through the sample, and 3.0 mV/0.1 MPa for liquid CO_2 flow. Calculated zeta potentials are –3.4 mV using water as the pore fluid and -1.7×10^{-6} mV for liquid CO_2. We propose that the lower coupling coefficient for CO_2 flow is primarily a result of changes in zeta potential, since changes in pore fluid resistivity and viscosity would act to increase the coupling coefficient. Zeta potential for the liquid CO_2/mineral interface is a function of the low polarity and lack of mobile ions associated with liquid CO_2. We find no anomalous

two-phase liquid/gas effects, which may have augmented single-phase streaming potentials by many times. We propose that although CO_2 gas may have been present for some of the higher pressure drop events, the low gas fraction (or quality) of the two-phase mixture did not lead to any significant anomalous or augmented observations. Implications of this work include spatial and temporal monitoring of CO_2 injectate in subsurface reservoirs and the identification of flow paths, with the recommendation being to attempt to image the advancing CO_2/water front, where the coupling coefficient is higher.

INTRODUCTION

As a palliative to global warming due to the buildup of greenhouse gasses in the atmosphere, several schemes have been proposed to inject liquefied atmospheric CO_2 into the earth for sequestration. For these schemes to be approached rationally, the location of the injectate within the earth must be mapped through time. This requires the measurement of a directly coupled physical parameter in real time, and an inversion method that can take place in near real time. Self-potential (SP), in this case streaming potential (or electrokinetic potential), is a widely recognized method for identifying flow paths through rock and rock/soil matrices (Bogoslovsky and Ogilvy, 1970; Corwin and Hoover, 1979; Wurmstich and Morgan, 1994). We present experimental data of streaming potentials resulting from the interaction of rock and liquid CO_2.

Past work in the field is limited to the study of fluids with polar molecules where the secondary electrical current is carried primarily in the pore fluid, with surface conduction contributing in special cases. Furthermore, quantitative research regarding streaming potentials is still somewhat limited to a few scenarios. Specifically, we find no reference to past work documenting the streaming potential response to CO_2 flow in a porous medium. This situation was tested experientially for the first time, the results of which follow.

THE ELECTRIC DOUBLE LAYER

Electrokinetic phenomena is based on the existence of an electric double layer (EDL) at the liquid-matrix interface where a diffuse mobile layer of ions can be effectively *dragged* away from their adsorbed immobile counterparts under a pore pressure gradient (Jouniaux et al, 1999). Since many minerals have negatively charged surfaces, a diffuse layer of positive ions from the local pore solution bond to the mineral surface, keeping the interface electrically neutral. The electric double layer is composed of 2 regions, the Helmholtz Layer and the Gouy Chapan zone (Ishido and Mizutani, 1981, Morgan, et al, 1989). The Helmholtz layer contains those ions adsorbed to the mineral surface and essentially fixed, and is subdivided into the Inner Helmholtz Plane (IHP), which contains those ions directly in contact with the mineral surface, and the outer Helmholtz place (OHP), which contains those ions affixed to the mineral surface but not directly contacting it. The Gouy-Chapman zone is the mobile layer of hydrated ions that are subject to frictionally induced displacement under a pore pressure gradient. Figure 1 shows a diagram of the EDL and describes the zeta potential, which is defined as the potential on the shear plane, or that plane separating the OHP and the Gouy-Chapman mobile zone.

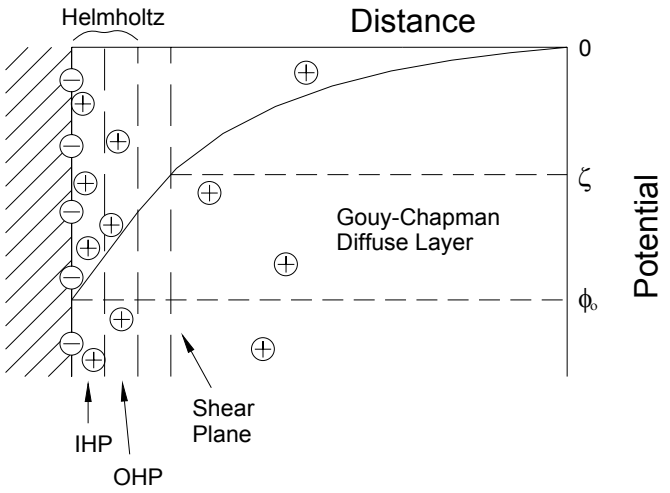

Figure 1: The electric double layer including the inner Helmholtz plane (IHP), the outer Helmholtz plane (OHP), and the Gouy-Chapman diffuse zone. The zeta potential is defined as the potential on the shear plane between the fixed Helmholtz layer and the mobile Gouy-Chapman zone.

Frictional movement of ions in the Gouy-Chapman zone creates a charge imbalance, which is known as the convection current. This induces an Ohmic return current, or the conduction current. These currents are equal and opposite everywhere inside the media, and equalizing them reveals the Helmholtz-Smoluchowski equation (Overbeek, 1952, Nourbehecht, 1963).

$$\nabla V = -\frac{\varepsilon_r \varepsilon_o \zeta}{\eta \sigma} \nabla P \,, \tag{1A}$$

or, as commonly written,

$$\Delta V = -\frac{\varepsilon_r \varepsilon_o \zeta}{\eta \sigma} \Delta P \,, \tag{1B}$$

where ε_r is the relative dielectric constant of the fluid, ε_o is the dielectric constant of vacuum, ζ is the zeta potential, σ is the conductivity of the fluid, and η is the dynamic viscosity of the fluid. The quantity ($\varepsilon_r \varepsilon_o \zeta / \eta \sigma$) is known as the streaming potential coupling coefficient, Cc.

Precise quantitative interpretation of streaming potential data can sometimes be difficult, as the coupling coefficient must be previously determined for each specific scenario. Furthermore, the governing equation (Eqn. 1) is only applicable for a specific set of flow conditions including laminar, steady, fully-established flow (Reichardt, 1935), conditions that are not always achieved in real rock samples.

Differences in coupling coefficients between water and liquid CO_2 allow imaging of the location of each pore fluid present in the reservoir. Furthermore, spatial variations in streaming potentials can give an accurate portrayal of the advancing CO_2 injectate front. Since the CO_2 molecule is non-polar, we hypothesized prior to the experiment that observed streaming potentials would be quite small, if at all observable. This follows since the fluid solution is lacking any electrolyte, or mobile ions in solution. Furthermore, the non-polar molecule cannot bind to and *drag* away any mobile ions that happened to be in the pore solution, therefore limiting the convection current created. Finally, the very high resistivity solution can impede the return path of any convection current. By way of comparison, the water molecule, and a water/electrolyte solution, is ideal for

accommodating the streaming potential phenomena. The polarity of the water molecule makes it effective at both conducting current in an electrolyte solution, as well as binding to mobile ions, to frictionally move them in the direction of fluid flow. The result of this contrast in fluid polarities will reveal a contrast in field-observable potentials, thereby facilitating imaging of the advancing CO_2/water boundary.

For this suite of experiments, we have analyzed the temporal response of induced potentials and investigated their relationship with applied pressure drop using both liquid CO_2 and 125 Ω-m water as the pore fluid. We have also examined the effects of the displacement of in situ pore water by the CO_2, since this is most likely to be the situation found in the field. Our tests use intact specimens of representative reservoir rock, in this case Berea sandstone (Lang Stone, Columbus, Ohio).

EXPERIMENTAL SETUP

The testing device was constructed to hold a 127 mm long core of 25 mm diameter rock. The geometry insures that the flow is essentially one dimensional, allowing the proper application of the simplified Eqn. 1B. The device (Figure 2) was constructed using aluminum tubing into which is inserted a sample surrounded by a 3 mm thick Teflon sleeve. Aluminum end caps hold cylindrical PEEK plastic plugs having baffled ends. As the end caps are tightened, the baffled ends of the PEEK plugs press against, and flare out, the end portions of the insulating Teflon sleeve. In this way the sample and the pore fluid are insulated from direct contact with the aluminum shell. The sample is coated with silicon RTV adhesive prior to being inserted into the Teflon sleeve to ensure that flow is not allowed at this interface. The electrodes are copper screws threaded through the PEEK plugs and tightened against the sample to ensure good contact. Electrode drift was not encountered during testing, nor was electrode polarization a problem. A perforated stainless steel shield insulated the device from stray electrical noise.

Prior to testing, each sample was saturated under vacuum for a period no less than 12 hours. The specimen was initially saturated with normal tap water having a resistivity of 125 Ω-m. Temperature stable (-60 - 250°C) pressure transducers at each end of the testing

device recorded absolute fluid pressures, which were digitized every 0.5 sec. A 14-bit dynamic range data acquisition system recorded potentials across the specimen at 200 samples per second for 1280 second sweeps. The testing system was thoroughly cleansed using a degreasing agent prior to each test, and carefully de-aired using a vacuum pump.

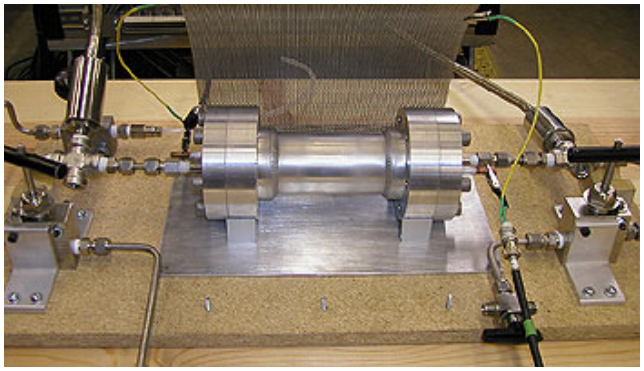

Figure 2: Testing device - specimen is 127 mm long and 25 mm diameter housed within an aluminum cell, and surrounded by a Teflon sleeve. Pressure transducers on each end record absolute pressure, while streaming potentials are noted by an independent data collection system.

Fluid pressure drop across the sample was regulated using a system of manually controlled valves. At the inlet, the CO_2 line was split with a T, and on one end a valve could be opened to atmosphere to allow control of inlet pressure. In our testing, this valve was not used, and the CO_2 inlet pressure of 6.5 MPa was determined by that of the storage tank. As flow rates during the experiment were small, the pressure change in the large (22 kg) siphon-tube tank was negligible over the course of the experiment. At the outlet of the testing device, a multi-turn valve regulated the outlet pressure. Changing the aperture of this needle valve (Autoclave Engineers) was sufficient to control the pressure drop across the sample. During testing this valve had a tendency to freeze as the exiting liquid CO_2 changed phase. To combat this, an additional valve was installed 1 meter downstream of the outlet valve, and this second valve held open at a constant aperture. This provided a small reservoir to absorb some of the rapid pressure fluctuations created by the phase change of the injectate. Both valves were periodically warmed with a heat gun.

The streaming potential coupling coefficient was investigated prior to each CO_2 flood using 125 Ω-m tap water as the pore fluid. Water was applied to the sample using a static head method where a large container of water was placed at different elevations above the sample, and the driving head measured. The maximum attainable pressure drop using this method was 30 kPa.

Immediately prior to CO_2 injection, a backpressure was applied to the sample with water to minimize pressure drop (and phase transition) as the 6.5 MPa liquid CO_2 entered the system. The test then began as liquid CO_2 was allowed to flow. The inlet valve was initially fully opened, while the outlet valve was closed. Opening the outlet valve to various apertures then regulated the pressure drop across the sample. Test 1 allowed liquid CO_2 to flow through the sample for 1½ hour, while tests 2 and 3 lasted 1 hour.

Following each CO_2 flood, the samples were re-saturated with tap water under vacuum for a period of at least 12 hours. The static head method was again used to investigate the coupling coefficient for the water resaturated specimen. Coupling coefficient information was thus noted prior to, during, and following each CO_2 flood.

RESULTS

For the initial low-pressure water floods, results indicate linear correlation of applied pressure and observed potential, as illustrated by Figure 3.

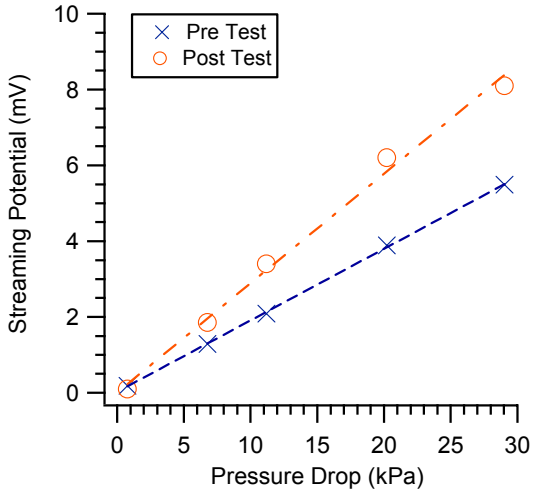

Figure 3: Results for static head testing to determine water/rock coupling coefficient prior to, and following CO_2 injection test 2. Resistivity of the pore fluid was 125 Ω-m. Calculations indicate coupling coefficients of 20mV/0.1MPa (Pre) and 30 mV/0.1MPa (Post).

During the liquid CO_2 flood, the water in the sample pore space was displaced, while reacting with the CO_2 to form weak carbonic acid. The coupling coefficient evolved over time in response to the mixing and displacement of the pore water. Figure 4 shows the coupling coefficient evolution for all tests during the initial 20 minutes of CO_2 injection.

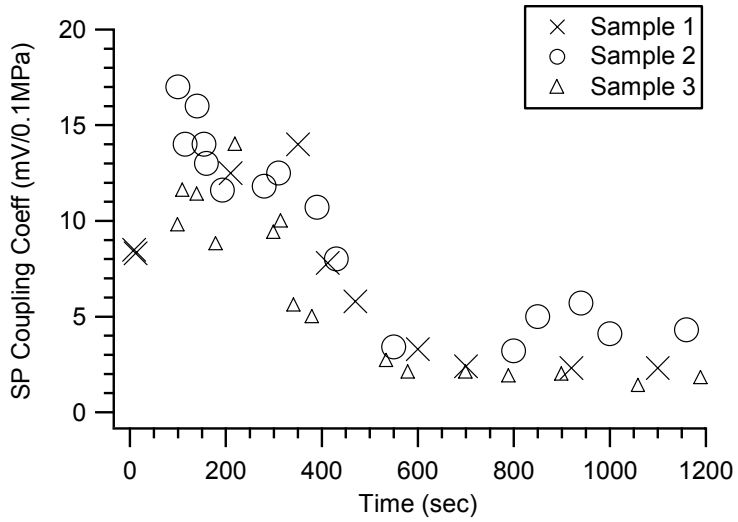

Figure 4: Coupling coefficient evolution with time for samples 1, 2, and 3. Only the first 20 minutes of the >1 hour total sweep are shown. Coupling coefficient values were steady for times greater than about 700 seconds, and remained steady throughout the remaining >40 minutes of testing.

Throughout testing, observed potentials and applied pressure drop correlated well in the temporal sense, as illustrated by Figure 5. The information shown is an arbitrary portion of data taken from the beginning of the final 20 minutes of test 3, and shows the accuracy of the coupling. We measured an accurate potential response from both low and high frequency pressure changes (Figure 6), although some resolution of the pressure drop data was lost due to the low data sampling rate. High-frequency pressure fluctuations were created by frozen condensate blocking the outlet valve. The addition of the second valve 1 meter downstream from the outlet valve steadied these fluctuations and created a signal typified by that in Figure 5. Coupling coefficients were determined at many points throughout each sweep by noting the change in observed potential for a given fluid pressure change event.

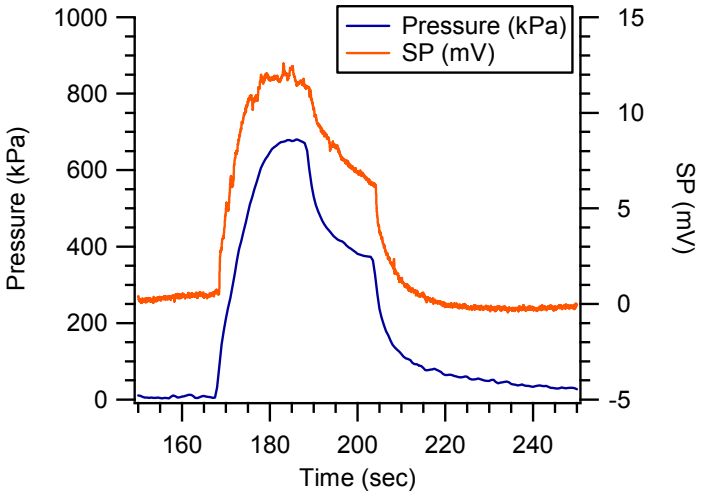

Figure 5: Representative portion of potential/pressure data for a low-frequency event, test 3.

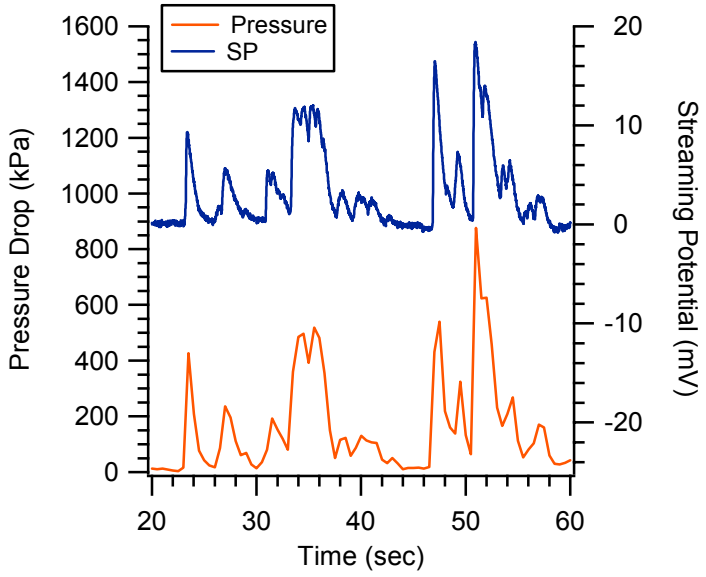

Figure 6: Potential/pressure data for high-frequency events, test 2. Results indicate the ability of coupled potentials to respond instantaneously to pore pressure changes.

The correlation between coupling coefficient and pressure drop is illustrated in Fig. 7. Recall that the Helmholtz-Smoluchowski equation only applies for fully established flow. Many authors have observed that at higher pressure drops the coupling coefficient

decreases in response to this condition being violated (Reichardt, 1935, see Morgan et al, 1989 for a review). We note a slight change in coupling coefficient with pressure drop, but observe that the coupling coefficient tends towards an asymptotic value as pressure drop increases.

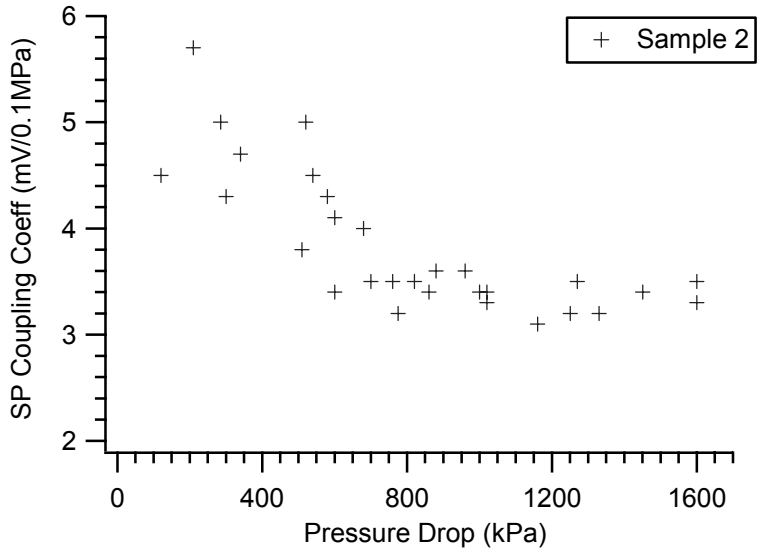

Figure 7: Correlation of coupling coefficient with pressure drop for test 2. Data is taken from time after water/CO_2 mixing is assumed to be complete, or that time greater than about 700 sec (see Figure 4).

Table 1 summarizes the results of the tests performed. We find that, on average, the coupling coefficients observed for CO_2 flow is about 10 times lower than that for 125 Ω-m water flow in the same sample.

Table 1: Summary of coupling coefficient results. All units are mV / 0.1 MPa.

	Pre-Test (water)	During (CO_2)	Post-Test (water)
Test 1	45	2.5	15
Test 2	20	3.5	30
Test 3	35	2.0	40

DISCUSSION

We propose that the lower coupling coefficient for CO_2 flow is a result of both competing changes in pore fluid resistivity, dielectric constant, and viscosity, as well as changes in zeta potential, which is affected by the lower-polarity pore fluid. A dramatic increase in fluid resistivity (~10^6) and decreased fluid viscosity (~15) will act to increase the coupling coefficient, while the decrease in dielectric (~55) will compete to decrease the coupling coefficient. The result of this competition, however, will be an expected coupling coefficient increase of near five orders of magnitude. On the contrary, the experimental results presented herein note a decrease in coupling coefficient by 1 order of magnitude. Such a results would require a decrease in zeta potential of nearly 6 orders of magnitude.

Material parameters affecting the coupling coefficient (Eqn. 1) for water and liquid CO_2 are presented in Table 2. Using these inputs, we have back-calculated the zeta potential for both water and liquid CO_2 flow. We find that the zeta potential calculated for the water / solid case was –3.4 mV, a result within the range of expected values (Morgan et al, 1989, Lorne et al, 1999, Fagerlund and Heinson, 2002). The calculated zeta potential for the liquid CO_2 flow scenario was found to be -1.7 x 10^{-6} mV. The smaller (less negative) zeta potential calculated for liquid CO_2 is indicative of the interface characteristics between the mineral grain and liquid CO_2. One factor influencing the zeta potential is the pore fluid polarity. Since the carbon dioxide molecule is non-polar, its ability to shear charge is significantly reduced. Furthermore, liquid CO_2 will not contribute mobile ions to carry charge or form a charged EDL, factors required for coupled electric flows.

Table 2: Dielectric constant, resistivity (Ω-m), and viscosity (mPa-s) for water and liquid CO_2. Zeta potentials are calculated from observed coupling coefficients. Source: 'Lange's Handbook of Chemistry', 1992.

	Water	**CO_2 (l)**
ε_o	8.85x 10^{-12} F/m	8.85x 10^{-12} F/m
ε_r	80	1.45

ρ	125 Ω-m	10^8 Ω-m
η	1.00 mPa-s	0.071 mPa-s
ζ (calculated)	*-3.4 mV*	*-1.7×10^{-6} mV*

The calculated zeta potential indicates a fundamental change to the rock / fluid interface between the water and liquid CO_2 tests. Yet, the observation of an electric potential in a non-conductive medium may indicate lasting effects of adsorbed pore water. That is, as the pore water is displaced, the coupling coefficient and zeta potential quickly decrease. At longer times, the coupling coefficient is steady, and may represent that time when no more pore water is permanently displaced. However, the observation of the coupled potential may indicate that a layer of adsorbed water is still present on the mineral surface. In this scenario, shearing may be occurring between the hydrated mineral surface and the liquid CO_2, and conduction current carried by the surface layer of bound water. Additionally, the reaction of water and CO_2 to form carbonic acid yields mobile hydrogen ions. If the bound pore water were actually transformed to a weak acid, then mobile cations would be available to carry charge at this interface. In either scenario, the pore fluid (liquid CO_2) is no longer carrying the conduction current, and this duty is accepted by surface charge. This result invalidates the Helmholtz- Smoluchowski equation as shown in Equation 1, which assumes that surface conductivity is minimal, and raises fundamental questions about the rock / liquid interface in the presence of a non-conducting pore fluid.

To include effects of surface conduction a modification of the Helmholtz- Smoluchowski equation has been proposed which includes the formation factor, F, or the ratio of the fluid resistivity (conductivity) to the sample resistivity (Jouniaux and Pozzi, 1995).

$$Cc = \frac{\varepsilon_r \varepsilon_o \zeta}{\eta \sigma} \frac{F}{F_o}, \tag{2}$$

$$\frac{F}{F_o} = \frac{1}{1 + \rho_f \sigma_s F_o}, \tag{3}$$

Where F is the formation factor, F_o is the formation factor when surface conduction is absent, ρ_f is the fluid resistivity, and σ_s is the surface conductivity. In laboratory investigations, this correction is only applicable for very high fluid sensitivities and

negligible for fluid resistivities < ~400 Ω-m (Lorne, et al, 1999). For sandstones, a correction ratio of 0.5 can be assumed for high fluid resistivities (Lorne et al, 1999). This rough assumption causes a correction to the calculated coupling coefficient and zeta potential, reducing the coupling coefficient by half, and augmenting the zeta potential by a factor of 2.

The mixing and replacement of the initial water by liquid CO_2 is indicated by changes in the coupling coefficient, as seen in Figure 4 by that period of time when the coupling coefficient is decreasing. The observed time required to complete mixing and replace the mobile pore water with liquid CO_2 is about 10-15 minutes. This value is dependent on the flow rate of the entering liquid CO_2, the topology of the connected pore space, and on the difference in viscosity between the two fluids. For longer times the coupling coefficient was observed to be steady, indicating and end to mobile water displacement from the pore space.

In our tests, there were no anomalous readings which would have indicated two-phase liquid/gas flow. Many authors have reported that gas bubbles within testing systems, or increased gas fractions in two-phase liquid/gas systems have the effect of increasing the coupling coefficient by up to an order of magnitude (Marsden and Tyran, 1986; Wheatall and Marsden, 1987; Sprunt et al, 1995). We expect the passing of gas bubbles to be somewhat erratic, and two-phase effects would then manifest themselves as rapid and random fluctuations in the value of the coupling coefficient. We noted no such fluctuations, but rather that the coupling coefficient was nearly constant following the initial mixing period of water and CO_2, and slightly dependent on the pressure drop (see Figures 4 and 7). Furthermore, we observed no appreciable temperature change on the outside of the aluminum test cell, as would be expected with a phase change of liquid CO_2 to gas.

Referring to the phase diagram for CO_2 shown in Figure 8, at 20°C a pressure of about 5.85 MPa is required to remain in the single-phase liquid regime. In our tests, the inlet pressure was held constant at 6.5 MPa, but the maximum tested pressure drop across the sample was

up to 1.5 MPa. Therefore, the absolute pressure may have dropped below the required liquid pressure, and entered the two-phase regime. To this end, we cite experimental work by Wheatall and Marsden (1987) who noted the streaming potential coupling coefficient as a function of steam quality (in this case the volume gas fraction). Their results indicate appreciable changes to the coupling coefficient only at gas fractions approaching 0.95 and higher. For the lower gas fractions, especially those below 0.5, the coupling coefficient varied little and variations are within the range of experimental uncertainty. Therefore, we conclude that although there may have been a CO_2 gas phase present for some of the larger pressure drops (those above 650 kPa), the volume gas fraction was so small that appreciable two-phase effects were not noted.

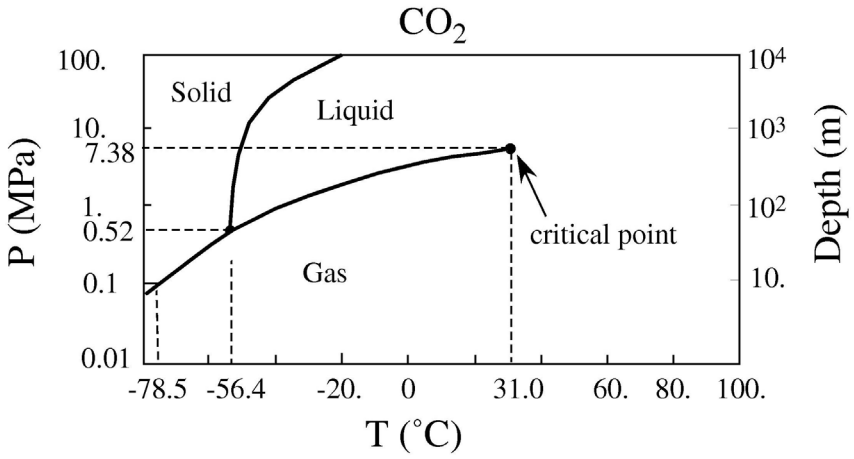

Figure 8: Phase diagram for carbon dioxide (source: Oldenburg and Unger, 2003).

The changes observed in the coupling coefficients measured prior to, and following CO_2 injection are likely artifacts of variations in experimental conditions between each test, including variations in the clay content of the Berea sandstone, and variations in the amount of time each sample was submerged in water. For example, sample 1 was saturated and left submerged for a period of nearly 2 weeks before the CO_2 test was completed. In contrast, samples 2 and 3 were saturated for around 1 day prior to the CO_2 flood. Furthermore, although each sample was cored from the same block of Berea sandstone, variations in the frequency of silty interbeds were encountered. Not only affecting the clay content of each sample, these interbeds may have caused variations in the

sample permeability, each factor contributing differences in calculated coupling coefficients under similar conditions.

The primary result of this work is to note the contrast between the coupling coefficient for water and that for liquid CO_2 flow through the same rock sample. On average, we observed a 10 times decrease in the coupling coefficient for liquid CO_2 compared to that for water. Given this information, researchers may decide the most effective way to image flow paths of liquid CO_2 injectate. Noting that the liquid CO_2 coupling coefficient is lower than that of water, we propose that the most effective way to spatially monitor injectate flow is to monitor the progressing CO_2/water front, where the coupling coefficient is highest.

CONCLUSION

The results presented herein note the contrast in streaming potential coupling coefficient when liquid CO_2 is injected into a water saturated sample of Berea sandstone. In three tests on different rock samples, we found that, on average, the coupling coefficient for liquid CO_2 was about 10 times lower than that for 125 Ω-m tap water. Absolute values of these coupling coefficients were average 30 mV/0.1MPa for water flow through the sample, and about 3 mV/0.1MPa for liquid CO_2 flow. Calculated zeta potential for the rock/liquid CO_2 interface was found to be -1.7×10^{-6} mV, where as the zeta potential calculated for the rock/water interface was –3.4 mV. Implications of this work include the monitoring of CO_2 injectate in subsurface reservoirs using streaming potentials.

ACKNOWLEDGEMENTS

This work was supported in part by the U.S. Department of Energy contract no. DE-AC07-991D13727 to the Idaho National Engineering and Environmental Laboratory.

REFERENCES

Bogoslovsky, V., and Ogilvy, A., Application of geophysical methods for studying the technical status of earth dams, *Geophysical Prospecting, 18*, 758-773, 1970.

Corwin, R., and Hoover, D., The self-potential method in geothermal exploration, *Geophysics, 44*, 226-245, 1979.

Fagerlund, F., and Heinson, G., Detecting subsurface groundwater flow in fractured rock using self-potential (SP) methods, *Environmental Geology, 43*, 782-794, 2002.

Ishido, T., and Mizutani, H., Experimental and theoretical basis of electrokinetic phenomena in rock-water systems and its applications to geophysics, *Journ. Geophys. Res., 86*(B3), 1763-1775, 1981.

Jouniaux, L., and Pozzi, J., Streaming potential and permeability of saturated sandstones under triaxial stress: consequences for electrotelluric anomalies prior to earthquakes, *Journ. Geophys. Res., 100*(B6), 10,197-10,209, 1995.

Jouniaux, L., Bernard, M., Pozzi, J., and Zamora, M., Electrokinetic in rocks: laboratory measurements in sandstone and volcanic samples, *Phys. Chem. Earth (A), 25*(4), 329-332, 2000.

Lorne, B., Perrier, F., and Avouac, J., Streaming potential measurements 1. Properties of the electric double layer, *Journ. Geophys. Res., 104*(B8), 17,857-17,877, 1999.

Marsden, S. S., and Tyran, C. K., The streaming potential generated by flow of wet steam in capillary tubes, *Proceedings, 11th Stanford Workshop on Geothermal Reservoir Engineering*, 225-229, 1986.

Morgan, F., Williams, E., and Madden, T., Streaming potential properties of westerly granite with applications, *Journ. Geophys. Res., 94*(B9), 12,449-12,461, 1989.

Nourbehecht, B., Irreversible thermodynamic effects in inhomogeneous media and their applications in certain geoelectric problems, Ph.D. thesis, Mass. Inst. of Tech., Cambridge, 1963.

Oldenburg, C. M., and Unger, J. A., On Leakage and Seepage from Geologic Carbon Sequestration Sites: Unsaturated Zone Attenuationl, *Vadose Zone Journal, 2*, 287-296, 2003.

Overbeek, J. Th., *Colloid Science vol. I, Irreversible Systems*, Elsevier, New York, 1952.

Reichardt, H., Elektrisches Stroemungspotential bei turbulenter stroeming, *Phys. Chem. Ser. A, 174*, 15, 1935.

Sprunt, E. S., Mercer, T. B., and Djabbarah, N. F., Streaming potential from multiphase flow, *Geophysics, 59*, 707-711, 1994.

Wheatall, M. W., and Marsden, S. S., Two phase streaming potentials, *Proceedings, 12th Stanford Workshop on Geothermal Reservoir Engineering*, 1987.

Wurmstich, B., and Morgan, F., Modeling of Streaming Potential Responses Caused by Oil Well Pumping, *Geophysics*, *59*, 46-56, 1994.

APPENDIX 2

THE SELF-POTENTIAL METHOD

Introduction

The self-potential (SP) method is based on measurement of naturally occurring potential differences generated mainly by electrochemical, electrokinetic, and thermoelectric sources. SP has been used in geothermal exploration (i.e. Corwin and Hoower, 1979), in earthquake studies (i.e. Fitterman, 1978; Corwin and Morrison, 1977), and in engineering applications (i.e. Ogilvy et al, 1969; Bogoslovsky and Ogilvy, 1973, Fitterman, 1983). The earlier model studies were based on polarized spheres or line dipole current sources. These techniques provided very little information about the nature of the primary sources. Marshall and Madden (1959) discussed source mechanisms in detail and provided a technique for the solution of coupled flows that incorporated the primary driving potential. Sill (1983) presented an alternative method for the solution of coupled flow problems that explicitly models both the primary flow and the induced secondary electric potential.

Governing Equations

The general equation for coupled flows can be written (Marshall and Madden, 1959)

$$\Gamma_i = \sum_j L_{ij} X_j \qquad (1)$$

where the fluxes Γ_i (charge, matter, heat, etc.) are related to the various forces X_j (gradients of electric potential, pressure, temperature, etc.) through the coupling coefficients L_{ij}. For many practical applications of coupled flows, we are concerned with secondary electric current flows and potentials that are driven by some other primary flow.

Equation (1) can be re-written as follows:

$$Q = C_{11} \nabla P + C_{12} \nabla \Phi \qquad (2)$$

$$J = C_{21} \nabla P + C_{22} \nabla \Phi \qquad (3)$$

where Q and J are primary (heat or fluid) flow and current flow respectively

C_{11} = K, the hydraulic conductivity

$C_{22} = \sigma$, the electrical conductivity

$C_{12} = C_{21}$ are the cross-coupling coefficients

The cross-coupling terms in equations (2) and (3) are typically much smaller than the primary flow terms. If we neglect these terms, the equations decouple into more familiar Darcy's Law and Ohm's Law. In the absence of external electrical current sources we note that the current is divergenceless:

$$\nabla \cdot J = \frac{dq}{dt} = 0$$

where q is electrical charge.

Applying this relationship to equation (3) and doing some algebra we obtain:

$$-\nabla \cdot (\sigma \nabla \Phi) = \nabla C_{21} \cdot \nabla P + C_{21} \cdot \nabla^2 P \qquad (4)$$

This is a classical dc conduction equation with electrical potential and conductivity on the left hand side and induced current sources on the right hand side. Equation (4) shows that induced current sources occur if a) the cross-coupling coefficient C_{21} changes in the direction of the primary flow and/or b) there are primary flow sources ($\nabla^2 P \neq 0$). Because the effects of secondary electric potential on fluid or heat flow are small the pressure (or temperature) distribution may be obtained by a straightforward application of Darcy's Law or the heat conduction equation.

Historical application of the method

Self-potential anomalies of widely varying amplitude, polarity, and spatial extend have been reported from several geothermal areas. Examples include positive anomalies of as much as 2300 mV in amplitude and about 1 km in width measured on Kilauea volcano, Hawaii by Zablocki (1976); a negative anomaly of about 200 mV amplitude and about 1 km in width at the northwest edge of Dunes thermal area (Combs and Wilt, 1976); a steep-sided positive anomaly of about 30 mV amplitude and 2 km in width over the Mud

Volcano area of Yellowstone National Park (Zohdy et al., 1973); a dipolar anomaly covering over 15 km and about 900 mV peak-to-peak amplitude over a postulated resurgent dome in Long Valley, California (Anderson and Johnson, 1976); a negative anomaly of about 60 mV amplitude and 3 km in width centered over the Leach Hot Springs area of Grass Valley (Corwin, 1976), a well-developed dipolar anomaly of about 160 mV peak-to-trough amplitude; and peak-to-trough distance of about 7 km at Cerro Prieto geothermal field in Baja California (Corwin et al. ,1980; and Fitterman and Corwin, 1982); negative SP anomalies, down to –1700 mV, with high gradients (1.83 mV/m) on Mount Pelee volcano due to a hydrothermal system, and a positive SP anomaly, up to 200 mV caused by two active hot springs (Zlotnicki et al., 1998).

Inversion of SP data of seepage through a dam in Karlsruhe, Germany determined voltage cross-coupling coefficients for sand and gravel on the order of 7×10^{-8} V/Pa (Wurmstich, 1995). In a study of a leakage from a landfill in Goeda, Germany Wurmstich (1995) showed that increasing electrical fluid conductivity caused by contamination decreased the SP response by up to 20 mV. He also reported that hydraulic fracturing produces enhanced, measurable SP responses when compared to injection at the same rate.

Vertical subsurface fluid flow, heat flow, or both in a presence of a vertical fault, contact or a fracture zone separating regions of different electrokinetic or thermoelectric coupling coefficients can generate surface SP anomalies. The same holds true for horizontal flow in the presence of a horizontal boundary, or components of flow parallel to boundaries at any orientation.

Streaming potentials are generated by electrokinetic processes that are directly related to moving fluids in porous media such as rock. Consequently, measurement of streaming potentials may provide important means of monitoring subsurface flow and give some insight into the rate and direction of fluid flow in an oil reservoir.

Electrokinetic potential (streaming potential) can be expressed as follows:

$$E_k = \frac{\xi \, \Delta P \, k \, \rho}{4 \, \pi \, \eta}$$

where ξ is adsorption (zeta) potential of double layer (solid-liquid)

ΔP is pressure difference

k is solution dielectric constant

ρ is resistivity

η is viscosity

Most of these parameters are available for a petroleum reservoir. The most difficult one to obtain is the zeta potential. There have been some numerical studies by Pride and Morgan (1991) for NaCl and quartz. They reported that quartz could acquire a zeta potential of at least –50 mV.

Morgan et al. (1989) reported on laboratory measurements of the streaming potential properties of Westerly granite. Experiments with pressure differences to 3 atm (0.3 MPa) were preformed. The coupling coefficients at the high-pressure levels (3 atm = 0.3 MPa) were 2-4 times smaller than at low-pressure differences (0.1 atm = 0.01 MPa). Experiments were therefore executed at 0.05 atm (5 kPa) pressure level. For Westerly granite with resistivity of 2 kΩm they measured a zeta potential of –38 mV with 10^{-3} N KCl. They reported for 1:1 electrolyte the ratio of the streaming potential coupling coefficient to fluid resistivity was –4 mV/(atm Ωm) and for 2:1 electrolytes –2 mV/(atm Ωm). The effect of temperature was small (0.05 mV/°C) and indicated that the zeta potential is approximately temperature independent for the temperature range they studied. They estimated that a typical geothermal reservoir of 250° C could possibly give a 125 mV anomaly.

Ishido and Mizutani (1981) found that streaming potential coupling coefficients of quartz in 10^{-3} N KNO_3 to increase in magnitude by about 2.5 mV/°C in the range 30° – 70° C. The difference between these two experiments was in equilibration time. Morgan's experiment lasted for 4 hours, while Ishido and Mizutani's experiment lasted for many tens of hours.

Wurmstich and Morgan (1994) investigated whether streaming potential measurements in boreholes and at the surface can be used to monitor subsurface flow and detect subsurface flow patterns in oil reservoirs. They modeled streaming potential responses caused by oil well pumping in monitoring wells and at the earth's surface. The oil reservoir was at 325 – 500 m depth, a total production rate of 500 bbl/day for all phases (gas/water or oil/water), a porosity of 0.2 in the reservoir, brine conductivities in the range of 0.3 S/m to 1.0 S/m, and water saturations in the range of 0.7 to 1.0. Maximum values of the computed streaming potential response were less than 0.6 mV at the surface and less than 9 mV in the monitoring wells (about 100 m from the production well). In observation wells father than 1000 m from the production well signal will decrease to a few μV.

Mikhailov et al. (2000) reported for granite containing water with the salinity of 0.004 mol/liter of NaCl and the conductivity of 0.022 S/m the value of the zeta potential of –60 mV, measured in laboratory. Values of the zeta potential of diorite are not available in the literature, but they hypothesize that is lower than granite. It is important to remember, however, that the zeta potential depends on the type of pore fluid.

A study done by Sprunt et al. (1994) shows that the solid-brine streaming potential coupling coefficient is independent of the permeability of the rock. Air bubbles were found to increase streaming potential coupling coefficient by more than two orders of magnitude over the value for single-phase brine flow. Two-phase oil-brine flow may also produce larger electrokinetic potential than single-phase flow.

Middleton (1997) studied dependence of the streaming potential on the applied pressure. The studies were done for sandstone and fractured granite. The study showed a simple relationship $\Delta V = A\ \Delta P$ for ΔP less than 0.075 MPa, where ΔV is the streaming potential, A is the coupling coefficient, and ΔP in the applied pressure. Some rocks exhibited a departure from this linear behavior for applied pressures in the range 0.008 MPa to 0.03 MPa. This non-linear behavior is described as $\Delta V = A\ [1 - B\ \Delta P^{m-1}]\ \Delta P$, where B and m

are constants. The constant m is typically in the range 2 to 3. This non-linear behavior is proposed to be caused by flow separation due to pore roughness.

Algorithm for numerical simulation

For numerical simulation program developed by Sill (1983) was used. This algorithm uses an approximate algorithm to solve the primary potential problem (fluid flow, heat flow, etc.) in the first step. The second step consists of using the primary potential solution along with a model for cross-coupling coefficients to calculate the sources for the electric problem (div J = 0). The final step uses the current sources along with an electrical model to determine the resultant electrical potentials. The solution of the coupled problem requires three models for the physical properties: the primary flow resistivity, the voltage cross-coupling coefficients, and the electrical resistivity.

The Sill algorithm allows for the forward model calculation of primary potential (pressure or temperature) and secondary potential (voltage) for discrete sources of heat or pressure in 2-D model. The program allows for 2-D distribution of physical properties and 3-D source function. The calculations are done in three steps. First, the pressure or temperature distribution is determined from the source parameters and the permeability or thermal conductivity distribution. Then, the locations and strengths of the induced electrical sources are determined. The last step is to compute SP voltages from the induced electrical sources and the two-dimensional resistivity distribution. The program is using a transmission surface approach. The equations are transformed to a Fourier domain and solved there.

Induced current sources are inversely proportional to the resistivity. Since the voltage is proportional to the current-resistivity product, the resultant model voltages depend only on resistivity ratios. In other words, the same potentials will result for all models that differ only by a multiplicative factor in all the models resistivities. The SP anomalies are largest near the primary flow sources and in regions where the cross-coupling coefficients change (geological boundaries).

Survey Costs

While survey costs are always variable depending on surface conditions and access, we estimate that SP data acquisition cost will run between 25 and 50 % of the cost of traditional magnetotelluric data acquisition. This translates to between $500 and $1000 per line kilometer. These costs are based on measurements spacing of 100 m. For 3D surveys the line spacing should be the same as station spacing along the line resulting in a cost of $5000 to $10,000 per square kilometer.

References

Anderson, L.A., and Johnson, G.R., 1976, Application of the self-potential method to geothermal exploration in Long Valley, California: J. Geophys. Res., 81, p. 1527-1532.

Bogoslovsky, V.A., and Ogilvy, A.A., 1973, Deformations of natural electric fields near drainage structures: Geophys. Prosp., **21**, p. 716-723.

Combs, J. and Wilt, M., 1976, Telluric mapping, telluric profiling, and self-potential surveys of the Dunes geothermal anomaly, Imperial Valley, California: Proc. 2nd U.N. Sympos. Of the Devel. And Use of Geothermal Resources, San Francisco, CA, U.S. Gov. Printing Office, Washington, D.C., v. 2, p. 917-928.

Corwin, R.F., 1976, Self-potential exploration for geothermal reservoirs: Proc. 2nd U.N. Sympos. Of the Devel. And Use of Geothermal Resources, San Francisco, CA, U.S. Gov. Printing Office, Washington, D.C., v. 2, p. 937-945.

Corwin, R.F., and Hoower, D.B., 1979, The self-potential method in geothermal exploration: Geophysics, **44**, p. 226-245.

Corwin, R.F., and Morrison, H.F., 1977, Self-potential variations preceding earthquakes in central California: Geophys. Rev. Lett., **4**, p. 171-174.

Corwin, R.F., and Morrison, H.F., Diaz, S.C., and Rodriguez, B., 1980, Self-potential studies at the Cerro Prieto geothermal field: Geothermics, **9**, p. 39-47.

Fitterman, D.V., 1978, Electrokinetic and magnetic anomalies associated with dilatant regions in a layered earth: J. Geophys. Res., **83**, B12, p. 5923-5928.

Fitterman, D.V., 1983, Self-potential surveys near several Denver Water Department dams: U.S. Geol. Surv. Open file rept. 82-470.

Fitterman, D.V., and Corwin, R.F., 1982, Inversion of self-potential data from the Cerro Prieto geothermal field, Mexico: Geophysics, **47**, p. 938-945.

Hoversten, G. M., Gritto, R., Washbourne, J. and Daley, T., 2003, Pressure and fluid saturation prediction in a multicomponent reservoir using combined seismic and electromagnetic imaging: Geophysics, **68**, p. 1580-1591.

Marshall, D.J., and Madden, T.R., 1959, Induced polarization, A study of its causes: Geophysics, **24**, p. 790-816.

Middleton, M.F., 1997, Measurements of streaming potential versus applied pressure for porous rocks: Phys. Chem. Earth, **22**, p. 81-86.

Mikhailov, O.V., Queen, J., and Toksoz, M.N., 2000, Using borehole electroseismic measurements to detect and characterize fractured (permeable) zones: Geophysics, **65**, p. 1098-1112.

Morgan, F.D., Williams, E.R., and Madden, T.R., 1989, Streaming potential properties of Westerly granite with applications: Journal of Geophysical Research, **94**, p. 12,449-12,461.

Ogilvy,A.A., Ayed, M.A., and Bogoslovsky, V.A., 1969, Geophysical studies of water leakages from reservoir: Geophys. Prosp., **17**, p. 36-62.

Pride, S.R., and Morgan, F.D., 1991, Electrokinetic dissipation induced by seismic waves: Geophysics, **56**, p. 914-925.

Sill, W.B., 1983, Self-potential modeling form primary flows: Geophysics, **48**, p. 76-86.

Sprunt, E.S., Mercer, T.B., and Djabbarah, N.F., 1994, Streaming potential from multiphase flow: Geophysics, **59**, p. 707-711.

Wurmstich, B., and Morgan, F.D., 1994, Modeling of streaming potential responses caused by oil well pumping: Geophysics, 59, p.46-56.

Wurmstich, B., 1995, 3D self-consistent modeling of streaming potential responses: Theory and feasibility of applications in earth sciences: Ph.D. dissertation, Texas A&M University, Austin, Texas, 314 p.

Zablocki, C.J., 1976, Mapping thermal anomalies on an active volcano by the self-potential method, Kilauea, Hawaii: Proc. 2nd U.N. Sympos. Of the Devel. And Use of Geothermal Resources, San Francisco, CA, U.S. Gov. Printing Office, Washington, D.C., v. 2, p. 1299-1309.

Zohdy, A.A.R., Anderson, L.A., and Muffler, L.J.P., 1973, Resistivity, self-potential and induced polarization surveys of a vapor-dominated geothermal system: Geophysics, **38**, p. 1130-1144.

Zlotnicki, J., Boudon, G., Viode, J.P., Delarue, J.F., Mille, A., and Bruere, F., 1998, Hydrothermal circulation beneath Mount Pelee inferred by self potential surveying. Structural and tectonic implications: Journal of Volcanology and Geothermal Research, **84**, p. 73-91.